In-line high-rate evaporation of aluminum for the metallization of silicon solar cells

Von der Fakultät für Mathematik und Physik
der Gottfried Wilhelm Leibniz Universität Hannover
zur Erlangung des Grades

Doktor der Naturwissenschaften
Dr. rer. nat.

genehmigte Dissertation

von

Dipl.-Phys. oec. Christoph Paul Mader

geboren am 03.11.1980 in Preetz

2012

Referent:	Prof. Dr.-Ing. Rolf Brendel
Korreferent:	Prof. Dr.-Ing. Lutz Rissing
Tag der Promotion:	11.07.2012

Kurzzusammenfassung

Das Thema dieser Arbeit ist die Evaluierung und Optimierung des Durchlaufhochratenaufdampfens von Aluminium zur Kontaktierung von Silizium Solarzellen. Im Rahmen der Arbeit werden Wafertemperaturen während des Beschichtungsprozesses bestimmt sowie die Waferverbiegung nach dem Aufdampfen und die elektrischen Eigenschaften der abgeschiedenen Aluminiumschichten untersucht. Desweiteren wird erstmalig gezeigt, dass durch einen einfachen Aufdampfschritt ohne weitere Temperaturbehandlungen aluminiumdotiertes Silizium hergestellt werden kann.

Die Temperaturentwicklung von Silizium Wafern während des Durchlaufhochratenaufdampfens von Aluminium wird untersucht. Es wird experimentell gezeigt, dass die Wafertemperaturen von der Waferdicke W, der Aluminiumschichtdicke d und der Emissivität ε des Wafers abhängen. Zweidimensionale Finite-Elemente Simulationen geben die gemesssenen Maximaltemperaturen mit einer Genauigkeit von 97% wieder.

Im Rahmen dieser Arbeit wird ebenfalls die Waferverbiegung nach dem Durchlaufhochratenaufdampfen untersucht. Die gemessenen Verbiegungen werden durch die elastische Verbiegungstheorie überschätzt, können jedoch unter Annahme einer zunächst elastischen Verbiegung und einer nach dem ersten Abkühlen einsetzenden plastischen Verformung beschrieben werden.

Desweiteren werden die elektrischen Eigenschaften der aufgedampften Aluminiumschichten und hierbei insbesondere die Sperrsättigungsstromdichten und Kontaktwiderstände untersucht. Es können Parametrisierungen der gemessenen Sperrsättigungsströme von Kontakten zu p-Typ Wafern sowie zu bordiffundierten Schichten erstellt werden. Ferner wird ebenfalls eine Parametrisierung der gemessenen Kontaktwiderstände zu p-Typ Silizium mit verschiedenen Oberflächendotierungen sowie eine Berechnung der Aktivierungsenergie des Kontaktbildungsprozesses präsentiert.

Die gemessenen elektrischen Eigenschaften werden in eindimensionalen Simulationen zur Abschätzung von Wirkungsgraden von Solarzellen verwendet. Anhand der Simulationen kann gezeigt werden, dass das Ersetzen eines siebgedruckten Aluminiumrückkontaktes durch einen aufgedampften Aluminiumrückkontakt eine Steigerung des Zellwirkungsgrades um bis zu 1.6% ermöglicht.

Erstmalig wird in dieser Arbeit gezeigt, dass durch einen einfachen Aufdampfschritt ohne weitere Temperaturbehandlungen aluminiumdotierte p^+ Bereiche hergestellt werden können und dass die Sperrsättigungsstromdichten von ganzflächigen und von lokalen p^+ Regionen im Bereich von konventionell eingesetzten siebgedruckten p^+ Bereichen liegen.

Diese Arbeit zeigt die hohe Qualität von mittels Hochratenaufdampfens im Durchlaufverfahren hergestellten Aluminiumkontakten zu Silizium Solarzellen und dass das Hochratenaufdampfen eine gute Alternative zum konventionellen Siebdruckprozess ist.

Abstract

This work focuses on the in-line high-rate evaporation of aluminum for contacting rear sides of silicon solar cells. The substrate temperature during the deposition process, the wafer bow after deposition, and the electrical properties of evaporated contacts are investigated. Furthermore, this work demonstrates for the first time the formation of aluminum-doped silicon regions by the in-line high-rate evaporation of aluminum without any further temperature treatment.

The temperature of silicon wafers during in-line high-rate evaporation of aluminum is investigated in this work. The temperatures are found to depend on the wafer thickness W, the aluminum layer thickness d, and on the wafer emissivity ε. Two-dimensional finite-element simulations reproduce the measured peak temperatures with an accuracy of 97%.

This work also investigates the wafer bow after in-line high-rate evaporation and shows that the elastic theory overestimates the wafer bow of planar Si wafers. The lower bow is explained with plastic deformation in the Al layer. Due to the plastic deformation only the first 79 K in temperature decrease result in a bow formation.

Furthermore the electrical properties of evaporated point contacts are examined in this work. Parameterizations for the measured saturation currents of contacted p-type Si wafers and of contacted boron-diffused p^+-type layers are presented. The contact resistivity of the deposited Al layers to silicon for various deposition processes and silicon surface concentrations are presented and the activation energy of the contact formation is determined.

The measured saturation current densities and contact resistivities of the evaporated contacts are used in one-dimensional numerical simulations and the impact on energy conversion efficiency of replacing a screen-printed rear side by an evaporated rear side is presented.

For the first time the formation of aluminum-doped p^+-type (Al-p^+) silicon regions by the in-line high-rate evaporation of aluminum without any further temperature treatment is presented. Contact saturation current densities of full-area and of local Al-p^+ regions are shown to be in the same range as published data of unpassivated screen-printed Al-p^+ regions.

The results of this work prove the high quality of rear contacts to silicon solar cells that are formed by in-line high-rate evaporation of aluminum and that evaporation is a competitive alternative to the screen-printing technology.

Schlagworte: Durchlauf-Hochraten-Aufdampfen, Silizium-Solarzelle, Temperatur
Keywords: in-line high-rate evaporation, silicon solar cell, temperature

Contents

Introduction

In contrast to fossil energy resources renewable energies like wind, water, and solar energy are not limited and they might offer an alternative to the present energy supply. A main issue is driving down the costs of the renewable energies. Over the last 20 years the electricity price contribution of a photovoltaic module could significantly be reduced from about 6 Euro/kWh in 1976 to approximately 0.15 Euro/kWh in 2010 [1]. However, a further reduction of the costs per kWh is necessary. This can either be done by reducing the production costs of solar cells and/or by increasing the energy conversion efficiency. Alternative production processes might thus be of interest. Screen-printing of aluminum pastes is the state-of-the-art process in industrial metallization of silicon solar cells. This process has three steps: (i) A viscous metal paste is printed onto the silicon surface through a screen by applying a force. (ii) The paste is dried for about 5 minutes at a temperature of $\sim$ 500 K. (iii) The metal paste is fired in a conveyor-belt furnace at peak temperatures of $\sim$ 1100 K [2]. The firing provides an ohmic contact on the entire rear side and also forms an aluminum-doped p^+-type region, which reduces the rear surface recombination [3]. However, the electrical and optical properties of such aluminum-doped p^+-type regions are only moderate and the full-area metal-semiconductor contact often limits the solar cell open-circuit voltage and therefore the energy conversion efficiencies. Additionally, the screen-printing process leads to mechanical stress of the wafer and wafer bowing during the firing process is a severe problem for the mechanical yield in production [4]. In contrast, evaporation of aluminum for contacting silicon solar cells is known as a high-efficiency laboratory technique [5–7] used for the metallization of record solar cells [8–10]. The evaporation process consists mainly of three sequential steps: (i) A solid source of film material is provided, (ii) the material evaporates in vacuum and is transported to the substrate, and (iii) the deposition takes place. Recently, the in-line high-rate evaporation of aluminum to the rear side of 'passivated emitter and rear cells' (PERC) has been introduced as a potentially industrially feasible metallization scheme [11,12]. Besides technological advantages over screen-printed contacts the evaporation of aluminum might also offer economical benefits, since the costs of the consumables can be reduced when using the evaporation technique. Nevertheless, so far screen-printing is still the standard technique used in the industry for the rear contact formation to silicon solar cells. This thesis investigates the technological potential of the in-line high-rate evaporation of aluminum - as a potentially industrially feasible metallization scheme - for rear contacts to silicon solar cells.

Chapter 1 gives a short review of the physics of metal-semiconductor contacts. Screen-printing, the state-of-the art metallization technique, is shortly presented and the evaporation process as well as an in-line high-rate evaporation system are introduced.

Chapter 2 deals with the temperature of silicon wafers and of silicon solar cells during the in-line high-rate deposition of aluminum. Measured temperatures are presented and two-dimensional finite-element simulations are carried out. Using the simulation tool the deposition process is optimized regarding temperature limits.

Chapter 3 examines the wafer bow of silicon wafers after the in-line high-rate deposition of aluminum. The wafer bow is investigated regarding elastic bending and plastic deformation and an analytical formula for describing the bow is deduced.

Chapter 4 investigates point contacts to boron-doped p-type silicon wafers and to boron-diffused p^+-layers. The point contacts are formed by laser contact openings and by evaporation of aluminum and are investigated regarding their contact resistivity and saturation current densities. Parameterizations for both electrical properties are presented.

Chapter 5 describes the formation of aluminum-doped p^+-type (Al-p^+) silicon regions by the evaporation of aluminum. The aluminum-doped regions are analyzed by scanning electron microscope investigations, by electrochemical capacitance voltage profiling, and by minority charge carrier lifetime measurements. Saturation current densities of full-area aluminum-doped regions and of local contacts are presented.

Chapter 6 estimates the impact of replacing screen-printed rear contacts by evaporated contacts. As the baseline case a PERC solar cell with screen-printed metallization is considered. The rear side is replaced by (i) evaporated base contacts and (ii) by a boron-diffused back surface field layer and evaporated contacts.

Chapter 7 summarizes this work.

Annex A gives an analytical verification of the two-dimensional temperature simulations from Chapter 2.

Annex B investigates the electrical properties contact resistivity and saturation current density of evaporated point contacts to n^+-type silicon.

1. Review of rear contacts to silicon solar cells

In this thesis, the contact formation to silicon solar cells by means of in-line high-rate evaporation is investigated. In order to motivate the topic of this work, the current Chapter gives a short overview of the metal-semiconductor contact theory. Also, the screen-printing process, the standard industrial technology for the formation of aluminum contacts to silicon solar cells, is introduced. The principle of evaporation of aluminum is discussed and the in-line high-rate evaporation of aluminum using the *ATON 500* deposition system is presented. The potential advantages of evaporated contacts over screen-printed contacts are briefly discussed.

1.1. Metal-semiconductor contact

The metal-semiconductor contact was first examined by Braun in 1874 [13], who found the rectifying characteristics of metal contacts to semiconductors. The theory for understanding these devices was independently given by Schottky and Mott in 1938 [14, 15]. They explained the characteristics of the metal-semiconductor contact by the existence of a potential barrier. Metal-semiconductor contacts are thus often referred to as Schottky-Mott contacts.

In the following the theory of the metal-semiconductor contact will briefly be reviewed. The focus is hereby on aluminum contacts to p-type silicon. This Section is based on a review given by Rhoderick and Williams [16]. When a metal and a semiconductor are connected, the silicon near the junction depletes of majority carriers since many unoccupied states are offered in the metal. In thermal equilibrium the Fermi level along both materials lines up and the valence band near the junction forms a barrier for holes flowing from the semiconductor to the metal. Figure 1.1 shows a schematic of the aluminum contact to p-type silicon according to the Schottky-Mott model. The graph shows (a) separated metal and semiconductor and (b) the ideal metal-semiconductor contact. The barrier height when contacting p-type silicon can be written as

$$\Phi_{\mathrm{B}} = E_{\mathrm{G}} - (\Phi_{\mathrm{M}} - \chi_{\mathrm{S}}), \tag{1.1}$$

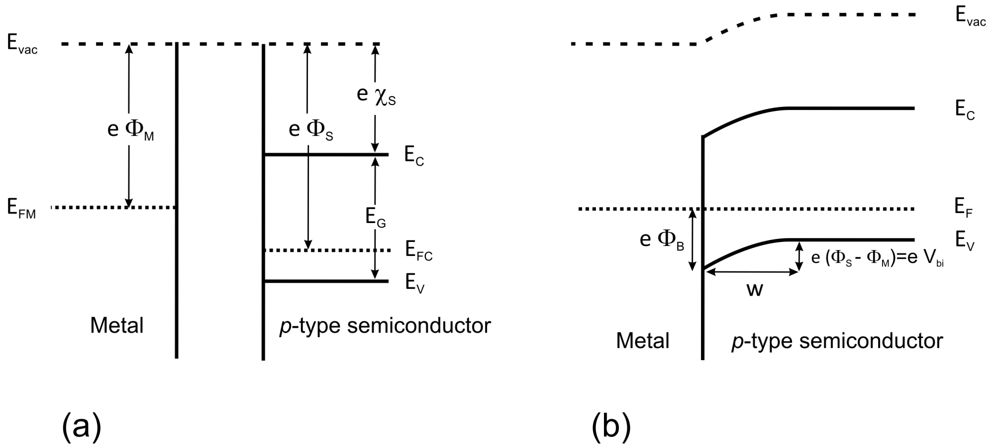

Figure 1.1.: *A rectifying metal contact to a p-type semiconductor according to the Schottky model. (a) Separated metal and semiconductor and (b) the ideal metal-semiconductor contact according to Schottky-Mott.*

where E_{G} is the band gap of the semiconductor, Φ_{M} is the metal work function, i. e. the potential difference between the Fermi level of the metal and the vacuum level, and χ_{S} is the semiconductor electron affinity, i. e. the potential difference between the bottom of the conduction band and the vacuum level. Note that the barrier heigth Φ_{B} according to Eq. (1.1) does not depend on the doping density N_{A} and that following the Schottky-Mott theory the barrier height to silicon is expected only to depend on the metal work function Φ_{M}.

Experimentally it was found that the barrier height is a less sensitive function of Φ_{M} than Eq. (1.1) would suggest [16]. Bardeen suggested this difference between the Schottky-Mott theory and the experimentally found data to be caused by interface states [17]. He supposed that the metal and semiconductor remain separated by a thin insulating layer and that there is a continuous distribution of surface states present at the interface between the semiconductor and the insulator. If the surface states contain a net charge the width

$$w = \left(\frac{2\varepsilon_{\mathrm{s}}\varepsilon_0 V_{\mathrm{bi}}}{qN_{\mathrm{A}}} \right)^{1/2} \tag{1.2}$$

of the depletion region, depending on the silicon doping density N_{A}, the build-in voltage V_{bi}, the relative permittivity ε_{s} of silicon, and the vacuum permittivity $\varepsilon_0 = 8.85\times10^{-12}$ F/m, is reduced and the band bending will thus also decrease. The barrier height is reduced and is said to be pinned by these states (Fermi-level-pinning). An alternative explanation for the barrier lowering is the formation of an electric field in the semiconductor at the contact interface. A so called image-force is bending the valence band upwards near the interface and thus the barrier height is reduced close to the interface [18,19]. The barrier lowering due to the image force

$$\Delta\Phi = \left(\frac{q^3 N_\mathrm{A}(V_\mathrm{bi} - kT/q)}{8\pi^2\varepsilon_\mathrm{s}^3\varepsilon_0^3}\right)^{1/4} \tag{1.3}$$

follows by simple electro-static considerations [16] and depends on the elementary charge $q = 1.6\times10^{-19}$ C, the silicon doping density N_A, the build-in voltage V_bi, the Boltzmann constant $k = 8.6\times10^{-5}$ eV/K, the temperature T, the relative permittivity ε_S of silicon, and the vacuum permittivity $\varepsilon_0 = 8.85\times10^{-12}$ F/m. The image-force lowering influences the current transport.

In the following the current transport in a metal-semiconductor contact is briefly discussed. The principal underlying transport is analogous to the thermionic emission of holes into a vacuum. Thus, the current-voltage relation in a Schottky-Mott contact is

$$j = A^* T^2 \exp\left(-\frac{q\ (\Phi_\mathrm{B} - \Delta\Phi)}{kT}\right)\left(e^{\frac{qV}{kT}} - 1\right), \tag{1.4}$$

where $A^* = R\ m^*/m_0$ is the effective Richardson constant, depending on the Richardson constant $R = 120$ A/(cm^2 K^2), the semiconductor effective hole mass m^* and the free hole mass m_0. V is the applied voltage and positive in forward bias. The effective mass depends on the type of doping and on the crystal orientation. The effective Richardson constant A^* in the case of p-type silicon is $A^* = 32$ A/(cm^2 K^2) [20]. The contact resistivity

$$\rho_\mathrm{c} = \left(\frac{dj}{dV}\right)^{-1}_{V\to0} \tag{1.5}$$

for thermionic emission is then given by

$$\rho_\mathrm{c}(TE) = \frac{k}{qA^*T}\exp\left(\frac{q\,(\Phi_\mathrm{B} - \Delta\Phi)}{kT}\right). \tag{1.6}$$

The current-voltage relation predicted by thermionic emission has an ideal rectifying characteristic. However, under certain circumstances it may be possible for holes with energies below the barrier height to penetrate the barrier by quantum-mechanical tunneling [21,22] and thus to form ohmic contacts. A model for this tunneling was given by Padovani et al. [23] and by Crowell et al. [24]. They use a characteristic energy

$$E_{00} = \frac{q\hbar}{2}\left(\frac{N_\mathrm{A}}{m_\mathrm{t}^*\varepsilon_\mathrm{S}\varepsilon_0}\right)^{1/2}, \tag{1.7}$$

where $\hbar = 6.58\times10^{-16}$ eV s is the reduced Planck constant and ${m^*}_\mathrm{t}$ the effective tunnel mass, to describe the theory of the metal-semiconductor contact. In the case of $kT/E_{00} \gg 1$, the thermionic emission dominates and the contact resistivity is given by Eq. (1.6). With increasing doping densities holes that are thermally excited to higher energies are able to tunnel through the thin barrier. This so called thermionic field emission takes place in the case of $kT/E_{00} \approx 1$. The contact resistivity in this doping region can be calculated using the WKB (Wentzel-Kramers-Brillouin) approximation [22]. The contact resistivity ρ_c is then given by

$$\rho_{\mathrm{c}}(TFE) = C_1 \frac{k}{qA^*T} \exp\left(\frac{q\left(\mathit{\Phi}_{\mathrm{B}} - \Delta\mathit{\Phi}\right)}{E_{00}\coth(E_{00}/kT)}\right), \tag{1.8}$$

with

$$C_1 = kT\cosh\left(\frac{E_{00}}{kT}\right)\left(\frac{\coth\left(E_{00}/kT\right)}{\pi E_{00}\left(\mathit{\Phi}_{\mathrm{B}} + E_{\mathrm{F}}\right)}\right)^{1/2} \exp\left(\frac{E_{\mathrm{F}}}{E_{00}\coth\left(E_{00}/kT\right)} - \frac{E_{\mathrm{F}}}{kT}\right). \tag{1.9}$$

E_{F} is the Fermi energy level with respect to the valence band. For higher doping densities, when $kT/E_{00} \ll 1$, field emission takes place and the contact resistivity follows by

$$\rho_{\mathrm{c}}(FE) = C_2 \frac{k}{qA^*T} \exp\left(\frac{q\left(\mathit{\Phi}_{\mathrm{B}} - \Delta\mathit{\Phi}\right)}{E_{00}}\right), \tag{1.10}$$

where C_2 is given by

$$C_2 = \left(\frac{\pi}{\sin\left(\frac{\pi kT}{2\,E_{00}}\ln\left(\frac{4\,\mathit{\Phi}_{\mathrm{B}}}{E_{\mathrm{F}}}\right)\right)} - \frac{2\,E_{00}}{kT\ln\left(\frac{4\,\mathit{\Phi}_{\mathrm{B}}}{E_{\mathrm{F}}}\right)}\right) \exp\left(-\frac{E_{\mathrm{F}}\ln\left(\frac{4\,\mathit{\Phi}_{\mathrm{B}}}{E_{\mathrm{F}}}\right)}{2\,E_{00}}\right). \tag{1.11}$$

According to this model the metal-semiconductor contact resistivity decreases with increasing doping density. This is consistent with experimental findings, where a decrease of the contact resistivity with increasing surface doping density was observed [25].

1.2. The screen-printing process

Screen-printing is the standard technique used for the formation of aluminum rear contacts to silicon solar cells. The screen-printing process has been described in many publications and more detailed information can be found in Refs. [26–29]. This Section is based on a review given in Ref. [29]. The process mainly consists of three steps: (i) A viscous metal paste is printed onto the silicon surface through a screen by applying a force. (ii) The paste is dried for about 5 minutes at a temperature of ∼ 500 K. (iii) The metal paste is fired in a conveyor-belt furnace at peak temperatures of ∼ 1100 K.

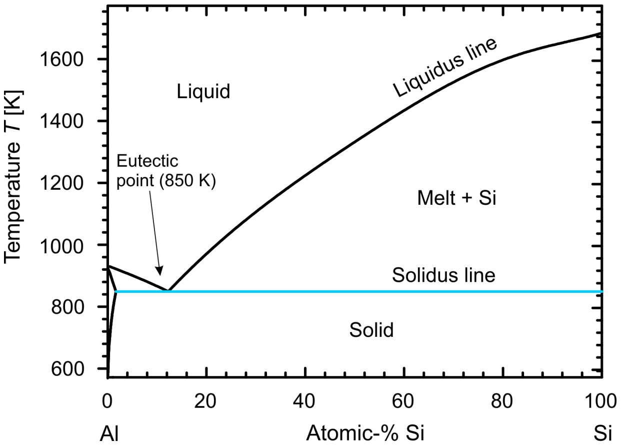

Figure 1.2.: *Binary phase diagram of aluminum and silicon showing the eutectic point at 850 K.*

The Al paste is an important component which has a crucial impact on the contact properties. Usually, a metallization paste for the rear side of a silicon solar cell consists of small-grained Al particles plus a small amount of a glass frit, which are both suspended in an organic solvent. The organic solvent is used to keep the Al particles and the glass frit in the paste in suspension and it is mainly responsible for the rheology of the paste. About 70-80 wt% of the complete paste consist of the metal component of small-grained Al particles. The glass frit enhances the sintering and secures a good mechanical contact of the metal to the silicon during firing. The firing also forms a highly aluminum-doped p^+ region. The morphological and electrical properties of a screen-printed Al-p^+ region are mainly influenced by the firing process.

The firing process can be divided into three sub-processes: (i) the burnout of the organic solvents and softening of the glass frit, (ii) the alloying of the Al and Si at the interface, and (iii) solidification of the Al-Si melt during cooling. Figure 1.2 shows a binary phase diagram of aluminum and silicon [30]. According to the phase diagram the melting point of Si decreases -starting at 1683 K for 100 at% Si- along the liquidus line with increasing Al concentration. At a Si concentration of about 12%, and thus of 88% Al, the melt solidifies at 850 K which is well below the solidification point of any other Al-Si composition. This so-called *eutectic point* represents the lowest solidification temperature where the liquid and the two solid phases coexist and are in chemical equilibrium. During firing, at the peak temperature of ~1100 K, a closed film of an Al-Si liquid forms at the Si surface. During cooling, the Al-Si liquid starts to undercool, thus the Si concentration in the melt is decreasing in accordance with the liquidus line in Fig. 1.2. During this process the excess amount of Si is rejected from the melt and Si grows epitaxially at the solid-Si/liquid-Al-Si interface. The epitaxially grown Si layer is now doped with Al in accordance with the solid solubility of Al in Si at a given temperature.

The Al-p^+ region formed during the firing step serves as the so-called back surface field (BSF) layer, which reduces the recombination of charge carriers at the rear side of the cell. This can be explained by the potential barrier between the p-type base and the p^+-type Al-BSF of sufficient thickness, which hinders the minority charge carriers to reach the highly recombination-active metallized Si surface and to recombine there [3]. Thus, the Al-BSF lowers the recombination underneath the metal contacts drastically, which increases the solar cell efficiency.

However, the electrical and optical properties of such an Al-BSF are only moderate and the full-area metal-semiconductor contact often limits the solar cell open-circuit voltage and therefore the energy conversion efficiency. Industrial-like silicon solar cells with a full-area screen-printed Al-p^+ back surface field achieve efficiencies of up to 18.6% on p-type, B-doped Czochralski-grown silicon wafers with an area of 156 cm^2 [31]. In order to reduce the rear recombination, the rear side can be passivated and contacted by local aluminum contacts.

In 1989 the 'passivated emitter and rear cell' (PERC) was introduced by Blakers et al. [5]. This cell features a passivated rear side and only local contacts. Industrial-type PERC solar cells with a screen-printed aluminum rear-contact have achieved energy conversion efficiencies up to 20.2% on p-type, B-doped Czochralski-grown silicon wafers with an area of 243 cm^2 [32, 33]. Nevertheless, the high contact resistivity of ~ 15 mΩ cm^2 of screen-printed aluminum contacts to silicon is still limiting the fill factor and thus the efficiency of industrial-type PERC solar cells [34]. Additionally, the screen-printing process leads to mechanical stress of the wafer and wafer bowing during the firing process is a severe problem for the mechanical yield in production [4]. Regarding the trend to thinner Si wafers this is an issue, since mechanical stresses increase with decreasing wafer thicknesses [35]. Also, the production of the Al pastes is technologically demanding and the pastes are thus expensive and they contain organic solvents, which is critical regarding the environment.

1.3. The evaporation process

The evaporation of aluminum is often used in laboratories for the contact formation to the rear side of silicon solar cells. In contrast to screen-printing, the evaporation of aluminum does not typically lead to the formation of an aluminum-doped p^+-type back surface field. Evaporated Al contacts thus feature high recombination at the silicon-aluminum interface. In order to reduce this recombination, evaporated rear contacts are often applied to solar cells that feature a passivated rear side and only local contacts [5]. For example, the rear sides of the solar cells in Ref. [5] were metallized by evaporated aluminum contacts and record cell efficiencies of 22.8% were reported (p-type, B-doped float-zone silicon, 4 cm^2). However, the high recombination at the silicon-aluminum interface was still limiting the energy conversion efficiency of PERC solar cells. By diffusing boron on the rear side of the solar cells, the performance could significantly be improved.

In 1991, first results on 'passivated emitter rear totally diffused' (PERT) solar cells were reported [36]. These cells achieved energy conversion efficiencies of up to 24.5% (p-type, B-doped magnetically confined Czochralski-grown silicon, 4 cm^2). However, the diffusion on the entire rear surface is increasing the recombination in the passivated areas between the contacts. As a consequence, 'passivated emitter rear localy diffused' (PERL) solar cells were developed, where boron was only diffused into the contact areas at the rear of the cells. The reported efficiency of 25% is still the highest efficiency measured under the global AM1.5 spectrum (1000 W/m^2) at 298 K (p-type, B-doped float-zone silicon, 4 cm^2) [10,37]. These laboratory PERC, PERT, and PERL cells demonstrate the potential of evaporated aluminum rear contacts. In the following, the fundamentals of the evaporation process are discussed and a potentially industrially feasible in-line high-rate metallization system is introduced.

1.3.1. Fundamentals of evaporation

The evaporation of metals is a physical vapor deposition (PVD) process and is used to deposit thin layers on substrates. The process contains mainly three sequential steps: (i) A solid source of film material is provided, (ii) the material evaporates in vacuum and and is transported to the substrate, and (iii) the deposition takes place. The solid film material is hereby vaporized by heat or by an energetic beam of electrons, photons, or positive ions. In this work, the thermal evaporation of aluminum onto silicon is considered. In the following a brief overview of the evaporation process will be given.

In vacuum, vapor is produced from a heated metal. The temperature-dependent equilibrium vapor pressure

$$\frac{\mathrm{d}p_\mathrm{v}}{\mathrm{d}T} = \frac{\Delta H_\mathrm{v}}{T(V_\mathrm{v} - V_\mathrm{l})} \tag{1.12}$$

is given by the Clausius-Clapeyron equation, where T is the temperature, ΔH_v is the heat of evaporation, and V_v and V_l are the molar volume of the vapor and of the liquid phase, respectively. The molar volume of the liquid phase can be neglected compared to that of the vapor phase. In vacuum the metal vapor can be regarded as an ideal gas and Eq. (1.12) thus simplifies to

$$\frac{\mathrm{d}p_\mathrm{v}}{p_\mathrm{v}} = \frac{\Delta H_\mathrm{v}\mathrm{d}T}{RT^2}, \tag{1.13}$$

where $R = 8.31$ J/(mol K) is the gas constant. Eq. (1.13) integrates to

$$p_\mathrm{v} = A\, e^{-\frac{\Delta H_\mathrm{v}}{RT}}, \tag{1.14}$$

where A is a constant of integration. In practice, the evaporation rate, which describes the per time and area evaporated amount of material, is more of interest than the equilibrium vapor pressure. The evaporation rate

$$G = 0.044\, p_\mathrm{v} \sqrt{\frac{M}{T}} \tag{1.15}$$

depends on the equilibrium vapor pressure p_v, the molar mass M, and the temperature T of the evaporation source [38]. Low evaporation rates cause reactions of the evaporated metal with residual gas molecules, which may lead to oxidized films on the substrate. High evaporation rates lead to an increased vapor pressure and thus to increased collisions of the vapor particles, resulting in a lowering of the rate. The evaporated aluminum particles have in average an energy E_v of

$$E_v = \frac{m}{2} v^2 = \frac{3}{2} kT, \tag{1.16}$$

where v is the velocity of the particels. The average energy is thus depending on the temperature of the evaporation source. A typical evaporation temperature is in the order of 1500 to 2000 K, the average energy of one aluminum atom is thus in the order of 0.2 to 0.26 eV. After the transport the evaporated material approaches the surface of the substrate and if enough of its perpendicular component of momentum is dissipated into the surface, the material will not be able to escape and will be attracted by the surface. The material might still be able to migrate along the surface, until absorbed. When deposited on the substrate, the atom releases its kinetic energy in the order of 0.2 to 0.26 eV. By the phase change from gaseous to solid, the enthalpy of sublimation $\Delta H_\mathrm{Al} = 11.25$ kJ/g is also released. This corresponds to an energy of 3.15 eV per Al atom. The evaporation process has been described in many publications and more detailed information can be found in Refs. [38–40].

1.3.2. In-line high-rate deposition system

The evaporation of aluminum in laboratories is usually done in batch evaporation systems. The systems consist of only one vacuum chamber, which has to be vented and evacuated for each deposition process. Thus, the batch systems are leading to high process times, which are probably not acceptable in solar cell productions. An in-line system that consists of various chambers is more suitable as an industrial application of the evaporation, since the process chamber does not have to be vented and evacuated for each deposition process and a higher throughput can thus be achieved.

ATON 500

Figure 1.3.: *In-line high-rate evaporation system ATON 500. The image shows the unloading area of the system and a carrier with 9 silicon solar cells after the rear side metallization.*

The aluminum depositions in this thesis are carried out in an in-line high-rate metallization system (*ATON 500* from *Applied Materials*). In winter 2008 / 2009 this system was installed at the Institute for Solar Energy Research Hamelin (ISFH). The author participated in the installation of the *ATON 500*. This included contract negotiations, definition of the technical requirements for the system, preparation of the technical infrastructure at ISFH, the mechanical installation itself, ordering of spare parts, and the process definition and process optimization. Figure 1.3 shows an image of the *ATON 500* and of a carbon carrier with nine silicon solar cells. The carrier moves with tray speed v_{tray} in continuous substrate flow through the deposition system. Figure 1.4 shows a schematic of the in-line high-rate deposition system. The system consists of 7 modules that are separated by valves. Each module features a pump unit in order to evacuate the corresponding module. The carrier enters the system in the loading area and moves into module 1. Module 1 is then evacuated within $\sim$ 25 seconds to a pressure of $\sim 7\times10^{-2}$ mbar. Subsequently the carrier moves to module 2, which is then evacuated within $\sim$ 20 seconds to a pressure of $\sim 1\times10^{-3}$ mbar. The waiting times in the modules 1 and 2 can be adapted if lower pressures are required. The shortest mechanical cycle time in order to avoid a 'carrier-jam' is 45 seconds. This results in a maximum throughput of 80 carriers and thus of 720 solar cells with edge length 156 mm per hour. The carrier moves into module 3 when the required pressure is reached. The Al deposition takes place in module 4. The process pressure depends on the Al deposition rate and is typically in the order of $(1\text{-}5)\times10^{-4}$ mbar. Aluminum vapor is generated in vacuum by continuously feeding Al wires to electrically-heated boron ni-

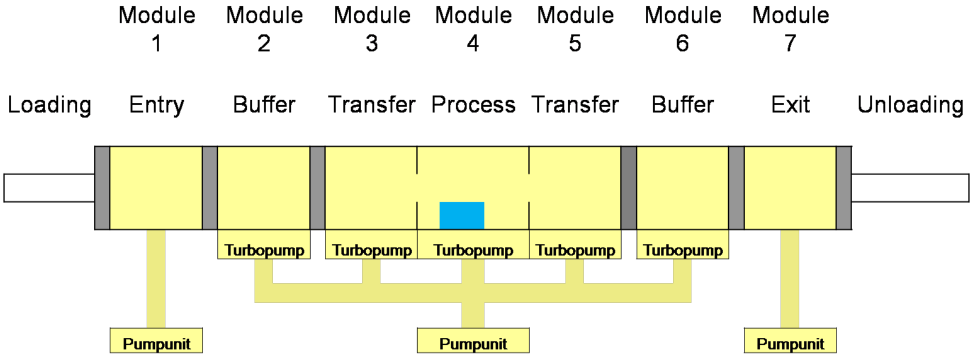

Figure 1.4.: *Schematic drawing of the ATON 500 in-line high-rate evaporation system. The carriers move in continuous substrate flow through the system from the loading to the unloading zone and pass the evaporator in module 4. Figure is taken from Ref. [41].*

tride boats. The evaporated aluminum deposits on the solar cells that move on the carrier through the deposition chamber. The wire velocity as well as the heating power can be adjusted for each boat to control the homogeneity over the complete tray width of 500 mm as well as the overall deposition rate. Figure 1.5 shows a schematic sketch of the deposition process. After the deposition process the carrier moves to module 7, which is then vented. Afterwards, the carrier moves to the unloading area.

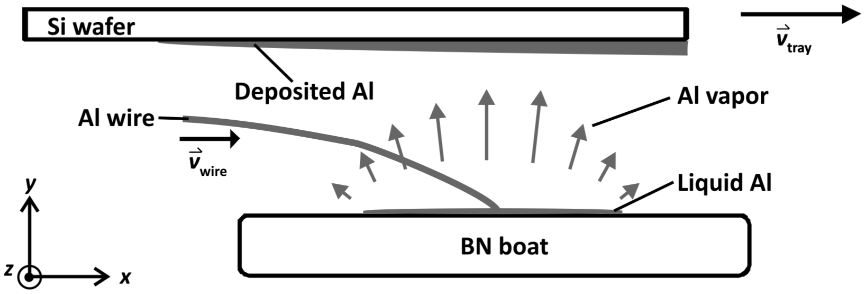

Figure 1.5.: *Schematic sketch of the Al deposition process. An aluminum wire is steered onto a heated boron nitride boat, resulting in a continuous generation of aluminum vapor. The evaporated aluminum deposits on the sample that moves on a carrier through the deposition chamber. 10 BN boats are positioned next to each other in z-dimension to have a homogeneous deposition on a width of 500 mm.*

Determination of dynamic deposition rate

The dynamic deposition rate $r_{\mathrm{dyn}} = d \times v_{\mathrm{tray}}$ is defined as the product of the Al layer thickness d deposited on a sample and the tray speed v_{tray}. We consider two dynamic deposition processes and employ two methods for determining the dynamic deposition rate r_{dyn}. In the first method we measure the Al layer thickness d after in-line deposition at various tray speeds v_{tray} and calculate the dynamic deposition rate as $r_{\mathrm{dyn}} = (4.9 \pm 0.2)$ µm×m/min for process 1 and $r_{\mathrm{dyn}} = (19.7 \pm 0.3)$ µm×m/min for process 2. For the measurement of the Al layer thickness d we fix a stripe of kapton tape onto a glass substrate. Then, we deposit the Al onto the glass and the kapton tape and remove the kapton tape after the deposition. This leads to a sharp edge and the Al layer thickness can be measured using a surface profiler (*Dektak 150* from *Veeco*).

In the second method we first perform a static deposition by evaporating the aluminum on the closed shutter, stopping the glass substrates over the boat and then opening the shutter. After 15 seconds the shutter is closed again and we measure the aluminum layer thicknesses d at various positions x on the glass substrates. We then determine the local static deposition rate $r_{\mathrm{s}}(x)$ along the direction of v_{tray}.

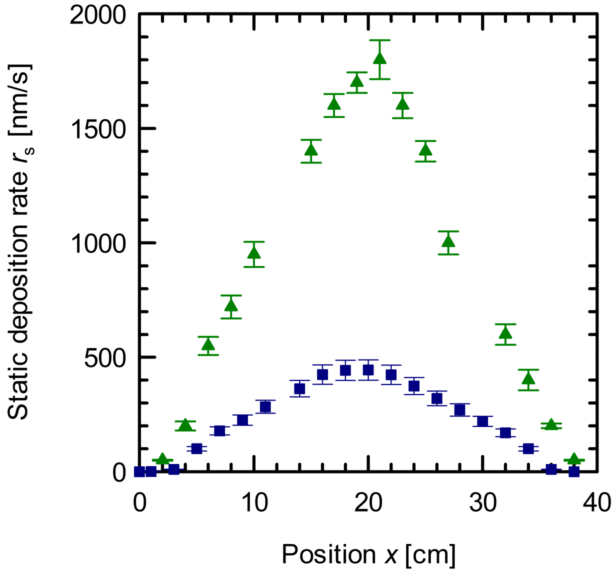

Figure 1.6.: *Local distribution of the static deposition rate $r_s(x)$ in the deposition chamber. The width l of the coating area for both processes in direction of sample flow is determined to be (35 ± 2) cm with a maximum static deposition rate $r_{s,max}$ in the center of the boats of (445 ± 45) nm/s (process 1) and of $r_{s,max}$ = (1800 ± 85) nm/s (process 2).*

The dynamic deposition rate

$$r_{dyn} = \int_0^{40cm} r_s(x)dx \tag{1.17}$$

follows by integrating the static deposition rate $r_\mathrm{s}(x)$ over the entire deposition width.

Figure 1.6 shows the measured static deposition rate $r_\mathrm{s}(x)$ from processes 1 and 2. Process 1 (blue squares) features a maximum static deposition rate of $r_\mathrm{s,max} = (445 \pm 45)$ nm/s in the center of the boats whereas process 2 (green triangles) features a maximum static deposition rate of $r_\mathrm{s,max} = (1800 \pm 85)$ nm/s. Using Eq. (1.17) gives $r_\mathrm{dyn} = (5 \pm 0.2)$ µm×m/min for process 1 and $r_\mathrm{dyn} = (20.6 \pm 0.8)$ µm×m/min for process 2. Both methods thus agree within the error bars. The local distribution of the static deposition rate will be used in Chapter 2 for the simulation of the wafer temperature during evaporation.

Throughout this work several processes are tested and the results are described in the corresponding Chapters. The results presented in this work are obtained with aluminum of a purity of 99.98%. However, using aluminum of purities of 99.999%, which is state of the art in laboratory batch evaporation systems, and of 99.7% did not show a different behavior in investigations of lifetimes and contact resistivities.

1.4. Chapter summary

This Chapter gives a review of the theory of metal-semiconductor contacts, of the screen-printing process, and of the evaporation process. When aluminum and silicon are connected, the valence band forms a barrier. According to the simplest approximation, the barrier height depends on the band gap of silicon, the metal work function of aluminum and the silicon electron affinity. Experimentally a lower barrier height is found. Ohmic contacts are possible by tunneling, which requires highly doped silicon surfaces. The common industrial technology for contacting the rear sides of silicon solar cells is briefly reviewed: An aluminum paste is applied by screen-printing to the silicon surface and a subsequent firing step forms a highly aluminum-doped p^+ region. This region reduces the effective surface recombination velocity at the rear side of the cell. As an alternative to the screen-printing process the evaporation of aluminum is introduced, which is known to form high-quality contacts to silicon solar cells when using laboratory batch systems. For an industrially feasible application, an in-line high-rate evaporation system is presented, where dynamic deposition rates r_dyn between (4.9 ± 0.2) µm×m/min and (20.6 ± 0.8) µm×m/min are achieved.

2. Temperature during aluminum deposition

This Chapter deals with the temperature of silicon wafers and of silicon solar cells during the in-line high-rate evaporation of aluminum. The deposition of aluminum onto silicon wafers leads to an increase in wafer temperature due to the enthalpy of deposition. In order to achieve a high throughput high deposition rates are necessary. These high rates are inevitably leading to elevated wafer temperatures, which may have an impact on solar cell parameters such as the contact resistivity, the passivation quality of dielectric layers, or might result in a wafer bow, which is not tolerable for the module assembly. Therefore the knowledge of the substrate temperature during in-line high-rate aluminum deposition, and hereby especially the knowledge of the peak temperature, is essential for understanding and improving the deposition process. The present Chapter deals with the temperatures that occur during deposition and presents measured and simulated temperatures. The two-dimensional finite-element simulation is based on the heat flows that occur during the deposition. Parts of this Chapter are published in Ref. [42].

2.1. Sample preparation and temperature measurement

For the experiments 156 × 156 mm^2, (1 0 0)-oriented, 220 µm-thick, p-type, B-doped Czochralski-grown silicon wafers (Cz-Si) with a resistivity of 4.7 Ω cm are used. After KOH etching there are three groups of wafers with a thickness of 130 µm, 140 µm, and 180 µm-thick, respectively. In order to obtain single side textured wafers, the rear side of 140 µm-thick planar wafers is protected with a 100 nm-thick plasma-enhanced chemical vapor-deposited silicon nitride (SiN$_x$) layer that has a refractive index $n = 1.9$. Subsequently, single side texturing is done in a KOH based alkaline solution. The final wafer thickness of the single side textured wafers is 130 µm. From SEM images the size of the resulting random pyramids is determined to be in the range of 3 to 5 µm. The silicon nitride mask is removed in a 40% solution of hydrofluoric acid.

Afterwards, 2 and 5 µm-thick aluminum layers are deposited on rear sides of the planar and the textured silicon wafers using the processes from Table 2.1. The dynamic deposition rate is $r_{\mathrm{dyn}} = 5$ µm×m/min for all processes. The wafer temperature during the deposition

Table 2.1.
Tray speed v_{TRAY}, Al layer thickness d, and wafer thickness W of the evaluated processes. The dynamic deposition rate of all processes is $r_{\mathrm{DYN}} = 5$ µm×m/min. The variation in Al layer thickness d is achieved by choosing various tray speeds.

Process	Tray speed v_{tray}[m/min]	Wafer thickness W [µm]	Al layer thickness d [µm]
1	1	180	5
2	2.5	130	2
3	2.5	130 (textured)	2
4	2.5	180	2

process is measured using three thermocouples (*PA1571A* from *datapaq*). A data logger (*Q18* from *datapaq*) moves along with the wafers through the deposition system and stores the temperature data. The thermocouples are fixed to the wafer's front side on the downstream edge of the wafer, where the deposition starts last, i. e. at $x = 0$ in Fig. 1.5. The thermocouples are fixed using a kapton tape. The tape covers about 2% of the wafer's front side, which affects the wafer emissivity and therefore the wafer temperature. We measure the temperature of a wafer with the entire front side covered with kapton tape in order to quantify the influence of the kapton tape on wafer temperature. The measured temperature is 7% higher when measured in K than the temperature of a wafer with only 2% of the front side covered with kapton tape. We thus estimate the tape-induced error in temperature to be less than 1%.

2.2. Experimental results and discussion

We measure the temperature for the processes 1 through 4 listed in Table 2.1 on two wafers each. Each wafer holds three thermocouples. The standard deviation of the six measurements and the tape-induced error define the error bars presented in the following figures. The symbols in Fig. 2.1 represent the measured temperature of 130 (squares) and 180 µm-thick planar Cz-Si wafers (triangles) during deposition of 2 µm-thick Al layers at a dynamic deposition rate of $r_{\mathrm{dyn}} = 5$ µm×m/min. The wafer temperature before deposition is equal to the chamber temperature $T_{\mathrm{chamber}} = 298$ K and increases during deposition within 14 seconds to the peak temperature of (559 ± 12) K for the 130 µm-thick wafer and within 18 seconds to (482 ± 11) K for the 180 µm-thick wafer, respectively. The increase in temperature is caused by the enthalpy of deposition of the evaporated aluminum.

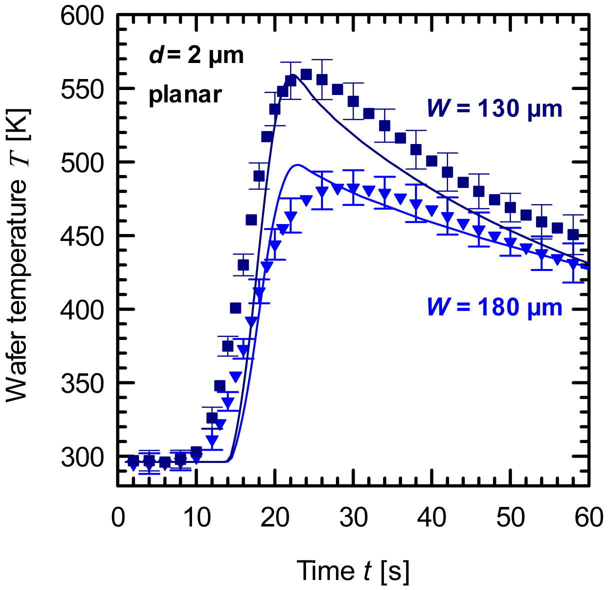

Figure 2.1.: *The symbols represent the measured temperatures of 130 (squares) and 180 µm-thick silicon wafers (triangles) during deposition of a 2 µm-thick Al layer. The measured peak temperatures are (559 ± 12) K for the 130 µm-thick wafer and (482 ± 11) K for the 180 µm-thick wafer, respectively. The solid lines represent simulated temperatures.*

With increasing temperature the heat radiation of the wafer increases. Equality of the heat flows caused by the Al deposition and by the heat radiation is reached at a certain time and thereafter the wafer temperature decreases. The lower heat capacity of the thinner wafer causes the faster temperature increase and the higher peak temperature when compared to the 180 µm-thick Si wafer.

Figure 2.2 shows the temperature of 180 µm-thick silicon wafers during the deposition of 2 (triangles) and 5 µm-thick Al layers (diamonds). The wafer temperature before deposition equals the chamber temperature of $T_{\text{chamber}} = 298$ K. The peak temperatures are (701 ± 14) K for the 5 µm process and (482 ± 11) K for the 2 µm process. The difference in peak temperature is caused by the difference in Al layer thickness.

Figure 2.3 shows the temperature of 130 µm-thick, planar (square) and textured (triangles), silicon wafers during the deposition of a 2 µm-thick Al layer. The deposition results in a peak temperature of (559 ± 12) K for the planar wafer and of (539 ± 13) K for the textured wafer. The temperature of the textured wafer decreases faster than the temperature of the planar wafer. The higher emissivity of the textured wafer causes both the lower peak temperature and the faster decrease in temperature. In conclusion, the wafer temperature during in-line high-rate deposition of aluminum was shown to depend on the wafer thickness (Fig. 2.1), the aluminum layer thickness (Fig. 2.2), and the wafer emis-

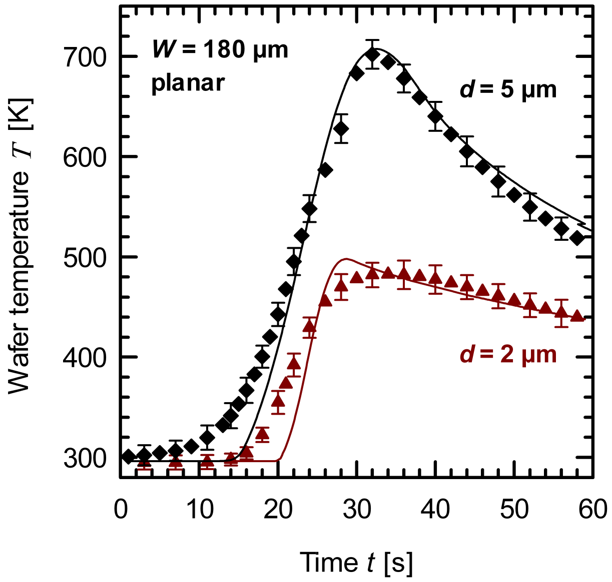

Figure 2.2.: *Measured temperatures of 180 µm-thick silicon wafers during deposition of 2 (triangles) and 5 µm-thick Al layers (diamonds) at a dynamic deposition rate of* $r_{dyn} = 5\ \mu m \times m/min$. *The high deposition rate leads to an increase in wafer temperature caused by the deposition enthalpy of aluminum. The thicker Al layer results in higher temperatures. The solid lines represent simulated temperatures.*

sivity (Fig. 2.3). The wafer emissivity hereby only depends on the front side morphology (textured vs. planar front side). A passivation layer on the wafer's rear or front side might have an impact on the wafer's emissivity and thus on the wafer temperature during the Al deposition. However, no influence on the wafer temperature was observed after applying a 100 nm-thick front and/or rear side passivation layer of SiN_x. This indicates that a 100 nm-thick passivation layer is transparent for the heat radiation of wafers at temperatures < 700 K. At higher temperatures and thus shorter wavelengths however a SiN_x passivation layer might have an impact on the wafer's emissivity and thus on the temperature during Al deposition. Furthermore, the wafer temperature depends on the start temperature T_s, the wafer temperature before the Al deposition starts. In our experiments the wafers are not heated prior to deposition and T_s thus equals the temperature of the deposition system and thus room temperature.

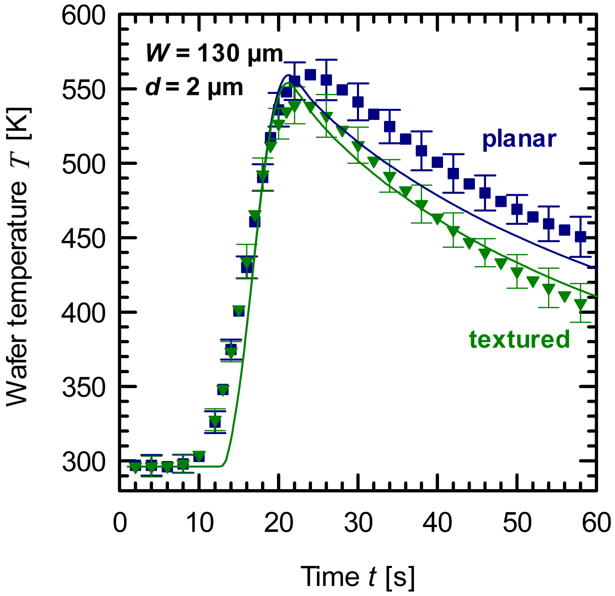

Figure 2.3.: *Measured temperature of 130 µm-thick, planar (squares) and textured (triangles), Cz-Si wafer during deposition of a 2 µm-thick Al layer. The high deposition rate leads to an increase in wafer temperature of up to (559 ± 12) K for the planar wafer and up to (539 ± 13) K for the textured wafer. The temperature decreases according to the emissivity of the wafer. The higher emissivity of the textured wafer causes both the difference in peak temperature and the faster decrease of temperature. The solid lines represent simulated temperatures.*

2.3. Temperature simulation

In this Section the temperature of silicon wafers during in-line high-rate evaporation is calculated. The simulation is based on a simplified model of the heat flows j during evaporation. These heat flows are caused by the enthalpy of deposition of aluminum and heat radiation of the wafer. Figure 2.4 shows a schematic sketch of the heat flows. A silicon wafer of thickness W moves with tray speed v_{tray} through the deposition chamber. Aluminum deposits on the rear side of the wafer and the enthalpy of deposition is released. This leads to an increase in wafer temperature. The wafer's front side radiates heat. This heat is in parts reflected from the deposition chamber and might be reabsorbed by the silicon wafer. In the following Sections, the heat conduction within the wafer and the boundary conditions are discussed and simulated wafer temperatures using two-dimensional finite-element simulations are presented. It will be shown that simulated and measured peak temperatures agree within an uncertainty of 3% when given in K. Finally, the simulation will be used to optimize the deposition process regarding upper temperature

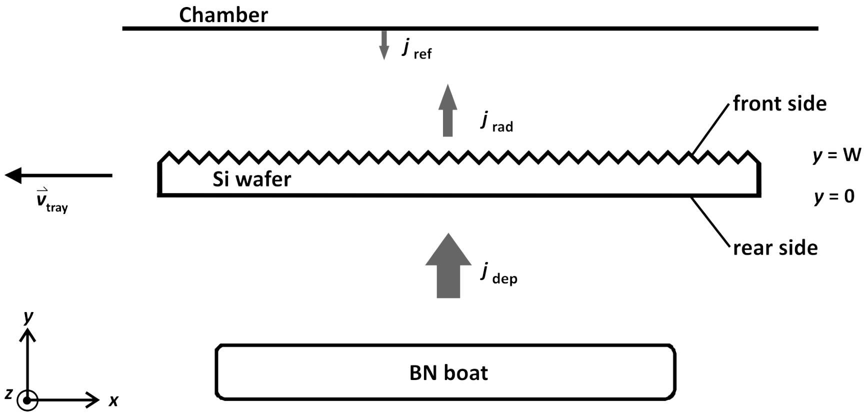

Figure 2.4.: *Model of the heat flows considered in the simulation. The boundary conditions are defined by the heat flows, which are caused by the deposition enthalpy of aluminum* j_{dep}*, the heat radiation of the wafer front side* j_{rad} *and the reflected heat radiation from the chamber to the wafer front side* j_{ref}*.*

limits. An analytical verification of two limiting cases will be presented in Appendix A.

2.3.1. Heat conduction within the wafer

The heat conduction within the wafer is described by the partial differential equation

$$\rho_{\mathrm{Si}}\, C_{\mathrm{Si}}\,(T)\frac{\partial T}{\partial t} - \vec{\nabla}\,(k(T)\,\vec{\nabla}(T)) = 0, \tag{2.1}$$

where $\rho_{\mathrm{Si}} = 2.336$ g/cm^3 is the density of silicon, $C_{\mathrm{Si}}(T)$ is the temperature dependent heat capacity of silicon [43], $\vec{\nabla}=(\frac{\partial}{\partial x}, \frac{\partial}{\partial y})$ is the vector differential operator, and $k(T)$ is the temperature dependent thermal conductivity of silicon [44]. The right-hand side equals zero as there are no heat sources in the wafer.

2.3.2. Boundary conditions

Boundary conditions are required for solving Equation (2.1). In the following three heat flows that define the boundary conditions are discussed.

Heat flow caused by enthalpy of deposition

The enthalpy of deposition is released during the evaporation process and leads to an increase in wafer temperature. The heat flow by the enthalpy of deposition

$$j_{\mathrm{dep}}(x) = \Delta H_{\mathrm{Al}}\,\rho_{\mathrm{Al}}\,r_{\mathrm{s}}(x) \tag{2.2}$$

enters the wafer at $y = 0$ and depends on the position x, the enthalpy of deposition $\Delta H_{\mathrm{Al}} = 11.25$ kJ/g, and the density of aluminum $\rho_{\mathrm{Al}} = 2.7$ g/cm^3. Here, $r_{\mathrm{s}}(x)$ is the static deposition rate shown in Fig. 1.6. Shortly after starting the Al deposition the rear side of the silicon wafer will be covered with aluminum. Aluminum is known to have a low emissivity of (4 ± 2)% in the spectral range of 1 to 20 µm [45]. This holds approximately in the temperature range of 300 to 760 K [45,46]. Additionally, the heated boron nitride boats are partially covered with an Al layer during the evaporation process. Thus the heat radiation from the boats is not expected to significantly increase the wafer temperature and this heat flow is neglected.

Heat radiation of the wafer

We consider only the heat radiation flux leaving the wafer's front side at $y = W$, because the rear side is covered with an aluminum layer of low emissivity [45,46] and the other two sides have a small surface area compared to the front side. The heat flux

$$j_{\mathrm{rad}}(T) = \varepsilon(T)\,\sigma\,T^4 \tag{2.3}$$

leaving through the front side depends on the emissivity $\varepsilon(T)$, the Stefan-Boltzmann constant $\sigma = 5.67\times10^{-8}$ W/(m^2 K^4) and the temperature T. We calculate the emissivity

$$\varepsilon(T) = \frac{\int_0^\infty \varepsilon_\lambda(\lambda,T)\,j_{\mathrm{Planck}}(\lambda,T)\,\mathrm{d}\lambda}{\int_0^\infty j_{\mathrm{Planck}}(\lambda,T)\,\mathrm{d}\lambda} \tag{2.4}$$

of the metallized wafer [47], where $\varepsilon_\lambda(\lambda,T)$ is the spectral emissivity and $j_{\mathrm{Planck}}(\lambda,T)$ is the spectral black body radiation calculated with Planck's law [48]:

$$j_{\mathrm{Planck}}(\lambda,T) = \frac{2hc^2}{\lambda^5}\,\frac{1}{e^{hc/kT}-1}. \tag{2.5}$$

Equation (2.4) requires the spectral emissivity $\varepsilon_\lambda(\lambda,T)$ of the metallized silicon wafer to be known. The spectral emissivity equals the spectral absorption [49]. Therefore, the spectral absorption of a metallized silicon wafer is calculated in accordance to the model from Ref. [50]. This model was used from Brendel et al. to calculate the absorption of a silicon wafer. We extend the model to calculate both, the absorption of the silicon wafer and of the Al layer on the rear side.

Figure 2.5 gives a schematic sketch of a silicon wafer with a metallized rear side. The wafer has the thickness W, the refraction index $n_{\mathrm{Si}}(\lambda,T)$, and the absorption coefficient $\alpha_{\mathrm{Si}}(\lambda,T)$. The absorption model also uses the front side transmittance T_{f}. The transmittance is determined to be $T_{\mathrm{f}} = 0.7$ for a planar and $T_{\mathrm{f}} = 0.9$ for a textured wafer using the Monte Carlo ray tracing program SUNRAYS [51]. Using a spectrophotometer (*Cary 5000* from *Varian*) the internal rear reflectance at the evaporated Al layer is determined to R_{Al}

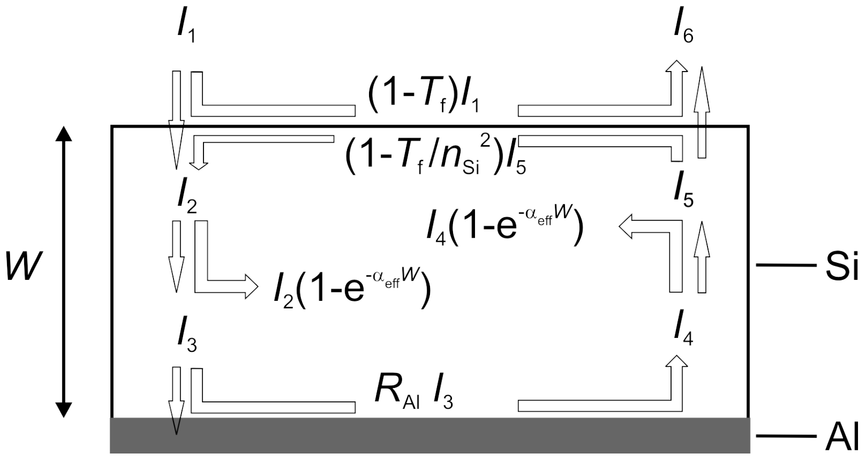

Figure 2.5.: *Schematic representation of the silicon wafer with an aluminum layer on the rear side and the light intensities* I_i*. We describe the optical behavior of the front side by a transmittance* T_f *and the optical behavior of the rear side by a reflectance* R_{Al}*. The silicon wafer has the refraction index* $n_{Si}(\lambda, T)$ *and the absorption constant* $\alpha_{Si}(\lambda, T)$*.*

= 0.74 for the wavelength range of 1 to 2.5 µm and this value is assumed as the internal rear reflectance for wavelengths up to 20 µm. The transmittance T_{Al} = 1 - R_{Al} into the aluminum layer is identical to the optical absorption in the metal.

The energy flow diagram with the six intensities I_{i} shown in Fig. 2.5 defines a linear system of six equations. The energy fluxes are conserved and indicated by the arrows. Each node with two fluxes adding or subtracting yields one of the equations listed below. The six linear equations are:

$$I_1 = 1 \tag{2.6}$$

$$I_2 = I_1 T_{\mathrm{f}} + I_5 \left(1 - \frac{T_{\mathrm{f}}}{n_{\mathrm{Si}}(\lambda, T)^2}\right) \tag{2.7}$$

$$I_3 = I_2 e^{-\alpha_{\mathrm{eff}}(\lambda,T)W} \tag{2.8}$$

$$I_4 = I_3 R_{\mathrm{Al}} \tag{2.9}$$

$$I_5 = I_4 e^{-\alpha_{\mathrm{eff}}(\lambda,T)W} \tag{2.10}$$

$$I_6 = I_1(1 - T_{\mathrm{f}}) + \left(\frac{I_5 T_{\mathrm{f}}}{n_{\mathrm{Si}}(\lambda, T)^2}\right) \tag{2.11}$$

The spectral absorption

$$A_{\text{Si}}(\lambda,\,T)=\frac{(e^{\alpha_{\text{eff}}(\lambda,T)W}-1)(e^{\alpha_{\text{eff}}(\lambda,T)W}+R_{\text{Al}})\,n_{\text{Si}}^2(\lambda,T)\,T_{\text{f}}}{e^{2\alpha_{\text{eff}}(\lambda,T)W}\,n_{\text{Si}}^2(\lambda,T)-n_{\text{Si}}^2(\lambda,T)\,R_{\text{Al}}+R_{\text{Al}}\,T_{\text{f}}} \tag{2.12}$$

in the silicon follows from the six Equations (2.6) to (2.11) similar to Ref. [50]. The absorption in the Al layer is given by

$$A_{\text{Al}}(\lambda,\,T)=\frac{e^{\alpha_{\text{eff}}(\lambda,T)W}(1-R_{\text{Al}})\,n_{\text{Si}}^2(\lambda,T)\,T_{\text{f}}}{e^{2\alpha_{\text{eff}}(\lambda,T)W}\,n_{\text{Si}}^2(\lambda,T)-n_{\text{Si}}^2(\lambda,T)\,R_{\text{Al}}+R_{\text{Al}}\,T_{\text{f}}}. \tag{2.13}$$

The angle-averaged effective absorption coefficient $\alpha_{\text{eff}}\ (\lambda,T)$ is defined in [52] by

$$e^{-\alpha_{\text{eff}}(\lambda,T)W}=2\int_0^{\pi/2}\sin(\vartheta)\cos(\vartheta)e^{-\alpha_{\text{Si}}(\lambda,T)W}\text{d}\vartheta. \tag{2.14}$$

The spectral emissivity $\varepsilon_\lambda(\lambda,T)$ is calculated (see Eq. (2.4)) by

$$\varepsilon_\lambda(\lambda,T)=A_{\text{Si}}(\lambda,T)+A_{\text{Al}}(\lambda,T). \tag{2.15}$$

At high carrier concentrations, which occur in highly doped silicon or at high temperatures, the free carriers change the refraction index $n_{\text{Si}}(\lambda,T)$ and the absorption coefficient $\alpha_{\text{Si}}(\lambda,T)$ of silicon [25, 53, 54]. In the following the impact of the free carrier absorption (FCA) on the optical parameters of silicon is discussed.

A typical upper limit of base doping in silicon solar cells is $N_{\text{A}}=3\times10^{16}$ cm^{-3}. We thus consider doping densities of up to $N_{\text{A}}=3\times10^{16}$ cm^{-3} at a maximum temperature of $T=800$ K. According to Refs. [55–57] the refraction index is not significantly changing in this range. In the following the values of $n_{\text{Si}}(\lambda)$ of intrinsic silicon given in Ref. [58] are thus used. In order to determine the impact of the FCA on the absorption coefficient we use the parameterization

$$\alpha_{\text{FCA}}=\frac{q^3\lambda^2}{4\pi^2\varepsilon_0c^3n_{\text{Si}}(\lambda)}\left(\frac{n}{m_{\text{n}}^*\mu_{\text{n}}(n,T)}+\frac{p}{m_{\text{p}}^*\mu_{\text{p}}(p,T)}\right) \tag{2.16}$$

that is introduced in Refs. [52–54], where $q=1.6\times10^{19}$ C is the elementary charge, n and p are the carrier densities of electrons and holes, respectively, $\varepsilon_0=8.85\times10^{12}$ C/(V m) is the vacuum permittivity, $c=3\times10^8$ m/s the speed of light in vacuum, $m_{\text{n}}{}^*=2.3\times10^{-31}$ kg and $m_{\text{p}}{}^*=3.3\times10^{-31}$ kg are the effective electron and hole mass, respectively, and $\mu_{\text{n}}(n,T)$ and $\mu_{\text{p}}(p,T)$ are the carrier mobilities of electrons and holes, respectively. The dependence of the mobility on doping density and temperature is taken into account by using the mobility model presented by Klaassen [59, 60]. The temperature dependence of the intrinsic carrier concentration

$$n_\mathrm{i} = \sqrt{N_\mathrm{c}N_\mathrm{v}}\left(\frac{E_\mathrm{g}}{kT}\right) \tag{2.17}$$

is also taken into account, which is given in Ref [61], where N_c and N_v are the temperature-dependent effective densities of states in the conduction and valence band, respectively, E_g = 1.12 eV is the bandgap of silicon, and $k = 8.6\times10^5$ eV/K is the Boltzmann constant. Using Equations (2.12) to (2.17) the spectral absorption of a 300 µm-thick, metallized wafer with a doping density of $N_\mathrm{A} = 3\times10^{16}$ cm^{-3} at a temperature of $T = 800$ K is calculated.

The absorption which is calculated by taking the FCA into account is in excellent agreement with the absorption, which is calculated using the optical parameters of intrinsic silicon at 300 K given in Ref. [61]. Thus, the free carrier absorption for doping densities up to $N_\mathrm{A} = 3\times10^{16}$ cm^{-3} and for temperatures up to 800 K and thus intrinsic carrier concentrations of $\sim 1\times10^{17}$ cm^{-3} is ignored in the emissivity model and the optical parameters of intrinsic silicon at 300 K are used.

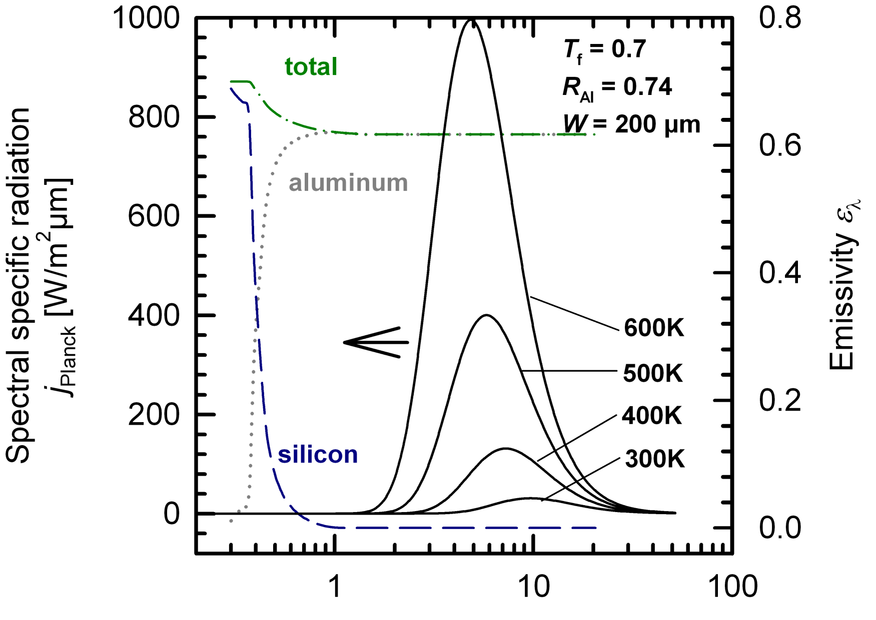

Figure 2.6.: *Spectral specific radiation of a black body and spectral emissivity of a 200 µm-thick metallized planar silicon wafer. The solid lines represent the radiation, which is strongly increasing with increasing temperature according to Planck's law (Eq. (2.5)). The dotted line represents the emissivity of the Al layer. The emissivity of the silicon (dashed line) is dominant at sub-band gap wavelengths. The total emissivity (dashed-dotted) of the metallized planar wafer* (T_f = *0.7) in the wavelength range of 1 to 20 µm is* ε_λ = *0.61.*

Please note that we consider the total emissvity of a metallized wafer and that the FCA might have an influence on the emissivity of a bare silicon wafer with a doping density of $N_\mathrm{A} = 3\times10^{16}$ cm^{-3} at a temperature of $T = 800$ K. Figure 2.6 shows the calculated spectral emissivity $\varepsilon_\lambda(\lambda)$ of a metallized silicon wafer in the wavelength range of 300 nm to 20 µm and for temperatures up to 800 K. The emissivities of the silicon wafer and of the Al layer are also shown. According to Eq. (2.4) the emissivity model gives $\varepsilon(T) = 0.61$ for a metallized planar and $\varepsilon(T) = 0.77$ for a metallized textured wafer in the temperature range from 300 K to 800 K.

Reflected heat radiation

The heat flux $j_\mathrm{rad}(T)$ (see Eq. (2.3)) reduces the wafer temperature. Nevertheless, a significant part of the radiated heat is reflected from the deposition chamber and re-absorbed by the wafer. This heat flux

$$j_\mathrm{ref}(T) = R\, j_\mathrm{rad}(T) \tag{2.18}$$

is accounted for in the boundary conditions by reducing the wafer emissivity (see Eq. (2.4)) by (1-R), which leads to an effective emissivity $\varepsilon_\mathrm{eff}(T) = (1\text{-}R)\ \varepsilon(T)$.

2.3.3. Two-dimensional finite-element simulation

The two-dimensional differential Equation (2.1) of heat conduction in the x-y-plane of the silicon wafer has time-varying boundary conditions (2.2), (2.3), and (2.18). Such partial differential equations can only be solved analytically in special cases. The standard procedure is to use a numerical approximation. In this work the finite-element partial differential equation solver COMSOL version 3.5a is used to simulate the wafer temperature $T(x,y)$.

The solid line in Fig. 2.7 shows the simulated temperature of a textured, 130 µm-thick Cz-Si wafer during deposition of a 2 µm-thick Al layer (see also Fig. 2.3). The images in Fig. 2.7 show the temperature distribution in the silicon wafer during the deposition process. Due to the high thermal conductivity of silicon the temperature gradient in vertical direction of the 130 µm-thick wafer is negligible. We observe a maximum temperature difference in horizontal direction of 134 K at a fixed time. The heat conduction within the wafer causes different peak temperatures on the upstream edge and on the downstream edge of the wafer in direction of sample flow. When the deposition starts on the upstream edge, heat is conducted to the downstream edge of the wafer and leads to an elevated temperature. This leads to higher peak temperatures of the downstream edge of the wafer during the Al deposition. The deposition of a 2 µm-thick Al layer onto a 130 µm-thick, textured wafer leads to simulated peak temperatures of 518 K (upstream) and of 553 K

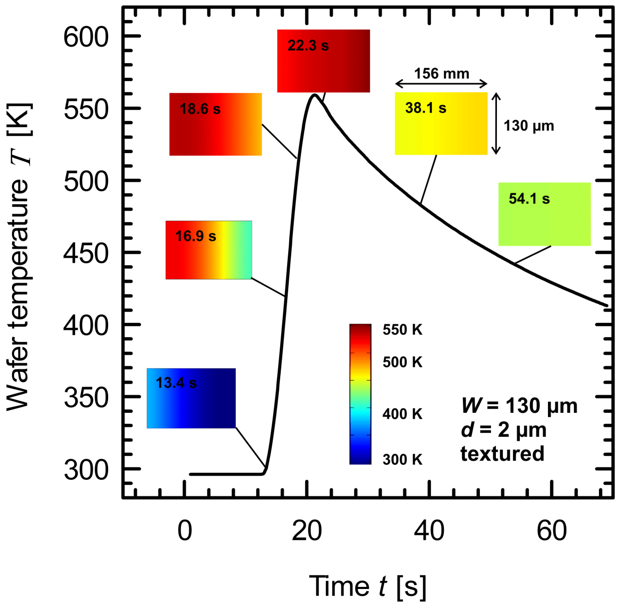

Figure 2.7.: *Simulated temperature of a 130 µm-thick, textured, Cz-Si wafer during deposition of a 2 µm-thick Al layer. The images show the temperature of the wafer at certain times. Due to the high ratio of wafer length to wafer thickness only the temperature gradient in direction of wafer length is visible.*

(downstream). This difference is also observed in temperature measurements. In this work simulated and measured peak temperatures of the downstream edge of the wafer are presented since the maximum peak temperature of the wafer is of interest.

2.4. Comparison of measured and simulated temperatures

Figure 2.8 shows measured and simulated temperatures of a 130 µm-thick Cz-Si wafer during the deposition of a 2 µm-thick Al layer. The symbols represent the measured temperature of a wafer with textured front side. The solid lines represent the temperatures, which are simulated with reflectivities R (see Eq. (2.18)) of 0, 0.3, 0.5, and 0.7. We use this to fit the reflectivity of the chamber. $R = 0.5$ reproduces the measured temperatures with the highest accuracy. In the following we thus use effective emissivities of $\varepsilon_{\text{eff}}(T) = 0.5\ \varepsilon(T)$, which results in $\varepsilon_{\text{eff}} = 0.305$ for a metallized planar and $\varepsilon_{\text{eff}} = 0.385$ for a metallized textured wafer in the temperature range from 300 to 800 K. The solid lines in Figs. 2.1-2.3 represent the simulated temperatures of the deposition processes shown in Table 2.1. The measured wafer temperatures of the processes 1-4 increase in the first 3 seconds by (13.7 ± 6.2) K whereas the simulated increase in temperature is (68.7 ± 28.3) K. This difference is caused by the heat radiation from the boron nitride boats before the deposition starts and when the wafer rear side is not yet covered with an Al layer of high reflectivity. This effect

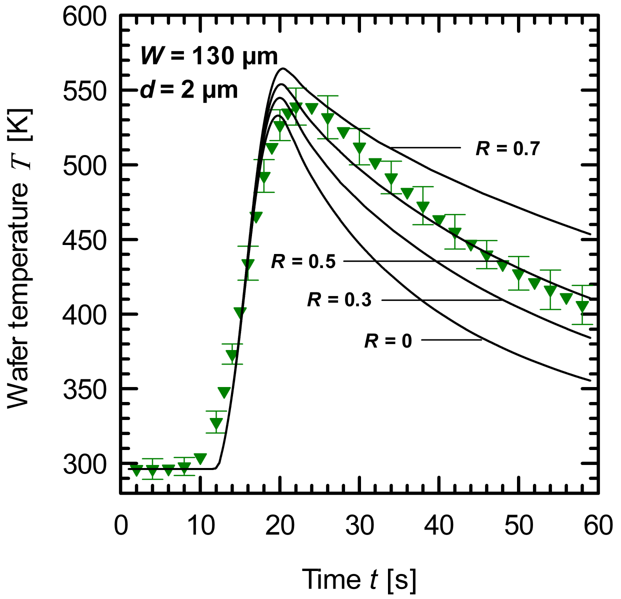

Figure 2.8.: *Measured and simulated temperatures of a 130 µm-thick Cz-Si wafer during deposition of a 2 µm-thick Al layer. The symbols represent the measured temperature of a textured wafer. The solid lines represent simulated temperatures with various reflectivities R of the chamber.*

is not considered in our simulation. Nevertheless, measured and simulated temperatures agree within 10% at all times and the measured and simulated peak temperatures agree within 3%. Table 2.2 summarizes the measured and simulated peak temperatures.

TABLE 2.2.
MEASURED AND SIMULATED PEAK TEMPERATURES T_{PEAK} DURING DEPOSITION FOR THE DIFFERENT PROCESSES ACCORDING TO TABLE 2.1.

Process	Wafer thickness W [µm]	Al layer thickness d [µm]	Measured peak temperature T_{peak} [K]	Simulated peak temperature T_{peak} [K]
1	180	5	701 ± 14	707
2	130	2	559 ± 12	559
3	130 (textured)	2	539 ± 13	553
4	180	2	482 ± 11	497

2.5. Temperature limits

Typically, solar cells have a maximum temperature they withstand since high temperatures may have a detrimental impact on relevant parameters such as the quality of passivation layers, wafer bow, or spiking. In opposite, other applications require high temperatures. For example the formation of aluminum doped p^+-type regions needs temperatures above the eutectic temperature of the Al-Si system of 850 K. Thus, it is necessary to adapt the evaporation process to the specific solar cell. In this Section, based on theoretical considerations, various evaporation processes are presented, which have various temperature limits.

2.5.1. Reducing the wafer temperature during evaporation

Specific solar cell types such as back contact cells require Al layers of up to 20 µm thickness [62]. The deposition of thicker Al layers leads to increased wafer temperatures during the process (see Fig. 2.2). Using thinner silicon wafers also leads to increased wafer temperatures during evaporation (see Fig. 2.1). Elevated temperatures may have a detrimental impact on relevant cell parameters. In the following various processes that resulted in a 20 µm-thick Al layer are described and it is shown that by choosing optimum deposition parameters the wafer temperature is significantly reduced. Table 2.3 summarizes the deposition parameters. Processes 1 and 2 feature the measured distribution of the local static deposition rate shown in Fig. 2.9 (squares). Process 1 is a single deposition process whereas process 2 represents a multi pass process, simulating a deposition system with various deposition chambers, where the 20 µm-thick Al layer is applied in 4 depositions of 5 µm each. Process 3 features a constant static deposition rate of 225 nm/s on the coating area of width $l = 37$ cm shown in Fig. 2.9 (solid line). In practice, this constant static deposition rate might be realized by two Al wires that are steered onto the evaporation

Table 2.3.
Number of deposition chambers, tray speed v_{tray}, and maximum static deposition rate $r_{\mathrm{s,max}}$. The dynamic deposition rate is $r_{\mathrm{dyn}} = 5$ µm×m/min and the deposited Al layer thickness is $d = 20$ µm×m/min.

Process	Number of deposition	Tray speed v_{tray} [m/min]	Maximum static deposition rate $r_{\mathrm{s,max}}$ [nm/s]
1	1	0.25	445
2	4	1	445
3	1	0.25	225

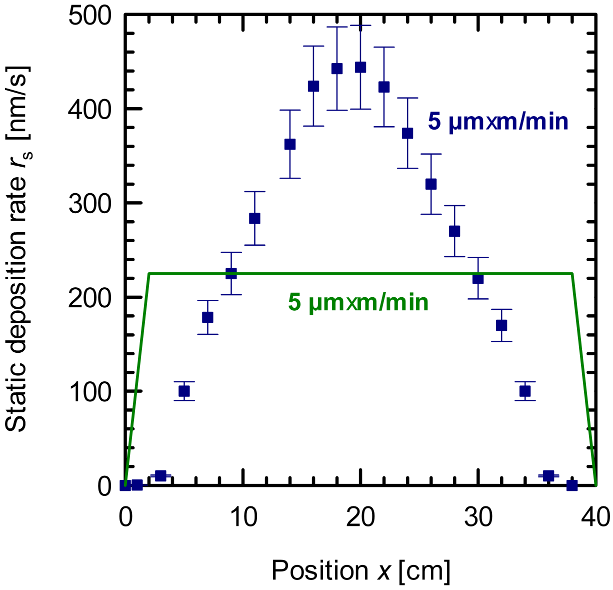

Figure 2.9.: *Local distribution of the static deposition rate $r_s(x)$ in the deposition chamber. The dynamic deposition rate r_{dyn} of both processes is 5 µm×m/min. The width l of the coating area for the measured process (squares) in direction of sample flow is determined to be (35 ± 2) cm with a maximum static deposition rate $r_{s,max}$ in the center of the boats of (445 ± 45) nm/s. The optimized process features a constant static deposition rate of 225 nm/s on the coating area of width $l = 37$ cm.*

boat or by two evaporation boats that are positioned at a certain distance in x-direction (see Fig. 1.5). Then, the optimized static deposition rate would result from the superposition of the two single distributions.

Multi deposition process

First, we consider the single deposition process 1 and the multi pass process 2. Figure 2.10 shows the simulated temperature of textured, 180 µm-thick wafers during the deposition of a 20 µm-thick Al layer with the processes 1 and 2 from Table 2.3. The deposition of the aluminum by process 1 leads to a peak temperature of 876 K (solid green line). This temperature is probably not acceptable in solar cell production [63]. Process 2 leads to acceptable wafer temperatures of up to 720 K (solid blue line) and has a 4 times higher tray speed and thus throughput. However, a deposition system with 4 deposition chambers results in a higher foot print and invest.

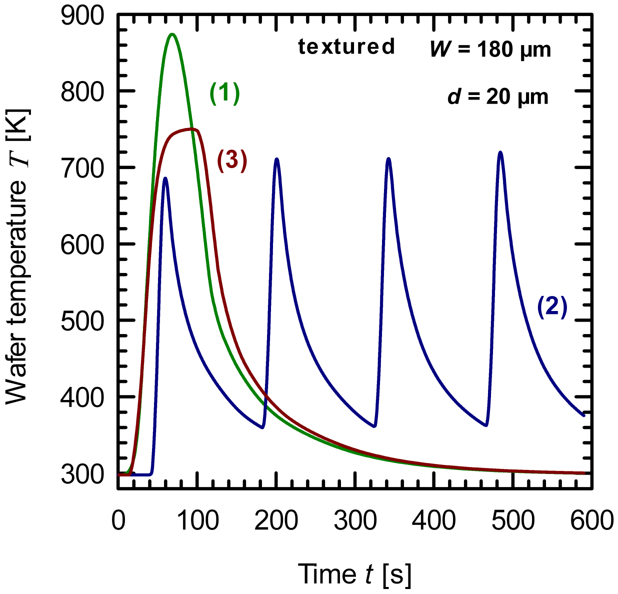

Figure 2.10.: *Temperatures of textured, 180 µm-thick Cz-Si wafers during deposition of a 20 µm-thick Al layer at* r_{dyn} = *5 µm×m/min by different processes. Processes 1 and 3 are single deposition processes whereas process 2 represents a multi pass process, simulating a deposition system with various deposition chambers. Processes 1 and 3 have different distributions of static deposition rates.*

Optimized static deposition rate

In this Section, the deposition process 3 (see Tab. 2.3) with a constant static deposition rate of 225 nm/s on the coating area of width $l = 37$ cm is considered. Similar to process 1 process 3 features a dynamic deposition rate of 5 µm×m/min and is a single deposition process. Thus it would result in the same throughput of processed solar cells per time.

Figure 2.10 shows the simulated temperature of a textured, 180 µm-thick wafer during the deposition of a 20 µm-thick Al layer using process 3, resulting in a peak temperature of 749 K. For explaining the different peak temperatures of process 1 and 3 we define a local upper temperature limit T_{lim}, which is reached when $j_{\mathrm{dep}}\,(x) = j_{\mathrm{rad}}\,(x)$ - $j_{\mathrm{ref}}\,(x)$. Equations (2.2), (2.3), and (2.18) thus yield the upper temperature limit

$$T_{\mathrm{lim}} = \sqrt[4]{\frac{\Delta H_{\mathrm{Al}} \rho_{\mathrm{Al}} r_{\mathrm{s,max}}}{\varepsilon_{\mathrm{eff}}(T)\sigma}} \tag{2.19}$$

for the local wafer temperature during in-line evaporation. According to Eq. (2.19) only the maximum static deposition rate $r_{\mathrm{s,max}}$ and the effective emissivity $\varepsilon_{\mathrm{eff}}$ define T_{lim}. Please note that Eq. (2.19) only applies at negligible heat conduction within x-direction of the wafer. T_{lim} thus defines the maximum possible temperature during the deposition process. The upper temperature limit T_{lim} is 887 K for process 1 and 749 K for process 3. Thus, choosing the distribution of the local static deposition rate of process 3 reduces the maximum possible temperature by 138 K at fixed throughput.

Minimized reflectivity of chamber

Reducing the reflectivity R of the chamber reduces the heat flux to the wafer and thus the wafer temperature during the Al deposition process. In the following it is assumed that the reflectivity of the chamber might be reduced to zero. In practice, the reflectivity of the chamber might be reduced by adding textured (rough) sheets to the evaporation chamber. The effective emissivity $\varepsilon_{\mathrm{eff}} = (1\text{-}R)\ \varepsilon$ of a textured wafer thus increases to $\varepsilon_{\mathrm{eff}} = 0.77$. Figure 2.11 shows the temperature of 180 µm-thick textured wafers during Al depositions using processes 1 to 3 from Table 2.3 with $R = 0$. The peak temperatures are 740 K (process 1), 642 K (process 2), and 636 K (process 3). Reducing the reflectivity from 50% to 0% thus significantly reduces the peak temperatures by 136 K (1), 78 K (2), and 113 K (3), respectively. Combining the optimized static deposition rate (process 3) with the reduced reflectivity results in temperatures below 700 K that have promise to be acceptable for back contact solar cells [63].

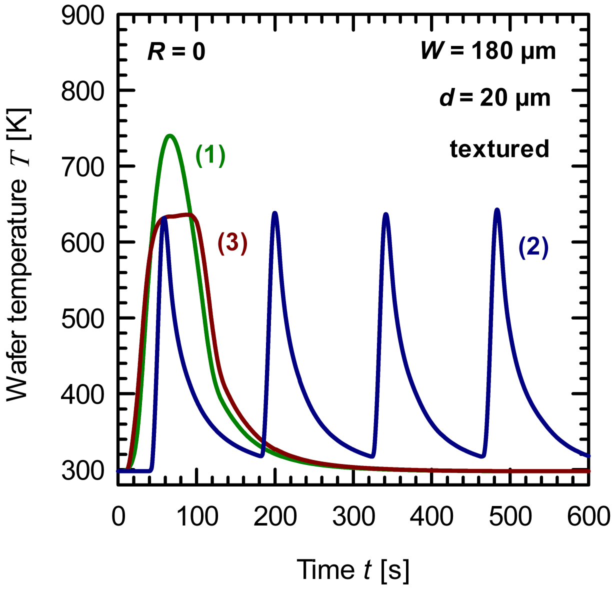

Figure 2.11.: *Temperatures of textured, 180 µm-thick Cz-Si wafers during deposition of a 20 µm-thick Al layer at* $r_{dyn} = 5\ \mu\mathrm{m}\times\mathrm{m/min}$ *by different processes. Processes 1 and 3 are single deposition process whereas process 2 represents a multi pass process, simulating a deposition system with various deposition chambers. Processes 1 and 3 have different distributions of static deposition rates. The reflectivity of the chamber is assumed to be R=0.*

2.5.2. Increasing the wafer temperature during deposition

While some samples degrade when exposed to too high temperatures, some processes require high temperatures. For example, the formation of highly aluminum-doped silicon (Al-p^+) regions requires temperatures above the eutectic temperature of the Al-Si system of 850 K. This work also examines the formation of Al-p^+ regions by in-line high-rate evaporation of aluminum (see Chapter 5). We find that temperatures above 1050 K are required for the formation of a closed Al-p^+ region and that a minimum Al layer thickness of 20 µm is necessary to achieve these temperatures. However, the deposition of thick Al layers does not seem to be cost-effective, since thick Al layers lead to increased costs of the consumables and they also result in a reduced throughput of the in-line deposition system. Using thinner silicon wafers and / or heating the wafers prior to deposition might reduce the Al layer thickness, which is required for the formation of aluminum-doped silicon (Al-p^+) regions. Figure 2.12 shows the aluminum layer thickness, which is required to obtain a wafer temperature of $T = 1050$ K as a function of the wafer thickness W. Reducing the wafer thickness from 270 µm to 100 µm reduces the required Al layer thickness from 28 µm to 10 µm. In addition, the wafer temperature before Al deposition could be increased by integrating a heater into the deposition system and thus the required amount of aluminum could further be reduced. For example, heating the wafers to 800 K reduces the required amount of aluminum that is necessary for achieving temperatures of 1050 K by factor 2.

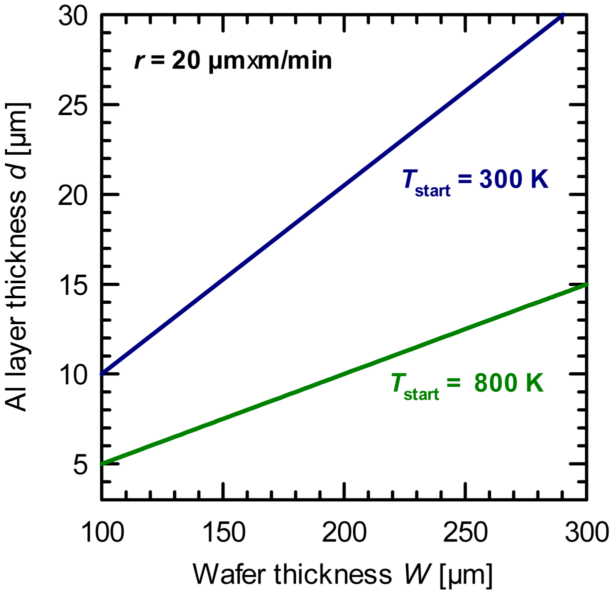

Figure 2.12.: *Al layer thickness required to obtain a substrate temperature T of 1050 K as a function of the wafer thickness W, calculated for a starting temperature of 300 K (blue line) and 800 K (green line), respectively. The dynamic deposition rate is $r_{dyn} = 20$ µm×m/min.*

2.6. Chapter summary

The present Chapter dealt with the temperature of silicon wafers during in-line high-rate evaporation of aluminum. The temperatures were experimentally found to depend on the wafer thickness W, the aluminum layer thickness d, and on the wafer emissivity ε. Depending on the investigated deposition parameters the investigated wafer temperatures are in a wide range of 497 K to 1050 K. The heat-flows during deposition could be shown to be reducible to the contributions of: (i) the enthalpy of deposition, (ii) the heat radiation of the wafer's front side, and (iii) the reflected heat flow from the chamber. Two-dimensional finite-element simulations that are based on these heat flows reproduce the measured peak temperatures with an accuracy of 97%. The simulation of the wafer temperature during in-line evaporation enables the optimization of the deposition parameters regarding low or high temperatures with respect to process requirements.

3. Bow after aluminum deposition

This Chapter presents the bow of silicon wafers after in-line high-rate evaporation of aluminum. In order to achieve a high throughput high deposition rates are necessary. The previous Chapter showed that these high rates are inevitably leading to elevated wafer temperatures due to the enthalpy of deposition. The different thermal expansions of the silicon substrate and the aluminum layer build up thermo mechanical stresses that lead to a bending of the solar cell after cooling down to room temperature [64–67]. This wafer bow represents an issue in wafer handling and module assembly [67] and may result in cracks and thus reduced module power output [68]. It is therefore necessary to optimize the in-line evaporation process with regard to the wafer bow.

3.1. Sample preparation and bow measurement

For the experiments 156 × 156 mm^2, full-square, single-crystalline, (1 0 0)-oriented and 240 µm-thick p-type Czochralski grown silicon wafers with a resistivity of 1.9 Ω cm are used. By varying the etching time in a KOH solution the wafers are thinned to 130 µm, 150 µm, 170 µm, 190 µm, 210 µm, and 230 µm. From the wafers with edge length $b = 156$ mm we cut wafers of edge lengths 125 mm and 100 mm having thickness values from 130 µm to 230 µm. The reduction of the edge lengths is done by an infrared disc laser with a wavelength of 1030 nm and a pulse length of 1 µs. Subsequently, we deposit Al layers of thickness $d = 2$ µm, 5µm, 10 µm, and 15 µm-thick on the silicon wafers at a dynamic deposition rate of $r_{\mathrm{dyn}} = 5$ µm×m/min. Table 3.1 summarizes the deposition processes.

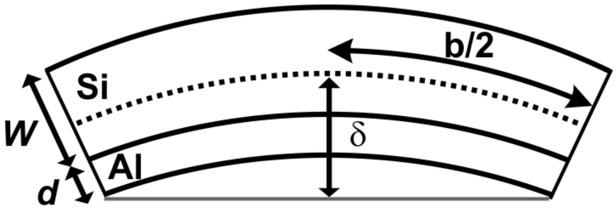

Figure 3.1.: *Sketch of a silicon wafer of thickness W contacted with an aluminum layer of thickness d. The stress-free wafer edge length is b. The dashed line represents the neutral axis. The bowing is represented by δ, the deflection from the neutral axis to the plane connecting the wafer edges.*

Table 3.1.
Wafer thickness W, Al layer thickness d, wafer edge length b, and simulated peak temperature T_{peak} of the deposition processes. The dynamic deposition rate of all processes is $r_{\text{dyn}} = 5$ µm×m/min. The variation in Al layer thickness d is achieved by choosing various tray speeds v_{tray}.

Process	6 wafer thickness values W [µm]	Wafer edge length b [mm]	Aluminum layer thickness d [µm]
1	130 to 230	156	2
2	130 to 230	100, 125, 156	5
3	130 to 230	100, 125, 156	10
4	130 to 230	100, 125, 156	15

Directly after the deposition of the Al layers we measure the bow δ. The wafer bow is defined as the deflection from the neutral axis to the plane connecting the wafer edges, as shown in Fig 3.1. For the bow measurement the wafers stand upright on millimeter paper. The upright position of the wafers reduces the influence of gravity on the measurement. We estimate the error of the measured bow to be 0.5 mm.

In order to investigate the wafer bow as a function of the temperature during thermal cycling tests we use the digital image correlation technique (DIC) with a stereo-camera system [69]. This method requires a random speckle pattern on the inspected surface, which we apply to the Al layers with spray paint. Stereo-images of these patterns allow the calculation of 3-dimensional representations of the surfaces and thus of the wafer bow. The metallized wafers are placed in a climate chamber in an upright position parallel to the window of the climate chamber and thermocouples are attached to both wafer sides. The wafers are heated in the climate chamber to temperatures of 373 K and then cooled down to 253 K. The heating- and cooling rates are 0.25 K per minute. The wafer side that features the aluminum layer faces the window so that the speckled surfaces are visible from outside the chamber and the measurement region is illuminated by a cold light source. Two charge-coupled device (CCD) cameras mounted outside the climate chamber simultaneously take pictures of the speckled surface of the wafers. Both images are then correlated by a computer algorithm and the wafer bow δ as a function of temperature is continuously measured using the image correlation. A more detailed description of the method can be found in Refs. [69–71].

3.2. Temperature during aluminum deposition

The wafer bow occurs due to the difference in thermal expansion and due to the elevated substrate temperatures during the deposition. Thus the deposition temperature is of interest. We simulate the wafer temperature during the deposition process using the two-dimensional finite-element simulation tool from Chapter 2.

Figure 3.2 shows the simulated peak temperatures T_{peak} of Si wafers during Al deposition with all processes from Tab. 3.1 as a function of the ratio of the Al layer thickness d to the wafer thickness W for wafer edge lengths of $b = 156$ mm. The peak temperatures increase with increasing ratio of Al layer thickness d to wafer thickness W. The upper temperature limit for large d/W is apparent. This limit is reached if equilibrium of the heat flows caused by deposition and radiation is established (see Equation 2.19). Reducing the edge length from $b = 156$ mm to $b = 100$ mm changes the wafer temperature by less than 2 K. In the following we thus only simulate temperatures of wafers with edge length 156 mm.

When the deposition starts at the upstream edge of the wafer heat is conducted to the downstream edge, which is not yet covered with aluminum. This heat conduction leads to higher peak temperatures at the downstream edge, as shown in Fig. 3.2. In the following we consider both temperatures, from upstream and downstream edge of the wafer, as lower and upper limits of the wafer temperature and use this temperatures for the calculation of the upper and lower limit of the wafer bow.

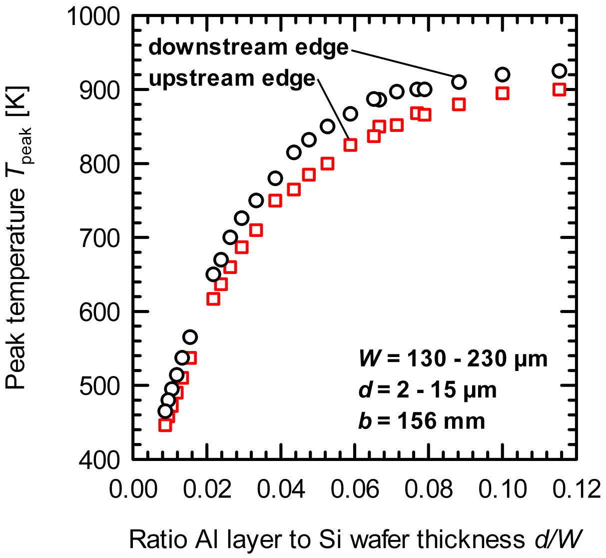

Figure 3.2.: *Simulated peak temperatures during Al deposition as a function of the ratio of Al layer thickness d to wafer thickness W. The data represent all processes shown in Tab. 3.1. The squares represent temperatures of the upstream edge of the wafer, which is first coated with an Al layer during the in-line evaporation process. The circles represent temperatures of the downstream edge of the wafer.*

3.3. Experimental results and modeling of the wafer bow

The elastic bending of a thin layer of thickness d on a thick substrate of thickness W depends linearly on the square of the edge length b^2, the Al layer thickness d, and the inverse square of the wafer thickness W^2 [72–76]. Figure 3.3 shows the measured wafer bow as a function of $b^2\ d\ /\ W^2$. The full triangles represent the measured bow data of all depositions according to Tab. 3.1. We fit the measured bow data with the least square method using a linear regression

$$\left(\frac{\delta}{\mathrm{m}}\right) = 6.6 \times 10^{-4} \left(\frac{b^2 d W^{-2}}{\mathrm{m}}\right), \tag{3.1}$$

which is shown as a solid line in Fig 3.3. Using the root mean square method we determine the standard deviation of the linear fit and the measured data to be 0.47 mm, a value that is similar to the error of the bow measurement. The most promising application of an in-line high-rate evaporation system for contacting silicon solar cells is the deposition of 2 µm-thick Al layers onto the rear side of $\sim$ 150 µm-thick silicon solar cells with edge length 156 mm [11]. This process leads to a wafer bow of (1 ± 0.5) mm and is thus tolerable for the module assembly.

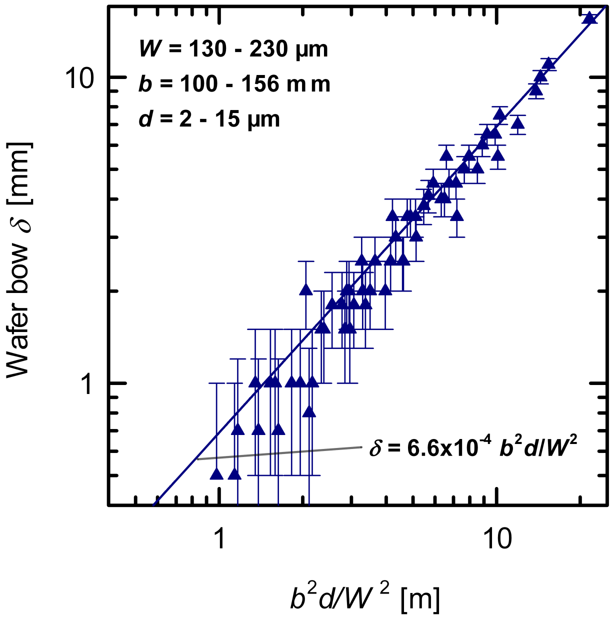

Figure 3.3.: *Measured bow of silicon wafers as a function of the square of the edge length b^2, the Al layer thickness d, and the inverse square of the wafer thickness W^2. The solid line represents a linear fit to the measured data using Eq. (3.1) and equals Eq. (3.2) when assuming a constant temperature difference of 79 K.*

As a first approximation for understanding the measured bow we assume the Al layer of thickness d to consist of various homogeneous sublayers of aluminum of thicknesses d_i, which are deposited at different temperatures T_i. The first sublayer of thickness d_1 is deposited at room temperature T_0 onto the wafer. The deposition leads to an increase in wafer temperature from T_0 to T_1. Afterwards, the second sublayer of thickness d_2 is deposited at T_1, leading to an elevated temperature T_2. We assume each of these sublayers to be free of stress after being deposited. After the deposition of the full layer, the temperature decreases to room temperature $T_0 = 300$ K. In Ref. [72] the elastic deformation of multilayers, which are deposited at various temperatures T_i on a substrate, is derived. The wafer bow

$$\delta = \frac{3}{4}\frac{\alpha_\mathrm{Al} - \alpha_\mathrm{Si}}{E_\mathrm{Si}/E_\mathrm{Al}}\frac{b^2}{W^2}\sum_{i=1}^{n} d_i(T_{i-1} - T_0) \tag{3.2}$$

depends on the edge length b, on the wafer thickness W, the thermal expansion coefficients α_Al and α_Si of Al and Si, respectively, and on Young's Moduli E_Al and E_Si of Al and Si, respectively. We use the coefficients of thermal expansion [77–79] and Young's Moduli [80, 81] of aluminum and silicon given in the literature. Table 3.2 summarizes the parameters of the CTEs and of Young's Moduli.

TABLE 3.2.
COEFFICIENTS OF THERMAL EXPANSION α AT ROOM TEMPERATURE AND YOUNG'S MODULI E OF ALUMINUM AND SILICON TAKEN FROM REFS. [77–81].

Material	Coeffcient of thermal expansion α [$10^{-6}\mathrm{K}^{-1}$]	Young's Modulus E [GPa]
Aluminum	23	70
Silicon	2.6	129.5

Figure 3.4 shows the wafer bow as a function of $b^2\ d\ /\ W^2$ calculated with Eq.(3.2) and with the simulated temperatures T_i at layer thickness $d^* = \sum_{j=1}^{i} d_\mathrm{j}$. The open triangles represent the wafer bow of the upstream edge of the wafer. The open circles represent the wafer bow, which is calculated with the higher temperatures T_i at the downstream edge of the wafer. The solid line represents the linear fit to the measured bow data (see Fig. 3.3). The temperatures from the upstream and downstream edges of the wafer represent upper and lower limits of the wafer temperature and thus also upper and lower limits of the wafer bow. We observe a notable difference between the theoretical and experimental data, where the elastic theory significantly overestimates the bow. This suggest that the bow can not be explained by the elastic theory.

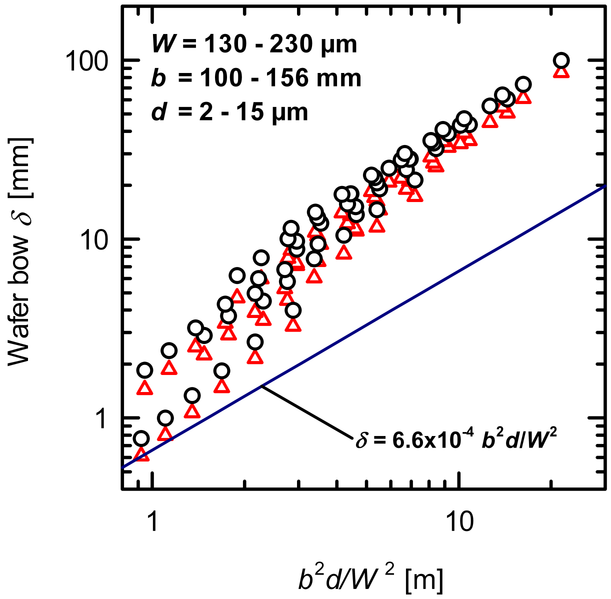

Figure 3.4.: *Bow of silicon wafers as a function of the square of the edge length* b^2*, the Al layer thickness* d*, and the inverse square of the wafer thickness* W^2*. The solid line represents a linear fit to the measured data using Eq. (3.1) and equals Eq. (3.2) when assuming a constant temperature difference of 79 K. The open symbols represent the calculated wafer bow taking into account the simulated peak temperatures of upstream (squares) and of downstream edge (circles) of the wafer.*

Huster investigated the wafer bow after applying screen-printed contacts and found that, similar to our investigations, the elastic theory overestimates the measured wafer bow by a factor 50 [66]. He explained the smaller bending with plastic deformation in the screen-printed Al paste. According to the elasto-plastic theory the wafer starts bending fully elastically upon the first decrease in temperature from the stress-free deposition temperature until the tensile stress in the Al layer reaches the yield stress. Once this stress limit is reached the plastic deformation starts [82]. As the temperature decreases down to room temperature, the plastic deformation results in no further bow as the Al layer cannot build up stresses above the yield stress. Thus, the bow formation does not depend on the process temperature but only on the stress limit of the aluminum paste.

Surprisingly, Eq. (3.2) becomes Eq. (3.1) when $T_{\text{i-1}}$ - $T_0 = 79$ K. This indicates that, similar to the screen-printed contacts, a plastic deformation takes place in the Al layer and that the stress limit is reached after the first 79 K in temperature decrease. In order to measure the plastic deformation we perform thermal cycling tests. Figure 3.5 shows the wafer bow of a 190 µm-thick wafer with edge length 125 mm and an Al layer thickness of 5 µm measured by DIC as a function of temperature during a thermal cycling test.

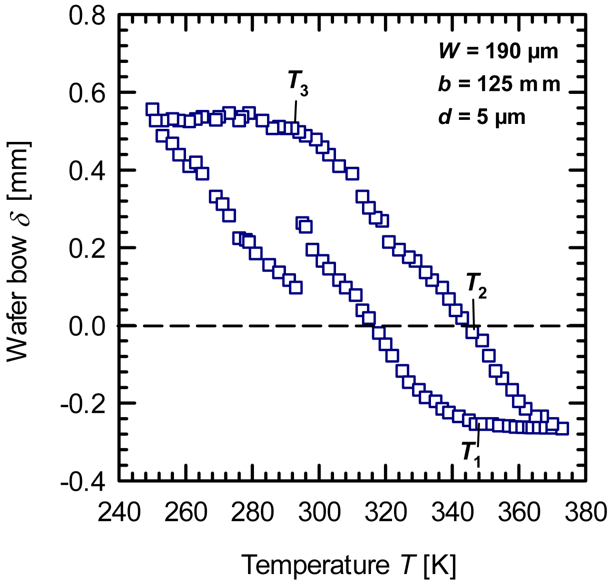

Figure 3.5.: *Wafer bow δ of a 190 μm-thick Si wafer that features a 5 μm-thick Al layer as a function of the temperature during thermal cycling. The wafer is heated up to 373 K, then cooled down to 253 K, and again heated up to 300 K. The different thermal expansion of the silicon wafer and the aluminum layer build up thermo mechanical stresses that lead to the bending.*

A positive bow δ represents a tensile stress in the Al layer, whereas a negative bow refers to compressive stress in the Al layer. The thermal cycling starts at room temperature and first the wafers are heated up. The different thermal expansion of Al and Si leads to a decrease of wafer bow until the compressive stress in the Al layer reaches the yield stress at the temperature $T_1 \approx 354$ K (see Fig. 3.5). Once this stress limit is reached the plastic deformation starts and does not result in a further bow.

During cooling down the wafer bow equals zero at the temperature $T_2 \approx 345$ K and further increases until the tensile stress in the Al layer reaches the yield stress at the temperature $T_3 \approx 295$ K and plastic deformation starts. The difference T_3 - T_2 gives the temperature difference between the stress-free state and the state where the yield stress is reached. We perform cycling tests for 21 wafers with ratios $b^2 d/W^2$ of 1.4 to 21 and determine the difference of the temperatures T_3 and T_2 in average to be (64 ± 9) K. This value is similar to the value of $\Delta T = 79$ K that we have to use in Eq. (3.2) to reproduce the experiments. Both experiments thus show that the wafer starts bending fully elastically upon the first $\sim$ 70 K in temperature decrease and that a further decrease in temperature results in plastic deformation of the Al layer.

3.4. Chapter summary

In this Chapter a comprehensive study of the wafer bow after in-line high-rate evaporation was presented for the first time. The Al layer thickness d, the wafer thickness W, and the wafer edge length b were varied over a broad range, revealing that the actual bow is lower than what would be expected according to the elastic theory. The lower bow is explained with plastic deformation in the Al layer. Due to the plastic deformation only the first $\sim$ 70 K in temperature decrease result in a bow formation and higher substrate temperatures during deposition are thus not critical with regard to the wafer bow. The most promising application for contacting silicon solar cells is the deposition of 2 µm-thick Al layers onto the rear side of $\sim$ 150 µm-thick silicon solar cells with edge length 156 mm [11]. This process leads to a wafer bow of (1 ± 0.5) mm and is thus tolerable for the module assembly. Due to plastic deformation this bow might further be eliminated by cooling down the wafers by $\sim$ 70 K and subsequent heating to room temperature.

4. Electrical properties of evaporated aluminum contacts

This Chapter deals with the electrical properties of point contacts to p-type silicon wafers and to boron-diffused p^+-type Si layers that are prepared by in-line high-rate evaporation of aluminum. Typically evaporation of aluminum is used for contacting passivated and locally contacted rear sides of silicon solar cells. The electrical properties saturation current density J_0 and contact resistivity ρ_c are the most important characteristics for understanding the impact of the rear side aluminum layer on solar cell efficiency. In this Chapter parameterizations of the saturation current densities J_0 and of contact resistivities ρ_c of aluminum layers to silicon will be presented. Also, the impact of evaporation on the passivation quality of a stack consisting of $\mathrm{Al_2O_3}$ / SiN_x will be investigated and the activation energy of the contact formation will be determined.

4.1. Surface recombination velocity and saturation current density

4.1.1. Contacts to *p*-type base

Figure 4.1 shows the sample structure of a locally contacted silicon wafer. The sample is used for determining both the saturation current density $J_{0,\mathrm{cont}}$ of the contacts and the contact resistivity ρ_c of the Al layers to the silicon substrates. The contacting scheme consists of point contacts with various radii r and period lengths p. The surface recombination velocity (SRV) at the aluminum silicon interface is referred to as S_cont and the SRV of the passivated areas on the front side and between the contacts is referred to as S_pas. The area-averaged effective surface recombination velocity S_eff of a metallized rear side is extracted using the equation

$$\frac{1}{\tau_\mathrm{eff}} = \frac{1}{\tau_\mathrm{bulk}} + \frac{S_\mathrm{pas}}{W} + \frac{S_\mathrm{eff}}{W}, \tag{4.1}$$

where τ_eff is the effective minority charge carrier lifetime, τ_bulk is the bulk lifetime, and W is the wafer thickness [83]. Using Eq. (4.1) S_pas is obtained on passivated symmetric

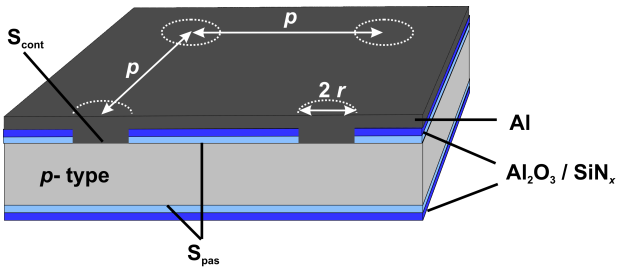

Figure 4.1.: *Schematic representation of a locally contacted silicon wafer. The figure shows the local aluminum contacts with radius r and period length p.*

samples, which do not feature any contact openings. It is assumed that the excess carrier concentration Δn is uniform throughout the base, which is not strictly valid for large surface recombination velocities. Due to the given asymmetry between the front and the rear side of the sample the emitter saturation current density tends to be underestimated up to 10% in the worst-case scenario [83]. Using high-quality float-zone silicon wafers the bulk lifetime τ_{bulk} of the substrate is Auger-limited and we use the parameterization proposed by Kerr et al. [84]. The effective surface recombination velocity

$$S_{\text{eff}} = \left(\frac{R_{\text{s}} - \rho W}{\rho D} + \frac{1}{f \, S_{\text{cont}}} \right)^{-1} + \frac{S_{\text{pas}}}{1 - f} \tag{4.2}$$

is analytically described by a theory introduced by Fischer [85] and depends on the base series resistance R_{s}, the resistivity of the bulk ρ, the wafer thickness W, the minority charge carrier diffusion coefficient D, the metallization area fraction f, and the surface recombination velocities S_{pas} between the contacts and S_{cont} under the contacts.

The base series resistance

$$R_{\text{s}} = p^2 \frac{\rho}{2\pi r} \arctan\left(\frac{2W}{r}\right) + \rho W \left(1 - e^{-W/p}\right) \tag{4.3}$$

of a point contact geometry is given in Ref. [86]. Using Eqs. (4.2) and (4.3) the recombination velocity under the contacts S_{cont} is determined by fitting the measured S_{eff} values using S_{cont} as the only fit parameter. The corresponding saturation current density follows as [83]

$$J_0 = q \, \frac{n_{\text{i}}^2}{N_{\text{A}}} \, S, \tag{4.4}$$

where $q = 1.6 \times 10^{19}$ C is the elementary charge, $n_{\text{i}} = 1 \times 10^{10}$ cm^{-3} is the intrinsic carrier concentration of silicon at 300 K [61], and N_{A} is the doping concentration.

4.1.2. Contacts to boron-diffused p^+-layers

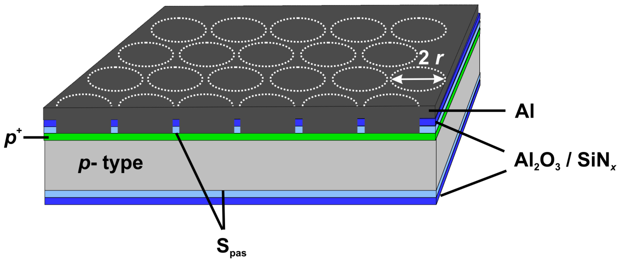

Figure 4.2.: *Schematic structure of a locally contacted wafer that features a boron-diffused* p^+ *layer. The figure shows a cross-section of the local aluminum contacts with radius* r*.*

Figure 4.2 shows the sample structure of a silicon wafer with a locally contacted boron-diffused p^+ layer. Again, S_{pas} denotes the surface recombination velocity of the passivated areas on the front side and between the contacts on the rear side of the wafers. Such samples are used for determining both the saturation current density of the contacted area and of the passivated area and to determine the contact resistivity. The saturation current density $J_{0,\mathrm{pas}}$ is obtained on passivated samples that do not feature any contact openings by plotting the inverse effective lifetime $1/\tau_{\mathrm{eff}}$ versus the excess carrier concentration Δn using the equation [83]

$$\frac{1}{\tau_{\mathrm{eff}}} = \frac{1}{\tau_{\mathrm{bulk}}} + \frac{S_{\mathrm{pas}}}{W} + \frac{J_0\,\Delta n}{q n_{\mathrm{i}}^2 W}. \tag{4.5}$$

The surface recombination velocity S_{pas} of the front side is obtained by lifetime measurements on passivated symmetric wafers that do not feature a boron-diffused layer or contact openings. Using S_{pas} and $J_{0,\mathrm{pas}}$ we extract the saturation current densities $J_{0,\mathrm{cont}}$ from samples that feature laser-contacted boron-diffused layers with an opening fraction f by plotting the inverse effective lifetime $1/\tau_{\mathrm{eff}}$ versus the excess carrier concentration Δn using the equation

$$\frac{1}{\tau_{\mathrm{eff}}} = \frac{1}{\tau_{\mathrm{bulk}}} + \frac{S_{\mathrm{pas}}}{W} + \frac{f\,J_{0,\mathrm{cont}} + (1-f)\,J_{0,\mathrm{pas}}\,\Delta n}{q n_{\mathrm{i}}^2 W}. \tag{4.6}$$

Using area-averaged values implies the passivation layer between the contacts not to be damaged. Thus, the saturation current densities of the contacted area might be overestimated and the calculated $J_{0,\mathrm{cont}}$ data obtained through this method consequently give an upper limit of the saturation current density.

4.2. Silicon sample preparation

4.2.1. Contacts to *p*-type base

For the contact resistivity- and saturation current density measurements asymmetric test structures are fabricated. Both sides are passivated with a stack of plasma-assisted atomic-layer-deposited (ALD) aluminum oxide (Al_2O_3) and plasma-enhanced chemical vapor-deposited (PECVD) SiN_x (see Fig. 4.1). The local contacts are prepared on one side of the samples by local laser ablation of the dielectric stack and subsequent in-line Al deposition. The wafers used in the experiments are (1 0 0)-oriented and 300 µm-thick p-type float-zone silicon wafers of 0.5 Ω cm, 1.5 Ω cm, and 3.8 Ω cm resistivity, respectively. After KOH etching and RCA cleaning the wafers are 270 µm-thick and we deposit on both wafer sides a 10 nm-thick Al_2O_3 and a 90 nm-thick SiN_x layer. The SiN_x layer has a refraction index of $n = 2.05$ at a wavelength of $\lambda = 632$ nm [87]. Afterwards, most of the samples are annealed in a N_2 environment for 15 min at 700 K. For the single sided laser contact openings (LCOs) laser pulses of 8 to 9 picoseconds (ps) at a wavelength of 532 nm are applied to the samples using a Nd:YVO_4 laser [62]. We process various contact schemes with different contact radii r and period lengths p. The variation in the point contact radius r is obtained by a matrix of point contacts. We determine the contact area A of the matrix contacts and the period length p via an optical microscope. The radius of a single point contact is $r = (17 \pm 1)$ µm, whereas the larger contacts feature approximated radii of 80 and 210 µm. Using the *ATON 500* we deposit Al layers of 2 µm, 5 µm, and 10 µm thickness at dynamic deposition rates of 1 µm×m/min, 2.9 µm×m/min, and 5 µm×m/min on the locally opened dielectric layers with the processes shown in Table 4.1.

TABLE 4.1.
DYNAMIC DEPOSITION RATE r_{DYN}, TRAY SPEED v_{TRAY}, AL LAYER THICKNESS d. THE VARIATION IN AL LAYER THICKNESS d IS ACHIEVED BY CHOOSING VARIOUS TRAY SPEEDS v_{TRAY}.

Process	Dynamic deposition rate r_{dyn} [µm×m/min]	Tray speed v_{tray} [m/min]	Aluminum layer thickness d [µm]
1	1	0.5	2
2	2.9	0.7	2
3	5	2.5	2
4	5	1	5
5	5	0.5	10

Subsequently, we deposit a 200 nm-thick silicon dioxide SiO_x layer by means of physical vapor deposition at a low temperature of $T < 400$ K on the aluminum layer using a laboratory batch evaporation system (*BAK EVO* from *Unaxis*). Afterwards we ablate a complementary finger structure of the PVD SiO_x layer, again using the ps laser system, and obtain the finger structure by etching in boiling 37% hydrochloric acid. The finger-structure is used for the measurement of the contact resistivity by the transfer length method. Afterwards the contacts are annealed for various times from 10 seconds to 20 hours at temperatures from 473 K to 623 K. Each lifetime- and contact resistivity measurement is done on three silicon samples and the standard deviation of the three measurements defines the error bars presented in the following figures.

4.2.2. Contacts to boron-diffused p^+-layers

For the contact resistivity- and lifetime measurements we fabricate asymmetric test structures where the passivated p^+ layer is prepared on the rear side of the wafer and the other surface of the sample is well passivated with a stack of Al_2O_3 and SiN_x. For the sample preparation we use single-crystalline, (1 0 0)-oriented and 300 µm-thick p-type float-zone silicon wafers of 200 Ω cm resistivity. After RCA cleaning we deposit on the wafer front side a diffusion barrier consisting of a 100 nm-thick SiN_x layer with a refraction index of $n = 1.9$. After another RCA cleaning the single-sided boron diffusions are done in an industrial-type diffusion furnace from *LPT Europe* [88]. We perform three different diffusion processes with different resulting sheet resistances of 23 Ω/□, 66 Ω/□, and 86 Ω/□, respectively. The diffusions feature an in-situ oxidation [89]. After the diffusions we remove the SiN_x barrier layer and the boron silicate glass in a 40% solution of hydrofluoric acid. After a following RCA cleaning we deposit on both wafer surfaces a 10 nm thick Al_2O_3 layer and a 90 nm thick SiN_x layer with a refraction index of $n = 2.05$, similar to the previous Section. Afterwards, most of the samples are annealed in a N_2 environment for 15 min at 700 K.

Using the ps laser system (see Section 4.2.1) we apply LCOs to the boron-diffused layers. The contacting scheme consists of non-overlapping point contacts with a metallization fraction of $f = 0.7$. The radius of the point contacts is $r = (19 \pm 1)$ µm. Using the *ATON 500* deposition system we deposit Al layers of 2 µm, 5 µm, and 10 µm thickness at dynamic deposition rates of 1 µm×m/min, 2.9 µm×m/min, and 5 µm×m/min onto the locally opened wafer surfaces using the processes shown in Table 4.1. Subsequently we process an Al finger structure as described in Section 4.2.1.

4.3. Measurement techniques

4.3.1. Dynamic infrared lifetime mapping

This Section is based on a description of the infrared lifetime measurement method given in Refs. [90, 91]. Infrared lifetime mapping (ILM) was introduced by Bail et al. in 2000 as a fast, spatially resolved technique for measurements of the excess carrier lifetime in silicon wafers [90]. The silicon wafer is mounted between a black body radiation source and an infrared (IR) camera. The IR-camera is focused on the wafer. The black body emits infrared radiation, which is absorbed and emitted by the wafer and is subsequently detected by the IR-camera. The sample is illuminated with spatially and temporally constant light of photon energy higher than the band-gap energy of silicon. Excess charge carriers are generated and attenuate the IR radiation. Infrared images of the sample are captured under both conditions, with the excitation turned on, and without excitation. The signal difference between these images is caused by the free carrier absorption of the excited charge carriers.

Using a suitable calibration procedure, the infrared signal is related to absolute carrier densities Δn. As the measurement is performed under steady-state conditions, the generation rate of charge carriers G and the recombination rate R are identical. The effective carrier lifetime is given by $\tau_{\text{eff}} = \Delta n/G$. In order to convert Δn into τ_{eff}, the generation rate of charge carriers thus needs to be determined. For this purpose the short circuit current of a calibrated reference solar cell is measured and a reasonable assumption on the front side reflectivity of the silicon sample is made. As the calibration of the infrared emission signal in absolute carrier densities depends critically on the optical properties of the silicon sample, the usage of this method has been restricted to wafers with planar surfaces so far [93, 94].

In order to overcome this restriction, Ramspeck et al. proposed the dynamic infrared lifetime mapping (dynILM) technique that transfers the data analysis into the time domain [91,95,96]. In contrast to the method of Bail, this technique uses the infrared emission of the silicon wafer and not the absorption. The sample is illuminated with spatially constant light of photon energy larger than the band-gap energy of silicon and the free carrier emission of the excited charge carriers is detected using an IR camera. The measurement principle of this technique is sketched in Fig. 4.3. Infrared images of the sample are recorded directly after switching on/off the excitation source, as well as after steady-state conditions have been established in the sample. The carrier lifetime is deduced in an entirely analytical calculation without any further need for a calibration of the signal amplitude [95, 96]. The dynILM technique further enables the measurement of absolute effective lifetimes on metallized silicon samples [91, 97].

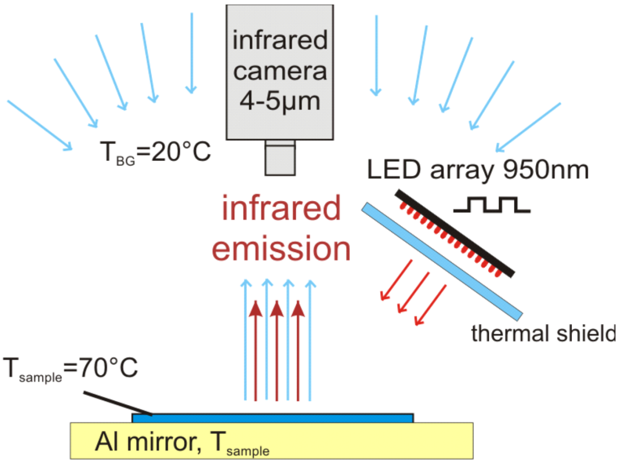

Figure 4.3.: *Schematic of the ILM measurement setup. Charge carriers are generated in the sample by illumination with light, consisting of photons with energies higher than the band-gap energy of silicon. The free carrier emission of these excited charge carriers is detected using an infrared camera. Image taken from Ref. [92].*

4.3.2. Transfer-length-method

In this work the contact resistivity ρ_c of aluminum to silicon is determined using the transfer length method (TLM) [19,98,99]. We thus prepare Al contact fingers of length l and width w that feature various distances d_i from each other. Figure 4.4 shows a schematic of Al fingers contacting a boron-diffused layer. We assume homogeneity of the contact resistivity ρ_c and of the sheet resistance R_{sh} under the Al finger and further assume an exponential decay of the current under the contact. Using the four-point probe method we measure on this structure the total resistance [19]

$$R = R_{sh}\left(\frac{d_i}{l}\right) + 2\left(\frac{l_t}{l}\right) R_{sh} \coth\left(\frac{w}{l_t}\right) + R_{cor} \tag{4.7}$$

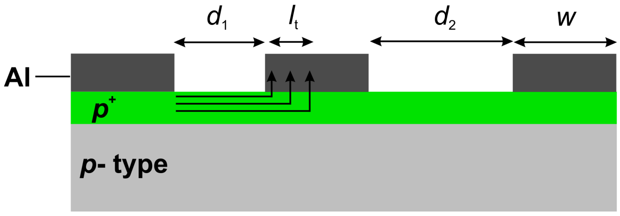

Figure 4.4.: *Cross-section of the sample structure, which is used for the TLM measurement. The Al fingers contact a wafer that features a boron-diffused p^+ layer. The fingers of width w feature various distances d_i from each other.*

between two Al fingers, where R_{sh} is the silicon sheet resistance, l_{t} the transfer length defined by

$$l_{\mathrm{t}} = \sqrt{\frac{\rho_{\mathrm{c}}}{R_{\mathrm{sh}}}}, \tag{4.8}$$

and R_{cor} is a correction term, which is usually neglected in Eq. (4.7) [19, 98, 99]. We calculate R_{cor} by means of a network simulation using the SpiceGUI [100] and find $R_{\mathrm{cor}} = (35 \pm 6)\ \mathrm{m}\Omega$. A more detailed description of the simulation will be presented elsewhere [101]. By plotting the measured total resistance R versus the finger distance d_{i} we obtain the contact resistance

$$R_{\mathrm{c,TLM}} = \left(\frac{l_{\mathrm{t}}}{l}\right) R_{\mathrm{sh}} \coth\left(\frac{w}{l_{\mathrm{t}}}\right) - R_{\mathrm{cor}}. \tag{4.9}$$

The sheet resistance R_{sh} follows by the slope of this plot. Using the measured R_{sh} and Eqs. (4.8) and (4.9) yields the contact resistivity ρ_{c}. An accurate determination of the finger distance d_{i} is essential for the determination of the contact resistivity. We determine d_{i} with a light-microscope with an accuracy of ± 10 µm and take this accuracy into account when determining the error of the contact resistivity. Especially for small contact resistivities below $10^{-3}\ \Omega\ \mathrm{cm}^2$ this leads to large error bars. We use the transfer length method for determining both the contacts to lowly doped p-type Si wafers and to highly doped boron-diffused p^+ layers.

The TLM method was derived for contacts to thin diffused layers assuming only one-dimensional current flow through the semiconductor [98, 99]. When measuring the contact resistivity of aluminum contacts to 300 µm-thick silicon wafers (contacts to p-type base) this one-dimensional current flow might not be given and using the TLM method might thus not be appropriate. We thus use two-dimensional finite-element simulations in order to extract the contact resistivity. We find that the TLM method overestimates the contact resistivity to p-type silicon wafers and determine a correction factor, which depends on the contact resistivity and on the used geometries of the wafer and of the aluminum finger structure. The contact resistivities to p-type silicon presented in this thesis are corrected by this. The simulations also show that the TLM method yields the correct contact resistivity when contacting boron-diffused p^+-type layers. A more detailed description of the simulation of the transfer length method will be presented elsewhere [101].

4.4. Results and discussion

In this Section results of the recombination at point-contacted silicon surfaces and of the contact resistivity are presented. Both, the recombination properties under the contacts and in the passivated area between the contacts are presented. The presented results are obtained with aluminum of a purity of 99.98%. However, using aluminum of purities of 99.999%, which is state of the art in laboratory batch evaporation systems, and of 99.7% did not show a different behavior in investigations of lifetimes and contact resistivities.

4.4.1. Surface recombination velocity and saturation current density

Influence of Al deposition on Al_2O_3 / SiN_x passivation stack

A stack consisting of aluminum oxide and silicon nitride is often used for the passivation of the rear side of locally contacted silicon solar cells [7, 34, 102–104]. Throughout this work, a passivating stack consisting of a 10 nm-thick plasma-assisted atomic-layer-deposited (ALD) aluminum oxide (Al_2O_3) and a 90 nm-thick plasma-enhanced chemical vapor-deposited (PECVD) SiN_x is investigated. The surface passivation of an ALD-Al_2O_3 layer is significantly improved by a post-deposition annealing step [7, 103, 105]. However, if the thermal budget exceeds a certain amount, the passivation quality of an ALD-Al_2O_3 layer decreases [106]. The temperatures during the Al deposition or the deposition of aluminum itself might have an impact on the surface passivation of the Al_2O_3 / SiN_x passivation stacks.

Figure 4.5 shows the measured surface recombination velocity S_{pas} as a function of the deposited aluminum layer thickness d for silicon wafers of 1.5 Ω cm resistivity. Both surfaces of the wafers are passivated with an Al_2O_3 / SiN_x passivation stack. The symbols in Fig. 4.5 (a) represent the S_{pas} values of not-annealed samples whereas Fig. 4.5 (b) shows the SRV of samples that are annealed for 15 minutes at 700 K prior to the Al deposition. The not-annealed samples (see Fig. 4.5 (a)) feature a surface recombination velocity prior to the aluminum depositions of (23 ± 5) cm/s. The SRV decreases with increasing Al layer thickness to (1.9 ± 0.15) cm/s after the deposition of 20 µm-thick Al layers. The deposition of thicker Al layers at a deposition rate of 20 µm×m/min leads to an increase of the SRV of up to (8.2 ± 0.5) cm/s.

In contrast, the annealed samples feature a low surface recombination velocity of (2 ± 0.2) cm/s prior to the Al deposition. The surface recombination velocity increases with increasing Al layer thickness and thus with increasing wafer temperature during the evaporation process. After the deposition of 40 µm at a dynamic deposition rate of 20 µm×m/min the SRV is (8.3 ± 0.7) cm/s. We assume that the observed dependences of the surface recombination velocities on Al layer thickness are caused by the temperatures during the Al depositions. In order to verify this assumption we set the peak temperatures,

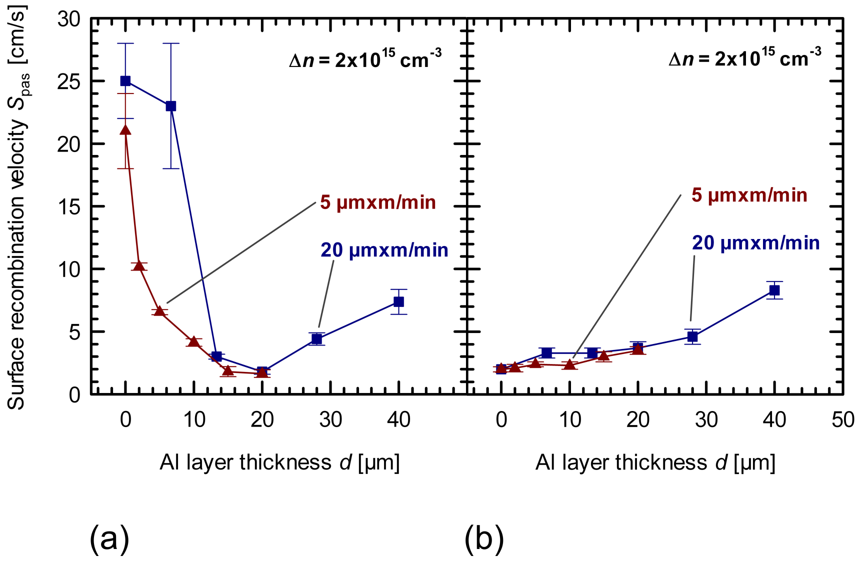

Figure 4.5.: *Measured surface recombination velocity S_{pas} of an Al_2O_3 / SiN_x passivation stack as a function of the deposited aluminum layer thickness d after deposition at dynamic deposition rates of $r_{dyn} = 5$ µm×m/min and of $r_{dyn} = 20$ µm×m/min. (a) SRV of not-annealed and (b) of annealed (15 min at 700 K) silicon wafers of 1.5 Ω cm resistivity.*

which occur during the Al depositions of 2 to 20 µm-thick layers at a rate of 5 µm×m/min, at a hot-plate and anneal the samples for the approximated deposition times. We observe a similar behavior of the surface recombination velocity S_{pas} of the samples that are annealed on a hot-plate and of the samples that feature deposited Al layers and thus conclude that the temperature during Al deposition causes the increase and decrease of SRV shown in Fig. 4.5.

Contacts to *p*-type base

Figure 4.6 shows the measured surface recombination velocity S_{eff} as a function of the opening fraction f for LCOs of radii of 16 µm, 80 µm, and 210 µm on silicon wafers of 1.5 Ω cm resistivity. The symbols represent both, the SRV S_{eff} directly after laser ablation and after the five Al deposition processes according to Table 4.1. The SRVs directly after laser ablation are in excellent agreement to the values after the aluminum depositions within the experimental error. This indicates that neither the surface recombination velocities S_{pas} between the contacts nor S_{cont} under the contacts are influenced by the deposition processes.

In the previous Section we have shown that the depositions of 2 µm, 5 µm, and 10 µm-thick Al layers (see Table 4.1) do not have a detrimental influence on the passivation quality of a stack consisting of a 10 nm thick ALD-Al_2O_3 layer and a 90 nm thick PECVD-

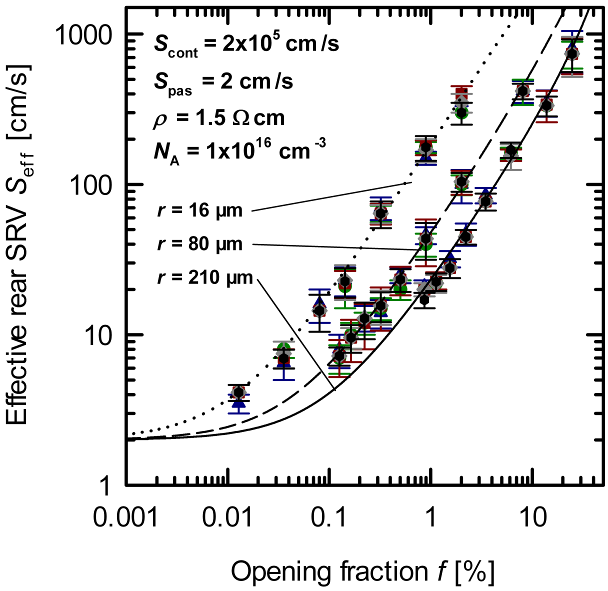

Figure 4.6.: *Measured surface recombination velocity* S_{eff} *as a function of the opening fraction* f *of silicon wafers of 1.5 Ω cm resistivity. The symbols represent both, the SRV* S_{eff} *directly after laser ablation and after the five Al deposition processes according to Table 4.1. Three opening radii of 16 µm, 80 µm, and 210 µm are applied. The SRVs increase with increasing opening fraction. Using Eqs. (4.2) and (4.3) we calculate the SRVs, which are represented by the solid lines.*

SiN$_x$ layer. Using Eqs. (4.2) and (4.3) we calculate the SRVs, which are represented by the lines in Fig. 4.6. We determine the SRV of the contacts for all processes by a least means square fit to be $S_{\mathrm{cont}} = 2{\times}10^5$ cm/s. The lifetimes directly after laser ablation are in accord to the values after the aluminum depositions within the experimental error. In the following we thus only analyze measured lifetimes after the deposition of a 2 µm-thick Al layer at a dynamic deposition rate of 5 µm×m/min.

The SRVs in Fig. 4.6 increase with increasing opening fraction. This is caused by the high recombination velocity under the contacts compared to the SRV in the passivated area between the contacts. The measured SRV values at a fixed opening fraction increase with decreasing opening radius. Müller et al. [97] showed that this is mainly caused by a transport limitation of the minority charge carriers to the contacts at large period lengths. In the following we want to further investigate this limitation by diffusion and thus analyze the silicon wafers of 3.8 Ω cm resistivity, since these wafers feature the highest minority charge carrier diffusion coefficient D in our experimental study.

Figure 4.7 shows the measured surface recombination velocities S_{eff} as a function of the opening fraction f for LCOs of 17 µm radius on silicon wafers of 3.8 Ω cm resistivity. The symbols represent the SRV S_{eff} after the deposition of a 2 µm-thick Al layer at a dynamic

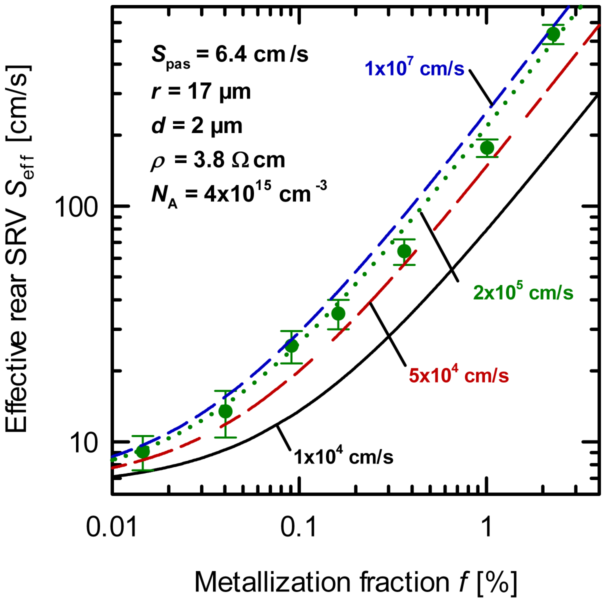

Figure 4.7.: *Measured surface recombination velocity S_{eff} as a function of the metallization fraction f of silicon wafers of 3.8 Ω cm resistivity (symbols). The SRVs increase with increasing opening fraction. Using Eqs. (4.2) and (4.3) we calculate for surface recombination velocities under the contacts of* 10^4 - 10^7 *cm/s the effective rear SRVs, which are represented by the lines.*

deposition rate of 5 µm×m/min. The lines represent the effective surface recombination velocity, which is calculated using Eqs. (4.2) and (4.3) with contact SRVs of $S_{\mathrm{cont}} = 10^4$ - 10^7 cm/s. The velocity of 1×10^7 cm/s is approximately the thermal velocity of the minority charge carriers and thus represents an upper limit of the surface recombination velocity. Using S_{cont} of 2×10^5 cm/s fits the measured SRVs best. However, assuming the thermal velocity as S_{cont} in Eq. (4.2) gives only about 10% higher S_{eff} values and is thus within the error bars of the measurement. An exact determination of S_{cont} is thus not possible.

From Fischer's Equation (4.2) it follows that the effective surface recombination velocity does hardly depend on the contact recombination velocity, when S_{cont} exceeds a certain value. We thus define the diffusion limit $S_{\mathrm{cont,limit}}$ by $S_{\mathrm{eff}}(S_{\mathrm{cont,limit}}) = 0.9\ S_{\mathrm{eff}}(10^7\ \mathrm{cm/s})$. The diffusion limit is almost independent from the base doping density. It is, when applying LCOs with radius 17 µm, about 2×10^5 cm/s and in the case of larger opening radii of 210 µm about 3×10^4 cm/s. By applying smaller contacts larger S_{cont} values can thus be determined more precisely. However, analyzing our experimentally achieved SRVs of single point contacts with 17 µm radius we find that the recombination is limited by the supply of minority charge carriers to the contacts and that a precise determination of S_{cont} is thus not possible. As a consequence we conclude that $S_{\mathrm{cont}} > S_{\mathrm{cont,limit}}$ and we thus present S_{cont} as the arithmetic mean of the diffusion limit $S_{\mathrm{cont,limit}}$ as a lower limit and of the thermal velocity $S_{\mathrm{thermal}} = 10^7$ cm/s as an upper limit. Using Eq. (4.4) we calculate the corresponding $J_{0,\mathrm{cont}}$ values.

Figure 4.8 shows the saturation current density versus the boron doping density of contacted and passivated wafers of 0.5 Ω cm, 1.5 Ω cm, and 3.8 Ω cm resistivity. We determine S_{cont} and thus $J_{0,\mathrm{cont}}$ as the arithmetic mean of the diffusion limit $S_{\mathrm{cont,limit}}$ as a lower limit and of the thermal velocity as an upper limit.

A fit using a power law to the saturation current density under the contacts gives

$$\left(\frac{J_{0,\mathrm{cont}}}{\mathrm{fA/cm^2}}\right) = 9 \times 10^{22} \left(\frac{N_{\mathrm{A}}}{\mathrm{cm^{-3}}}\right)^{-1.004} . \tag{4.10}$$

A decrease of $J_{0,\mathrm{cont}}$ with increasing boron doping density has already been reported in the literature [97, 107, 108]. We determine the saturation current densities $J_{0,\mathrm{pas}}$ of the passivated area on symmetric samples and measure (10.6 ± 2.6) fA/cm^2 for 0.5 Ω cm, (3.2 ± 0.2) fA/cm^2 for 1.5 Ω cm, and (25.6 ± 8.1) fA/cm^2 for 3.8 Ω cm material. These are excellent SRVs that allow for the fabrication of high efficient silicon solar cells [7, 103].

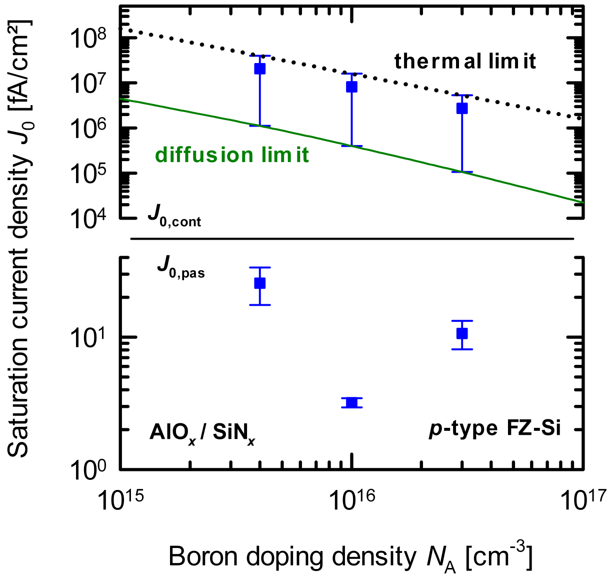

Figure 4.8.: *Measured saturation current densities J_0 of passivated and contacted silicon wafers of resistivities of 0.5 Ω cm (N_A = 3×10^{16} cm^{-3}), 1.5 Ω cm (N_A = 1×10^{16} cm^{-3}), and 3.8 Ω cm (N_A = 4×10^{15} cm^{-3}). The solid line represents the diffusion limit when applying LCOs with radius 17 μm and the dashed line represents the thermal limit.*

Contacts to boron-diffused layers

.

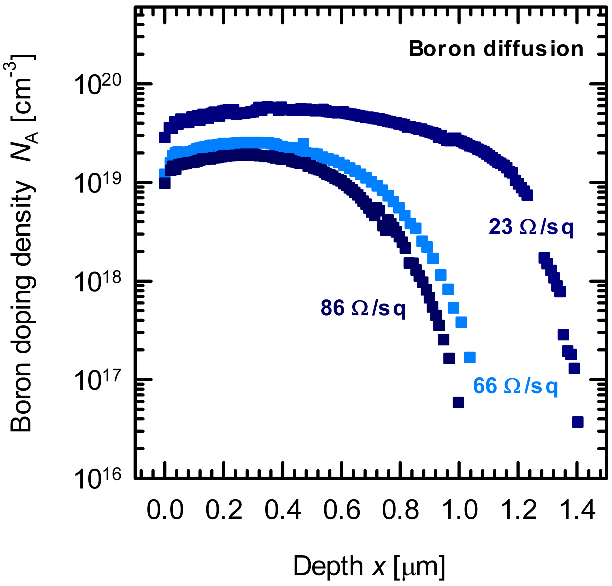

Figure 4.9.: *Doping profile of the boron-diffused layers measured using the ECV profiling technique. The diffusion processes feature an in-situ oxidation [89] and thus low surface doping densities.*

Figure 4.9 shows the doping profiles of the three different boron diffusions examined in this work obtained by the electrochemical capacitance voltage (ECV) profiling technique with the aid of a *WEP CVP21* ECV profiler. We measure the lifetimes on the asymmetric samples shown in Fig. 4.2 directly after laser ablation and after the five Al deposition processes according to Tab. 4.1. Similar to the previous Section we do not observe any dependence of the measured lifetimes on the Al deposition process. In the following we thus only present saturation current densities that are measured after the deposition of a 2 µm-thick Al layer at a dynamic deposition rate of 5 µm×m m/min.

Figure 4.10 shows the measured J_0 values of the passivated and of the contacted boron-doped layers. The J_0 of the contacted layers increases and the J_0 of the passivated layers decreases with increasing sheet resistance $R_{\rm sh}$. This is similar to results obtained on diffused layers that were presented in the literature by Kerr [109] and Cuevas [110]. We fit the measured $J_{0,\rm cont}$ data by

$$\left(\frac{J_{0,\rm cont}}{\rm fA/cm^2}\right) = 118.8\left(\frac{R_{\rm sh}}{\Omega/\square}\right)^{0.452}. \tag{4.11}$$

The increase in $J_{0,\rm cont}$ with increasing sheet resistance $R_{\rm sh}$ results from the field effect passivation associated with the gradient of the doping profile [110]. For a homogeneous

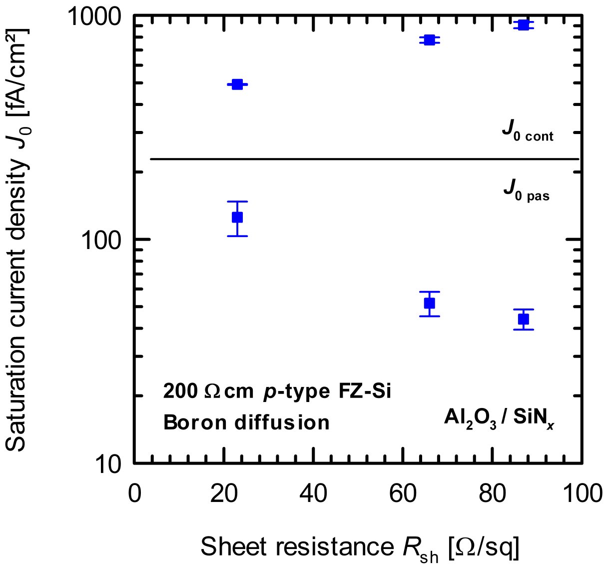

Figure 4.10.: *Measured saturation current densities J_0 of passivated and of contacted p^+ layers of sheet resistances R_{sh} of 23 Ω/□, 66 Ω/□, and 86 Ω/□. The J_0 of the contacted boron-doped layers increase with increasing sheet resistance, whereas the saturation current densities of the passivated boron-doped layers decrease with increasing sheet resistance.*

doping profile, analytical calculations predict $J_{0,\text{cont}}$ to depend on the inverse boron doping density of the diffused boron-layer and thus to increase with increasing sheet resistance [3]. The decrease of the saturation current density $J_{0,\text{pas}}$ of passivated boron-diffused layers with decreasing sheet resistance results from a reduced Auger recombination.

4.4.2. Contact resistivity

We determine the contact resistivity of Al layers to silicon for various aluminum layer thicknesses d and surface doping densities N_A after deposition with the processes shown in Table 4.1. Figure 4.11 shows the measured contact resistivity of 2 µm-thick Al layers to silicon of 1.5 Ω cm resistivity as a function of the dynamic deposition rate r_{dyn}. The blue squares represent the as-deposited contact resistivity and the green triangles represent the contact resistivity after annealing the contacts for 1 minute at 623 K. The as-deposited contact resistivity increases with increasing dynamic deposition rate from (2.5 ± 0.8) mΩ cm² after deposition at r_{dyn} = 1 µm×m/min to (73.7 ± 5.4) mΩ cm², when applying r_{dyn} = 5 µm×m/min.

Heinemeyer et al. showed in Ref. [41] that the wafer temperature during the deposition of 2.5 µm-thick Al layers decreases with increasing dynamic deposition rate from 590 K (r_{dyn} = 1 µm×m/min) to 488 K (r_{dyn} = 5 µm×m/min). We assume the difference in

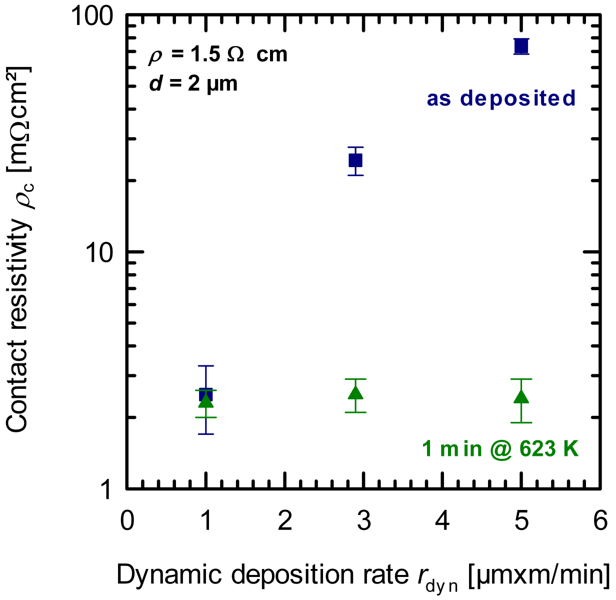

Figure 4.11.: *Measured contact resistivity ρ_c of 2 µm-thick Al layers to boron-doped silicon of 1.5 Ω cm resistivity as a function of the dynamic deposition rate r_{dyn}. The as-deposited contact resistivity (blue squares) increases with increasing deposition rate. Annealing the contacts for 1 minutes at 623 K leads to contact resistivities independent of the dynamic deposition rate.*

as-deposited contact resistivity to be caused by this difference in wafer temperature during the deposition. However, annealing the contacts for 1 minute at 623 K leads to a contact resistivity of (2.4 ± 0.1) mΩ cm^2, independent of the dynamic deposition rate. We thus assume that the different as-deposited contact resistivities are only caused by the different temperatures during the depositions and not by the dynamic deposition rate itself. The static deposition rate in particular (see Fig. 1.6) does not have an impact on the contact resistivity.

In order to investigate the impact of the Al layer thickness on the contact resistivity we compare the processes 3 to 5 from Table 4.1 after deposition on silicon of 1.5 Ω cm resistivity. The as-deposited contact resistivity decreases with increasing aluminum layer thickness from (73.7 ± 5.4) mΩ cm^2 ($d = 2$ µm) to (2.4 ± 1.0) mΩ cm^2 ($d = 10$ µm). Again, we assume the difference in as-deposited contact resistivity to be caused by the difference in peak temperature during the aluminum deposition. The deposition of a 2 µm-thick Al layer onto a 300 µm-thick Si wafer leads to a peak temperature of 425 K whereas the deposition of a 10 µm-thick Al layer leads to a maximum temperature of 759 K (see Fig. 3.2). However, annealing the contacts for 1 minute at 623 K again reduces the contact resistivity to (2.4 ± 0.3) mΩ cm^2 independent on the Al layer thickness.

In the following we want to further investigate the impact of the temperature on the contact resistivity formation. We thus measure the contact resistivity of 2 µm-thick Al layers to silicon of 0.5 and 3.8 Ω cm resistivity as a function of the annealing time for three temperatures of 473 K, 523 K, and 573 K. The contact resistivity decreases with increasing annealing time and reaches a minimum after a certain time. This time taken for the contact resistivity to reach its minimum decreases rapidly with increasing temperature. In the case of silicon of resistivity of 0.5 Ω cm the minimum is reached within 100 seconds when annealing at 573 K and within 10^4 seconds when annealing at 473 K. Using lighter doped silicon with a resistivity of 3.8 Ω cm further increases the times to reach the minimum to 200 seconds (annealing at 573 K) and to 3×10^5 seconds (annealing at 473 K).

We use the Arrhenius equation in order to calculate the activation energy of the contact formation from aluminum to silicon. The activation energy

$$E_\mathrm{A} = -k_\mathrm{b} T ln \left(\frac{K}{A}\right) \tag{4.12}$$

depends on the Boltzmann constant $k_\mathrm{b} = 8.6\times10^{-5}$ eV/K, the temperature T, the reaction rate coefficient K, and the frequency factor A. We assume an exponential decay of the contact resistivity and determine the reaction rate coefficient K as the inverse time constant. Figure 4.12 shows an Arrhenius plot of the reaction rate coefficient K as a function of the inverse temperature $1/T$.

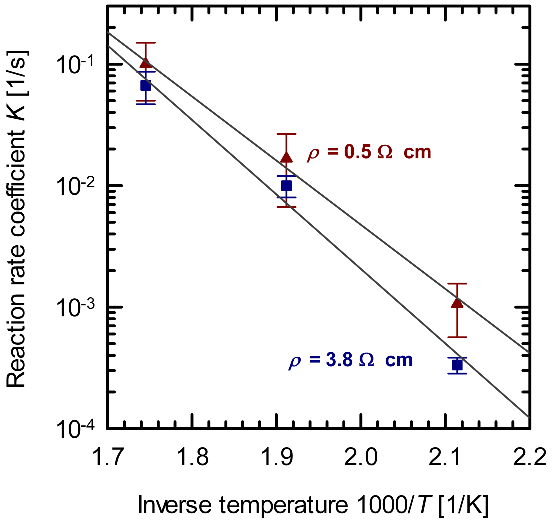

Figure 4.12.: *Reaction rate coefficient K as a function of the inverse temperature in an Arrhenius plot. The calculated activation energy E_A of the contact formation of 2 µm-thick Al layers is determined to be $E_A = (1.06 \pm 0.12)$ eV for silicon of 0.5 Ω cm resistivity and to be $E_A = (1.24 \pm 0.2)$ eV for silicon of 3.8 Ω cm resistivity.*

The fact that the data can be fitted with an Arrhenius plot indicates that the contact formation of aluminum layers to silicon is a thermally activated process. To extract the activation energy of the process, a least squares fit to the measured data in Fig. 4.12 is carried out. We obtain an activation energy of $E_\mathrm{A} = (1.06 \pm 0.12)$ eV for silicon of 0.5 Ω cm resistivity and of $E_\mathrm{A} = (1.24 \pm 0.2)$ eV for silicon of 3.8 Ω cm resistivity.

One might assume that the contact formation is associated with the diffusion of silicon into the Al layer. The fact that the activation energy decreases with increasing doping density might thus be interpreted by an enhanced diffusivity with increasing doping density [111]. In literature the activation energy of the diffusion of silicon into evaporated Al layers was determined to be $E_\mathrm{A} = 0.79$ eV [112]. The silicon samples, especially the doping of the substrates, used by McCaldin are not further specified. He investigated the out diffusion of silicon into Al layers through a contact opening of 80 µm diameter. This might result in a lower activation energy since a larger amount of Al is available for the out diffusing silicon in the case of point contacts compared with a full-area contact.

Figure 4.13 shows the contact resistivity ρ_c for various base doping densities N_A of 4×10^{15} cm^{-3}, 1×10^{16} cm^{-3}, and 3×10^{16} cm^{-3} and surface doping densities of boron-diffused layers of 1×10^{19} cm^{-3}, 1.2×10^{19} cm^{-3}, and 2.8×10^{19} cm^{-3}.

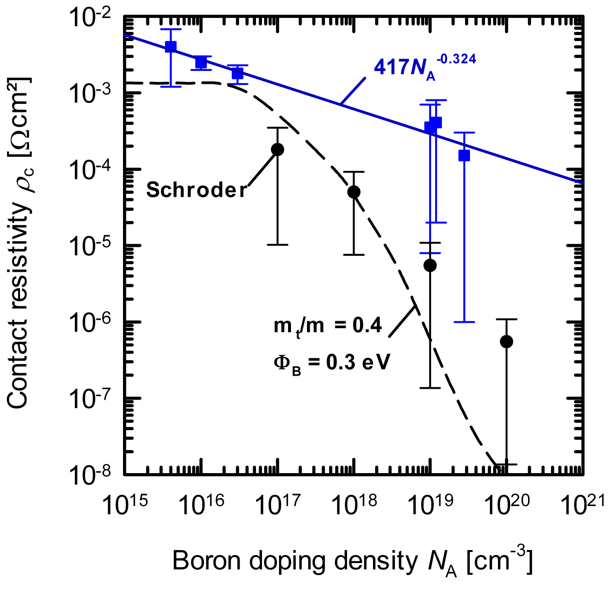

Figure 4.13.: *The squares represent the measured contact resistivity ρ_c of 2 µm-thick Al layers to boron-doped silicon of various surface doping densities N_A. The contact resistivity decreases with increasing doping density. The solid line represents a fit to the measured ρ_c data using an empiric power law. The circles represent measured contact resistivities from Ref. [19] and the dashed line represents data calculated with Eqs. (1.8) to (1.11).*

The squares represent our measured data. The contact resistivity decreases with increasing surface doping density from (4 ± 2.8) mΩ cm^2 to (0.151 ± 0.15) mΩ cm^2. The error bars follow by considering the error of the correction term R_{cor} and of the finger distance d_{i} (see Section 4.3.2), respectively. We fit our measured data by an empiric power law and obtain

$$\left(\frac{\rho_{\text{c}}}{\Omega\,\text{cm}^2}\right) = 427 \left(\frac{N_{\text{A}}}{\text{cm}^3}\right)^{-0.324} . \tag{4.13}$$

The black circles in Fig. 4.13 represent the contact resistivity, which has been presented by Schroder et al. [19]. The values are by 2 orders of magnitude lower than our values. This might indicate that the TLM method is not appropriate for determining very low contact resistivities. However, our measured data agree with the data from Schroder within the error bars. The decrease of the contact resistivity with increasing surface doping density can be explained by the theory of metal-semiconductor contacts. In Section 1.1 it was shown that the barrier height and the barrier width decrease with increasing doping density, which enables tunneling of carriers through the barrier and thus reduces the contact resistivity. Using Eqs. (1.8) to (1.11) we calculate the contact resistivity, which is represented by the dashed line in Fig. 4.13.

4.5. Chapter summary

This Chapter investigated the electrical properties of evaporated aluminum point contacts to silicon. It was found that the recombination at aluminum contacts to B-doped p-type Si wafers are limited by the supply of minority charge carriers. The measured $J_{0,\text{cont}}$ values were fitted by

$$\left(\frac{J_{0,\text{cont}}}{\text{fA/cm}^2}\right) = 9 \times 10^{22} \left(\frac{N_{\text{A}}}{\text{cm}^{-3}}\right)^{-1.004} . \tag{4.14}$$

The $J_{0,\text{cont}}$ values of contacted boron-diffused p^+-type layers were found to increase with increasing sheet resistance R_{sh} according to

$$\left(\frac{J_{0,\text{cont}}}{\text{fA/cm}^2}\right) = 118.8 \left(\frac{R_{\text{sh}}}{\Omega/\Box}\right)^{0.452} . \tag{4.15}$$

The contact resistivity of 2 µm-thick Al layers to silicon was found to decrease with increasing doping density, yielding a fit of the form

$$\left(\frac{\rho_{\text{c}}}{\text{m}\Omega\,\text{cm}^2}\right) = 427 \left(\frac{N_{\text{A}}}{\text{cm}^{-3}}\right)^{-0.324} . \tag{4.16}$$

By studying the contact resistivity as a function of annealing temperature, it was revealed that the contact formation is a thermally activated process with an activation energy of $E_{\mathrm{A}} = (1.06 \pm 0.12)$ eV for silicon of 0.5 Ω cm resistivity and of $E_{\mathrm{A}} = (1.24 \pm 0.2)$ eV for silicon of 3.8 Ω cm resistivity.

5. Formation of aluminum-doped silicon regions

This Chapter presents the formation of aluminum-doped silicon regions by the in-line high-rate evaporation of aluminum. Chapter 2 showed that the in-line high-rate evaporation of aluminum on silicon wafers can lead to substrate temperatures well above 850 K. This temperature represents the lowest temperature where the liquid and the two solid solutions coexist and are in chemical equilibrium. During evaporation at temperatures above 850 K a closed film of an Al-Si liquid forms at the Si surface. During cooling, the Al-Si liquid starts to undercool and an epitaxially grown, aluminum-doped Si layer is formed (see also Section 1.2).

Typically, the rear contact of industrial p-type silicon solar cell is formed in a screen-printing process, where an Al paste is screen-printed on the Si wafer and subsequently fired in a conveyor-belt furnace. The Al-p^+ region is formed during the firing step and serves as the back surface field, reducing the effective surface recombination velocity at the rear side of the cell and thus increasing the solar cell efficiency. In this Chapter the formation of Al-p^+ layers by a single evaporation process without any further temperature treatment is presented. Parts of this Chapter are published in Refs. [113, 114].

5.1. Full-area aluminum-doped regions

5.1.1. Sample preparation

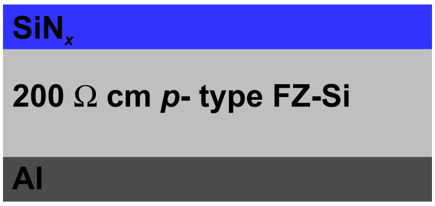

Figure 5.1.: *Schematic structure of a FZ-Si wafer of 200 Ω cm resistivity. The front side of the wafer is passivated with a SiN$_x$ layer. The Al layer is evaporated on the rear side of the wafer.*

We use (1 0 0)-oriented and 270 µm thick p-type float-zone silicon (FZ-Si) wafers of 200 Ωcm resistivity. After KOH etching and RCA cleaning we deposit a 100 nm thick PECVD-SiN$_x$ layer with a refraction index of $n = 2.05$ at a wavelength of $\lambda = 632$ nm on the front side of the wafer [87]. Subsequently, we evaporate Al layers of 13, 20, and 28 µm thickness at a dynamic deposition rate of $r_{\mathrm{dyn}} = 20$ µm×m/min. Figure 5.1 shows a schematic of the sample structure. The process parameters are summarized in Table 5.1. We calculate the wafer temperature during the processes from Table 5.1 using the two-dimensional finite-element simulations from Chapter 2. Figure 5.2 shows the simulated substrate temperature for three deposition processes with layer thicknesses d of 13 µm, 20 µm, and 28 µm. The wafer temperature increases due to the enthalpy of deposition. The deposition of thicker Al layers is thus leading to higher wafer temperatures. The deposition of 20 and of 28 µm-thick Al layers leads to wafer temperatures above the eutectic temperature of the Al-Si system of 850 K. These conditions can lead to the formation of aluminum-doped Al-p^+ region. Please note that phase changes are not considered in the simulation.

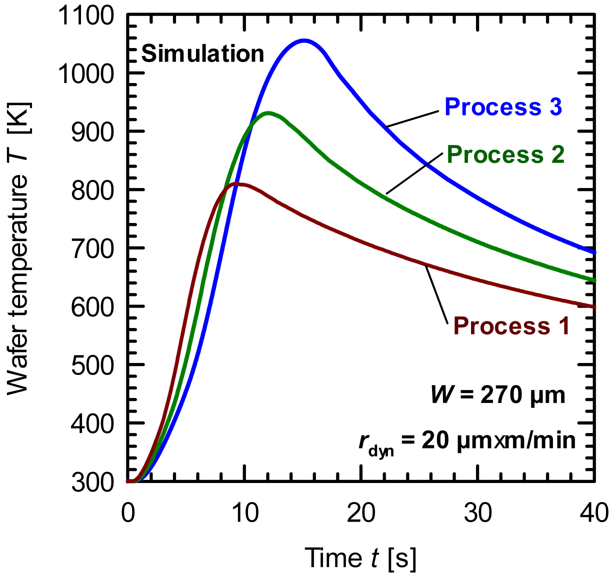

Figure 5.2.: *Substrate temperature T during deposition of Al layers of different thickness d (see Table 5.1) on a planar wafer at a dynamic deposition rate of r_{dyn} = 20 µm×m/min deduced from numerical simulations (see Chapter 2). The Si wafer thickness is fixed at W = 270 µm. The increase in temperature is caused by the deposition of aluminum.*

TABLE 5.1.
TRAY SPEED v_{TRAY} AND AL LAYER THICKNESS d OF THE EVALUATED PROCESSES. THE DYNAMIC DEPOSITION RATE OF ALL PROCESSES IS $r_{\mathrm{DYN}} = 20$ µM×M/MIN. THE VARIATION IN AL LAYER THICKNESS d IS ACHIEVED BY CHOOSING VARIOUS TRAY SPEEDS.

Process	Tray speed v_{tray} [m/min]	Aluminum layer thickness d [µm]
1	1.5	13
2	1	20
3	0.7	28

5.1.2. Results and discussion

Scanning electron microscope study

Figure 5.3 shows cross-sectional SEM images of the full-area evaporated samples of the three deposition processes 1 to 3 from Table 5.1. The images are obtained from an ultra-high resolution *Hitachi S-4800* field emission SEM after the evaporated Al layer has been etched off in a boiling 37% solution of hydrochloric acid (HCl). The Al-doped p^+-region forms during the evaporation process and appears brighter than the high-resistivity bulk of the silicon wafer due to the potential contrast [115]. The process 1 (see Table 5.1) results

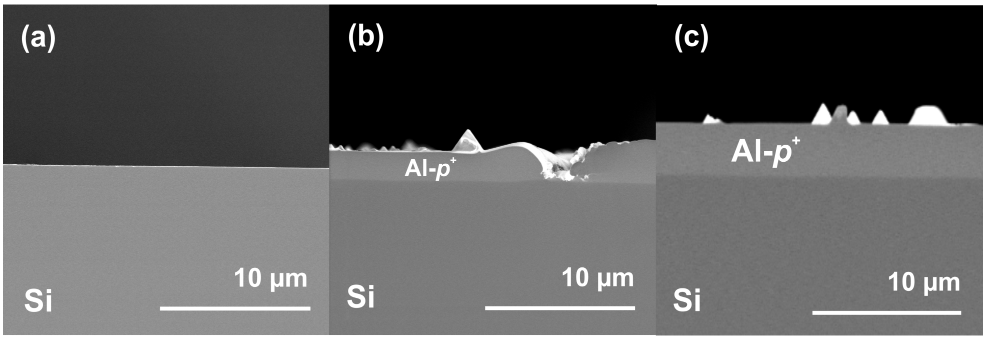

Figure 5.3.: *(a) SEM micrograph of a cross-section of a sample processed with process 1. The process temperature below 850 K is not leading to an Al-p^+ layer. (b) Process 2 results in a higher maximum wafer temperature of $T_{peak} = 938$ K, leading to the formation of a discontinuous Al-p^+ region. The Al-p^+ region is clearly visible as being brighter than the base. (c) Process 3 ($T_{peak} = 1050$ K) results in a completely closed Al-p^+ region. The emitter thickness is (3.5 ± 0.5) µm. Figures 5.3 (b) and (c) show surface structures attributed to aluminum-rich Si-structures on the surface.*

in a peak temperature below 850 K, thus it is not leading to a formation of an Al-p^+ region as shown in Figure 5.3 (a). Process 2 (see Table 5.1) results in a higher maximum wafer temperature of $T_{\text{peak}} = 938$ K, leading to the formation of an Al-p^+ region. However, Figure 5.3 (b) shows a discontinuous aluminum-doped layer. Process 3 (see Table 5.1) with a simulated maximum substrate temperature of $T_{\text{peak}} = 1050$ K results in a completely closed Al-p^+ region as shown in Figure 5.3 (c). From this image we determine the Al-p^+ depth to be (3.5 ± 0.5) µm. The sheet resistance R_{sh} of the Al-p^+ region is determined from four-point-probe measurements to be $R_{\text{sh}} = 80\ \Omega/\square$. SEM investigations on the entire area did not show any substantial non-uniformities of the Al-p^+ thickness and we thus assume a homogeneous distribution of the sheet resistance R_{sh}.

Electrochemical capacitance voltage profiling

Figure 5.4 shows the doping profile of the full-area Al-p^+ region (process 3, see Table 5.1) obtained by the electrochemical capacitance voltage (ECV) profiling technique with the aid of a *WEP CVP21* ECV profiler. The profile is obtained after the evaporated Al layer has been etched off in a boiling 37% solution of hydrochloric acid (HCl). The doping profile of the Al-p^+ region shows a pronounced peak within the first 500 nm close to the surface. In SEM investigations of plan-view samples surface structures are found. These structures are of the same morphology as structures from screen-printed Al-p^+ regions observed in previous studies [116]. Thus, we attribute the measured concentration peak to

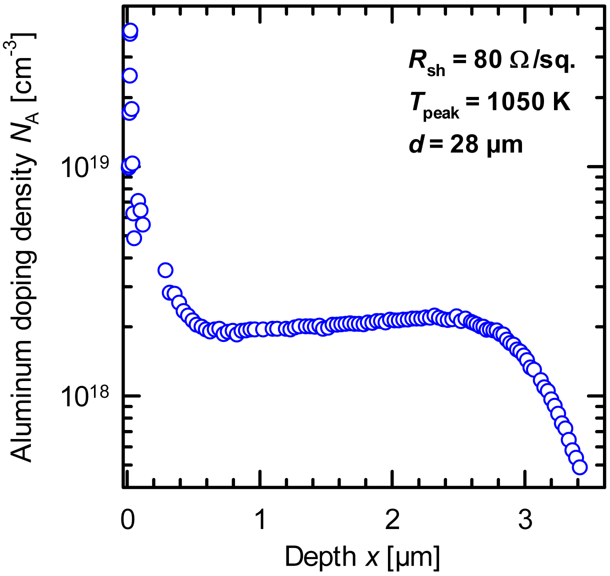

Figure 5.4.: *Doping profile after deposition of 28 µm aluminum at a dynamic deposition rate of 20 µm×m/min measured by ECV profiling. The pronounced concentration peak at the surface is attributed to aluminum-rich surface structures.*

aluminum-rich Si-structures on the surface, which are not removed during the HCl etching.

Saturation current density of evaporated Al-p^+ regions

Figure 5.5 shows the measured inverse effective lifetime $1/\tau_{\mathrm{eff}}$ as a function of the injection density Δn of samples of processes 2 and 3 (see Table 5.1). A fit of Eq. (4.5) to the measured data results in a saturation current density of $J_0 = (1600 \pm 400)$ fA/cm^2 (process 2) and $J_0 = (695 \pm 65)$ fA/cm^2 (process 3). These values are in the same range as published J_0 data of unpassivated screen-printed Al-p^+ regions, where 500 to 2200 fA/cm^2 have been reported [117–120]. Process 1 results in temperatures of 808 K, thus not leading to a formation of an Al-p^+ region. Due to the missing back surface field we measure an effective carrier lifetime τ_{eff} of only (22 ± 2) µs at a carrier concentration of $\Delta n = 8{\times}10^{13}$ cm^{-3}.

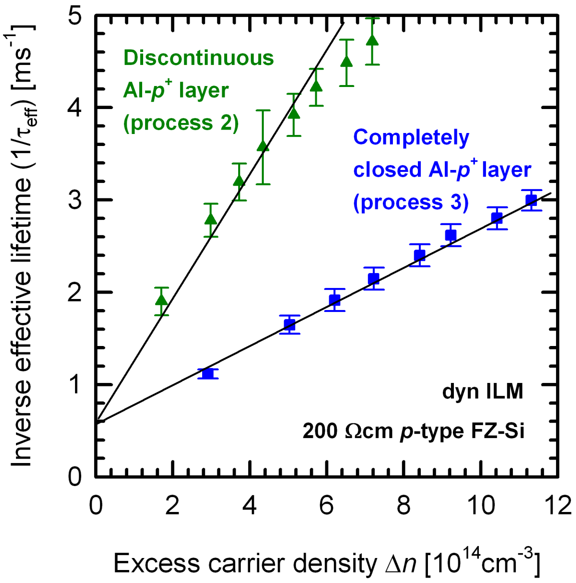

Figure 5.5.: *Measured inverse effective lifetime $1/\tau_{\mathrm{eff}}$ as function of the excess carrier density Δn of a 200 Ω cm FZ p-Si wafer. The Al-p^+ region covers only one side of the wafer, the other surface is well passivated by SiN$_x$.*

5.2. Locally aluminum-doped regions

The electrical and optical properties of a full-area Al-BSF are only moderate and the full-area metal-semiconductor contact often limits the solar cell open-circuit voltage and therefore the energy conversion efficiency. In order to reduce the recombination at the rear side of silicon solar cells, the rear side can be passivated and only contacted by local aluminum contacts. In this Section the formation of local Al-p^+ regions will be presented.

5.2.1. Sample preparation

We use (1 0 0)-oriented and 270 µm thick p-type float-zone silicon (FZ-Si) wafers of 1.5 Ω cm resistivity. After KOH etching and RCA cleaning we deposit on both wafer sides a 10 nm thick ALD-Al_2O_3 layer and a 90 nm thick PECVD-SiN_x layer with a refraction index of $n = 2.05$ at a wavelength of $\lambda = 632$ nm [87]. For the single sided contact openings laser pulses of 8 to 9 picoseconds at a wavelength of 532 nm are applied to the samples using a Nd:YVO_4 laser. The contacting scheme consists of parallel line contacts with a width of $b = 85$ µm and a period length of $p = 2000$ µm. Finally, we evaporate Al layers of 13, 20, and 28 µm thickness on the locally opened wafer side, again using the processes 1 to 3 from Table 5.1.

5.2.2. Results and discussion

Scanning electron microscope study

Figure 5.6 shows cross-sectional SEM images of the samples of the three deposition processes 1 to 3. The images are obtained from an ultra-high resolution *Hitachi S-4800* field emission SEM. Again, process 1 (see Table 5.1) results in a temperature below the eutectic temperature of 850 K, thus no Al-p^+ region is formed (Figure 5.6 (a)). Process 2 results in a wafer temperature of 938 K, leading to the formation of an Al-p^+ region. However, Figure 5.6 (b) shows a discontinuous aluminum-doped region. Process 3, where a peak substrate temperature of $T_{\text{peak}} = 1050$ K is simulated, results in a completely closed Al-p^+ region within the contact openings, as shown in Figure 5.6 (c). From this SEM image we determine the Al-p^+ depth to be (5 ± 3) µm.

At temperatures above the eutectic temperature silicon dissolves into the aluminum layer. The passivation layer acts hereby as a diffusion barrier and the alloying process can only take place in the area of the local openings. This results in the surface morphology shown in Fig. 5.6 (b) and (c). Please note, that the width of the line contacts after the formation of the Al-p^+ region increases from $b = 85$ µm to $b = 120$ µm. A detailed analysis of the contact formation of local screen-printed Al alloyed Si contacts is given in Refs. [121–123].

Please also note that the SEM images 5.6 (b) and (c) show a inhomogeneous aluminum layer. The images are taken directly after the Al depositions. However, images 5.6 (b) shows that the contact area is only covered with a thin Al layer of $\sim$ 1 to 10 µm, whereas the deposited Al layer thickness is 20 µm. Fig. 5.6 (c) shows an accumulation of Al from the deposited 28 µm to a thickness of $\sim$ 40 µm. A macroscopic examination of the samples shows that the rear side of the wafers after the deposition with processes 2 and 3 from Table 5.1 is only partially covered with Al. This might be caused by the input of gravity on the liquid Al layer during deposition.

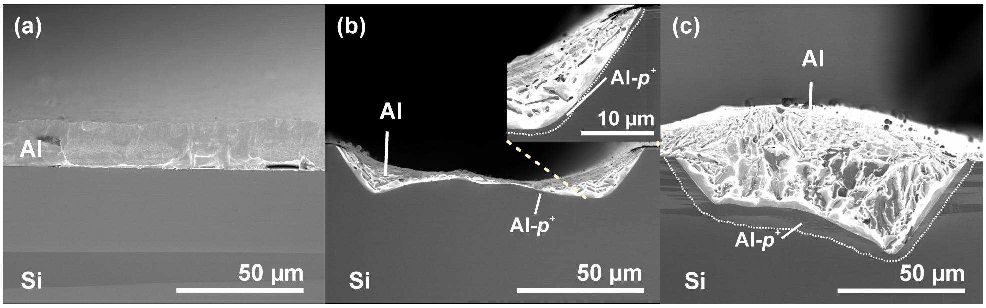

Figure 5.6.: *SEM micrographs of cross-sections of samples processed with processes 1 to 3. The samples feature an Al_2O_3 / SiN_x passivation stack with line openings of a width of 85 µm before Al deposition. The line width increases during the formation of the Al-p^+ layer to 120 µm. (a) SEM micrograph of a sample processed with process 1. The process temperature below 850 K is not leading to a local Al-p^+ region. (b) Process 2 results in a higher maximum wafer temperature of T_{peak} = 938 K, leading to the formation of a discontinuous Al-p^+ region represented by the dotted line. The emitter thickness is (150 ± 150) nm. The Al-p^+ region is clearly visible as brighter contrast. (c) Process 3 (T_{peak} = 1050 K) results in a completely closed Al-p^+ region as represented by the dotted line. The emitter thickness is (5 ± 3) µm.*

Saturation current density of local Al-p^+ regions

Figure 5.7 shows the measured rear SRV S_{eff} as a function of Al layer thickness d. Process 1 (see Table 5.1) is not leading to the formation of an Al-p^+ region. The corresponding effective recombination velocity is S_{eff} = (114 ± 15) cm/s. Processes 2 and 3 lead to the formation of an Al-p^+ region and are thus reducing the effective SRV. Process 2 results in a SRV S_{eff} of (99 ± 10) cm/s and process 3 in a S_{eff} of (50 ± 5) cm/s. Latter value is in the same range as published SRVs of screen-printed local Al-p^+ regions [31]. We use Eqs. (4.2) and (4.3) to determine the recombination velocity S_{cont} at the Al-Si interface by fitting the measured S_{eff} values using S_{cont} as the fit parameter. From the S_{cont} values we determine the corresponding saturation current density J_0 using equation (4.4) to $J_{0,\text{cont}}$ = (11.5 ± 3.5)×10^3 fA/cm^2 for process 1. Processes 2 and 3 are reducing the saturation current density of the contacts to values of (4.8 ± 0.8)×10^3 fA/cm^2 and (1.55 ± 0.15)×10^3 fA/cm^2, respectively. The latter value is higher than the presented saturation current density for a full-area Al-p^+ region that is processed with the same process (see Section 5.1). This can be caused by the different contact formation mechanisms of full-area and local Al-p^+ regions (see Refs. [121–123]). Also, when determining the $J_{0,\text{cont}}$ of the local Al-p^+ regions we assume an opening width of 120 µm, which refers to the one-dimensional opening width in the direction of the Si surface. Hereby, we neglect the actually larger contact area (see Fig. 5.6 (c)) and thus overestimate the saturation current density.

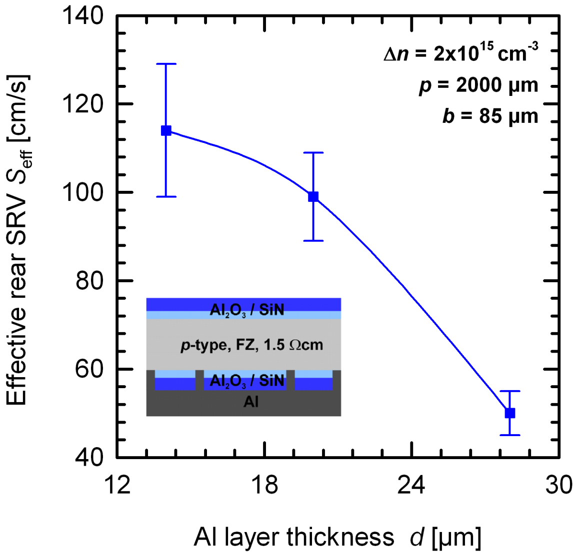

Figure 5.7.: *Measured effective surface recombination velocity S_{eff} as a function of the Al layer thickness d of a 1.5 Ω cm p-type FZ-Si wafer. One side of the wafer is passivated with a stack of Al_2O_3 and SiN_x. The other side is passivated with the same stack and features local laser contact openings of a width of 85 µm and a period length of 2000 µm. The local Al-p^+ region forms at the interface of Al to Si in the area of the contact openings.*

5.3. Chapter summary

This Chapter discussed the formation of aluminum-doped silicon regions by the in-line high-rate evaporation of aluminum due to the high temperatures of up to 1050 K during deposition. For the first time it was demonstrated that the deposition of 28 µm-thick Al layers onto 270 µm-thick planar, unpassivated Si wafers leads to the formation of a (3.5 ± 0.5) µm-thick Al-p^+ region with sheet resistance of R_{sh} = 80 Ω/□. With local contact openings, the same process leads to the formation of a local Al-p^+ region of (5 ± 3) µm thickness when applied on a passivated Si wafer. In addition we showed that the corresponding measured saturation current densities of the contacts are $J_{0,cont}$ = (695 ± 65) fA/cm^2 for the full-area aluminum-doped region and (1.55 ± 0.15)×10^3 fA/cm^2 for the local contacts, which are suitable for fabrication of high-efficiency solar cells.

6. Silicon solar cell device simulation

This Chapter presents the numerical simulation of energy conversion efficiencies of 'passivated emitter and rear cell' (PERC) and of 'passivated emitter rear totally diffused' (PERT) solar cells that feature evaporated rear point contacts. Chapter 4 investigated the electrical properties saturation current density $J_{0,\text{cont}}$ and contact resistivity ρ_c and parameterizations for both parameters were presented. These parameterizations will be used in the present Chapter to simulate the energy conversion efficiencies of PERC and of PERT solar cells. As the baseline case a PERC solar cell that features a screen-printed metallization will be considered [31, 34] and the impact of replacing the screen-printed rear metallization by an evaporated rear metallization will be simulated.

6.1. Baseline case of device simulation

As the baseline case we consider a 'passivated emitter and rear cell' (PERC) processed at ISFH, which features a phosphorous emitter on the front side and screen-printed metallization [31, 34]. This solar cell is simulated in Ref. [34] using the one-dimensional numerical simulation software PC-1D [124] with the parameters shown in Table 6.1. The simulated (and measured [31]) energy conversion efficiency η of the PERC cell featuring a screen-printed metallization of front and rear side is 19.4%.

In order to evaluate the potential of an evaporated rear side metallization, we simulate the efficiency η of solar cells using the front side characteristics of the 19.4% PERC cell as well as the electrical characteristics of evaporated contacts determined in the Chapter 4. We use the recombination, series resistance, and doping profile of the screen-printed front side and consider two solar cell structures with evaporated rear contacts: (i) a PERC solar cell, where the base is locally contacted by laser contact openings and (ii) a PERT solar cell that features a boron-diffused back surface field and laser contact openings (LCO).

Figure 6.1 shows a schematic representation of both solar cell types. Both cells are assumed to be processed on B-doped p-type Czochralski-grown silicon (Cz-Si) and to feature a textured, P-doped n^+-type front emitter and a passivated and locally contacted rear side. We use the values of the screen-printed front side from Ref. [31]. Cz-Si contains boron and oxygen, which forms recombination-active boron-oxygen-complexes under illumination [126, 127]. The minority charge carrier lifetime thus decreases by illumination

Table 6.1.
Parameters used for one-dimensional PC-1D simulations of silicon solar cells. Screen-printed and evaporated refers to the rear side contact formation.

Parameter	Screen-printed PERC cell	Evaporated PERC cell	Evaporated PERT cell
Front reflectance	Measured	Measured	Measured
Emitter contact resistance [Ω cm^2]	0.55	0.55	0.55
Base contact resistance [Ω cm^2]	1	(4.3),(4.13),(6.3)	(4.13),(6.3),(6.5)
Thickness [µm]	180	180	180
Background doping [cm^{-3}]	6×10^{15}	1×10^{15}-1×10^{17}	1×10^{15}-1×10^{17}
Peak doping front diffusion [cm^{-3}]	1×10^{20}	1×10^{20}	1×10^{20}
Rear diffusion [Ω/□]	-	-	23-260
Bulk lifetime [µs]	920	(6.1),(6.2)	(6.1),(6.2)
Front surface recombination [cm/s]	1×10^4	1×10^4	1×10^4
Rear surface recombination [cm/s]	70	(4.2),(4.3)	(6.4), [125]

under typical solar cell operation temperatures. However, the lifetime can be recovered and stabilized by illumination at temperatures in the range of 350 to 500 K [128, 129]. In our simulations we consider both, the degraded lifetime and the stabilized lifetime after illumination and use the parameterizations given in Refs. [127, 130, 131] for a typical oxygen concentration of $(7.5 \pm 0.5)\times10^{17}$ cm^{-3}. The degraded lifetime is

$$\left(\frac{\tau_{\mathrm{n,deg}}}{\mu\mathrm{s}}\right) = 8.7 \times 10^{14} \left(\frac{N_\mathrm{A}}{\mathrm{cm}^{-3}}\right)^{-0.824}, \tag{6.1}$$

while the stabilized lifetime is

$$\left(\frac{\tau_{\mathrm{n,stab}}}{\mu\mathrm{s}}\right) = 1 \times 10^{26} \left(\frac{N_\mathrm{A}}{\mathrm{cm}^{-3}}\right)^{-1.46}. \tag{6.2}$$

As suggested in Ref. [130] we assume the degraded lifetime to increase by a factor 2 due to a standard $POCl_3$ diffusion. We further assume $\tau_\mathrm{p} = 10\ \tau_\mathrm{n}$ and E_t-E_i = 0.15 eV, where E_t is the trap level of Shockley-Read-Hall recombination and E_i is the intrinsic Fermi level.

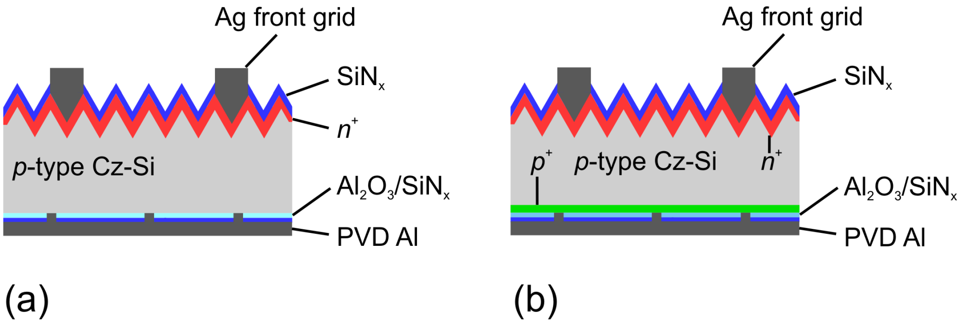

Figure 6.1.: *Schematic representation of (a) PERC and (b) PERT solar cells. Both cells are assumed to be processed on B-doped p-type Czochralski-grown silicon (Cz-Si) and to feature a textured, P-doped n^+-type front emitter and a passivated and locally contacted rear side.*

6.2. Modeling passivated emitter and rear cells

We simulate PERC cells with various base resistivities ρ, contact radii r, and metallization fractions f of the rear side. By varying these parameters both the rear surface recombination velocity S_{eff} and the rear series resistance $R_{\mathrm{s,PERC}}$ change. We calculate the rear SRV as a function of base resistivity, contact radius, and metallization fraction using Fischer's model (see Eqs. (4.2) and (4.3)). We use the fitted dependence of the saturation current densities $J_{0,\mathrm{cont}}$ (see Eq. (4.10)) on the doping density N_{A} and an approximated and constant $J_{0,\mathrm{pas}}$ $= 10$ fA/cm^2 as input parameters. The corresponding series resistance $R_{\mathrm{s,PERC}}$ of the rear side as a function of base resistivity, contact radius, and metallization fraction results from adding the base resistance R_{s} (see Eq. (4.3)) and the area-averaged contact resistance

$$R_{\mathrm{c}} = \sqrt{\frac{\rho\rho_c}{W}}\,\frac{rB_0(-r\sqrt{\rho/\rho_c W})}{-2f\sqrt{-1}B_1(r\sqrt{-\rho/\rho_c W})}, \tag{6.3}$$

which is given in Ref. [98]. B_0 and B_1 are Bessel functions that follow by solving the differential equations when using radially dependent parameters and i is the imaginary unit.

Eq. (6.3) takes into account that the ratio of a point contact that participates in collecting the current decreases with decreasing sheet resistance R_{sh} and also with decreasing contact resistivity ρ_{c} [132]. R_{c} further depends on the wafer thickness W and the opening radius r. Furthermore, we use the parameterization for the contact resistivity ρ_{c} given in Eq. (4.13). The empiric Equation (4.3) deviates less than 8% from the exact numeric solution [85, 133] and Catchpole showed that Eq.(4.3) provides a good approximation for spreading resistance in PERC solar cells [134].

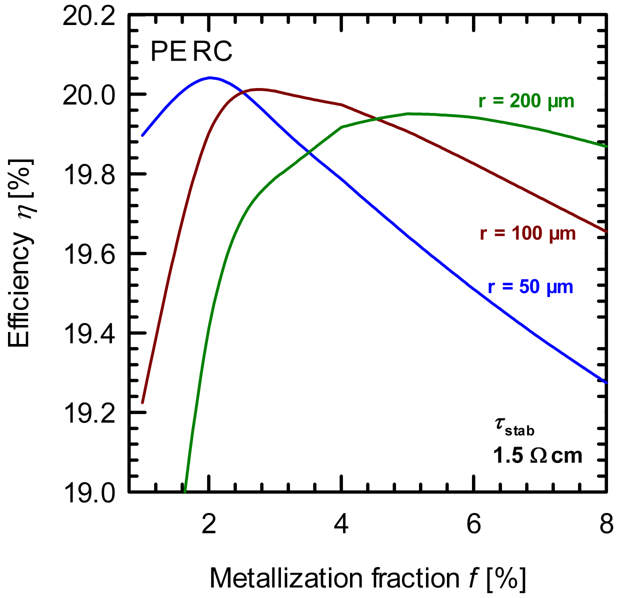

Figure 6.2.: *Energy conversion efficiency η of PERC solar cells with a base resistivity of 1.5 Ω cm obtained by one-dimensional PC-1D simulations. The efficiency is plotted as a function of metallization fraction f for three different contact radii.*

We thus assume that $R_{\text{s,PERC}} = R_{\text{s}} + R_{\text{c}}$ is a reasonable approximation for the base series resistance of PERC solar cells.

Figure 6.2 shows the simulated energy conversion efficiency of a PERC solar cell as a function of the metallization fraction for various contact radii and for a base resistivity of 1.5 Ω cm with stabilized minority carrier lifetime according to Eq. (6.2). The optimum metallization fraction f_{opt}, i. e. the fraction with the highest efficiency η, increases with increasing contact radius r. In addition, the maximum efficiency at a given contact radius is less sensitive to r for larger radii. However, the highest efficiencies are obtained at smaller contact radii. The following simulations were done assuming an opening radius of 100 µm.

The cell efficiency is limited by high series resistance for $f < f_{\text{opt}}$ and by increasing recombination at the rear surface for $f > f_{\text{opt}}$. Figure 6.3 shows the optimum opening fraction depending on base doping density N_{A} for the degraded and stabilized solar cells. The optimum metallization fraction shows a minimum for base doping densities of about 1-5$\times 10^{16}$ cm^{-3} of about 3% (stabilized lifetime) and 4% (degraded lifetime), respectively. A lower bulk lifetime τ_{deg} enables a higher opening fraction since the recombination is dominated by recombination in the p-type base. Thus, increasing recombination losses at the rear by a higher metallization fraction f are overcompensated by the gain in fill factor. As a consequence, the optimum metallization fraction f_{opt} in the case of degraded lifetime is higher than in the case of a stabilized bulk lifetime. Also the increase of f_{opt}

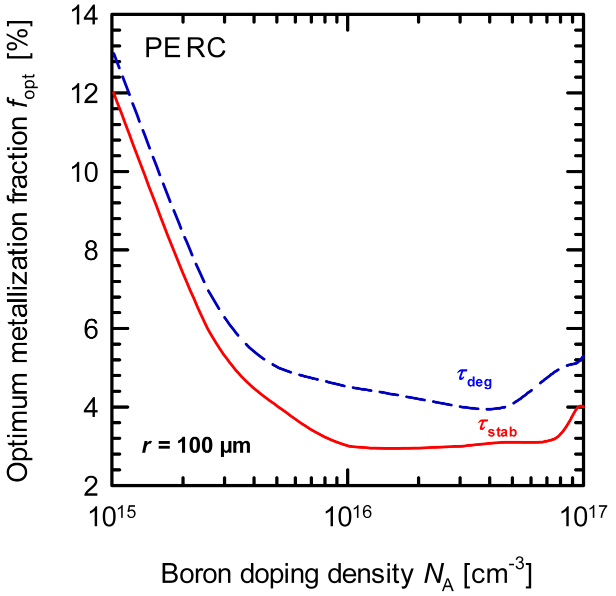

Figure 6.3.: *Optimum metallization fraction f_{opt} of PERC solar cells as a function of the base doping density N_A. The dashed blue line represents a PERC cell with a degraded bulk lifetime τ_{deg} while the solid red line corresponds to a PERC solar cell with a stabilized bulk lifetime τ_{stab}.*

when using higher doped silicon is caused by the lower bulk lifetime associated with higher recombination. The increase for lower doped silicon is caused by the lower conductivity of the base and by the higher contact resistivity.

Figure 6.4 shows the simulated solar cell parameters fill factor FF, open-circuit voltage V_{oc}, short-circuit current density J_{sc}, and efficiency η as a function of base doping density N_{A}. The values are calculated with the optimum metallization fraction (see Fig. 6.3) and with an opening radius of 100 µm. The dashed blue lines represent values which are calculated for a degraded bulk lifetime (see Eq. (6.1)), whereas the solid red lines corresponds to the solar cell parameters after stabilizing the bulk lifetime (see Eq. (6.2)).

The solar cell parameters show qualitatively the same dependence on base doping density for degraded and stabilized bulk lifetimes. The fill factor increases with increasing doping density. This is caused by a reduced total series resistance due to lower base and contact resistances. In addition, the open-circuit voltage V_{oc} increases with increasing doping density, which is caused by the direct influence of the doping density on the dark saturation current density and thus on the open-circuit voltage [135]. The degradation of the bulk lifetime associated with Auger recombination reflects in a decrease of the short-circuit current J_{sc}, which decreases for doping densities larger than 1×10^{16} cm^{-3}. Regarding the solar cell output an optimum base resistivity in the order of 0.5 Ω cm (corresponding to 3×10^{16} cm^{-3}) with an efficiency of 20.6% (stabilized) is found.

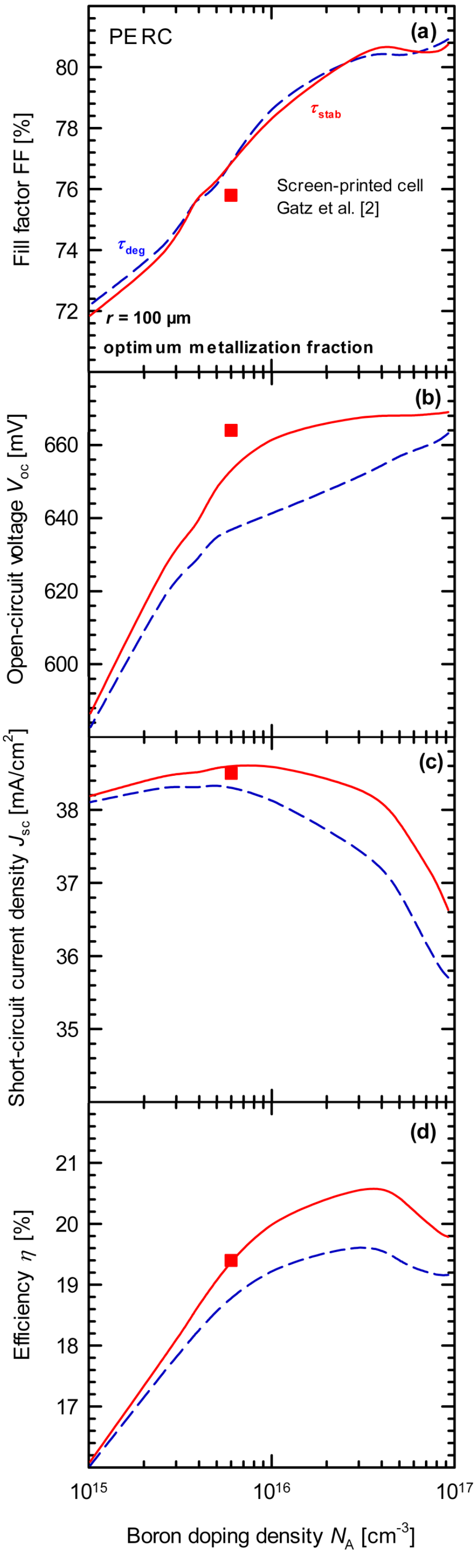

Figure 6.4.: *Simulated solar cell parameters of PERC solar cells as a function of base doping density N_A with degraded lifetimes τ_{deg} (dashed blue lines) and stabilized lifetimes τ_{stab} (solid red lines). The graphs show (a) the fill factor FF, (b) the open-circuit voltage V_{oc}, (c) the short-circuit current density J_{sc}, and (d) the energy conversion efficiency η. The squares represent measured and simulated parameters from the screen-printed solar cell from Refs. [31, 34].*

6.3. Modeling passivated emitter and rear totally diffused cells

We simulate passivated emitter and rear totally diffused (PERT) solar cells with various base resistivities ρ, contact radii r, metallization fractions f, and sheet resistances R_{sh} of the back surface field. By varying these parameters both the recombination at the rear side and the series resistance $R_{\mathrm{s,PERT}}$ change. For the calculation of the rear recombination we determine the saturation current density of the rear side

$$J_{0,\mathrm{rear}} = (1-f)\, J_{0,\mathrm{pas}} + f\, J_{0,\mathrm{cont}} \tag{6.4}$$

by assuming area-averaged values. Note that the numerical simulation program PC-1D requires surface recombination velocities as input parameter. In order to calculate these surface recombination velocities as a function of the metallization fraction f we use a one-dimensional model (EDNA) [125], which models a 1D emitter in silicon. Given a dopant profile as measured by ECV profiling technique (see Fig. 4.9) and a saturation current density $J_{0,\mathrm{rear}}$ (f) of the boron-diffused rear side (see Eq. (6.4)), we calculate the rear surface recombination velocity as a function of the metallization fraction f. This effective SRV is then used as input parameter in the numerical simulations of the energy conversion efficiencies. Fig. 6.5 shows the effective SRV as a function of the metallization fraction

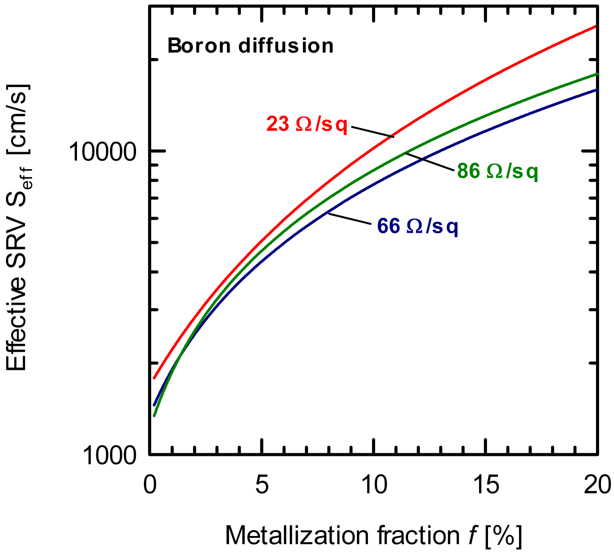

Figure 6.5.: *Effective rear surface recombination velocity $S_{\mathit{eff,rear}}$ as a function of the metallization fraction f for three boron-diffused layers with sheet resistances R_{sh} of 23, 66, and 86 $\Omega/\Box$. The SRV are determined using the measured saturation current densities and using the one-dimensional emitter model EDNA [125].*

for the three boron-diffused layers presented in Section 4.4.1. The surface recombination velocity increases with increasing metallization fraction f from $\sim$ 1500 cm/s for $f = 0\%$ to 1.6×10^4 cm/s (66 $\Omega/\square$), 1.8×10^4 cm/s (86 $\Omega/\square$), and 2.6×10^4 cm/s (23 $\Omega/\square$) for $f = 20\%$, respectively.

In order to calculate the corresponding series resistance $R_{\mathrm{s,PERT}}$ we use the area-averaged contact resistance R_{c} (see Eq. (6.3)) and a model for the series resistance $R_{\mathrm{s}}{}^*$ in the base. This model follows Ref. [136] by assuming lateral flow of the majority charge carriers into the back surface field and then to the point contacts. For the base series resistance follows

$$R_{\mathrm{s}}^* = \rho W + \frac{R_{\mathrm{sh}} p^2}{30} + p^2 \frac{R_{\mathrm{sh}} d_{\mathrm{BSF}}}{2\pi r} \arctan\left(\frac{2 d_{\mathrm{BSF}}}{r}\right), \tag{6.5}$$

where d_{BSF} is the thickness of the boron-diffused layer. The first term in Eq. (6.5) is attributed to the normal current flow through the base into the BSF, the second term corresponds to the resistance in the BSF, and the third term takes into account the spreading resistance under the Al contacts [86, 134].

In the case of a BSF with $R_{\mathrm{sh}} = 66\ \Omega/\square$ and a typical metallization fraction of 2%, the second and third contribution in Equation (6.5) can be neglected and the series resistance is dominated by the current flow through the base. Similar to the previous Section we obtain the total series resistance $R_{\mathrm{s,PERT}}$ by adding Eqs. (6.3) and (6.5). We use the above measured recombination and contact resistivity of boron-diffused layers with sheet resistances R_{sh} of 23 $\Omega/\square$, 66 $\Omega/\square$, and 86 $\Omega/\square$ in our simulations.

The boron-diffused layer under the rear contacts reduces the recombination under the contacts. Hence, it is possible to reduce the distance between the rear contacts compared to the distances of PERC solar cells and to use smaller contact openings [137, 138]. This results in a reduced lateral series resistance and thus an increased fill factor compared to a PERC solar cell. In our simulations of PERT solar cells we thus use the experimentally achieved single point LCOs with a radius of 19 µm.

Figure 6.6 shows the simulated solar cell parameters fill factor FF, open-circuit voltage V_{oc}, short-circuit current density J_{sc}, and efficiency η as a function of base doping N_{A} of PERT solar cells with a BSF with sheet resistance of $R_{\mathrm{sh}} = 66\ \Omega/\square$. The efficiencies are calculated for the optimum metallization fraction f_{opt}. The optimum metallization fraction is about 2% after stabilizing the lifetime and about 3% for a degraded bulk lifetime. The dashed blue lines represent values which are calculated for the degraded bulk lifetime whereas the solid red lines present the solar cell parameters after stabilizing the bulk lifetime. For both bulk lifetimes the fill factor increases with increasing doping density, as expected from the decreasing series resistance in the base. The open-circuit voltage V_{oc} is about 670 mV in the stabilized state for all base doping densities and shows a minimum of $\sim$ 650 mV at 2×10^{16} cm^{-3} for degraded bulk material which increases to 668 mV at 1×10^{15} cm^{-3} and 664 mV at 1×10^{17} cm^{-3}, respectively.

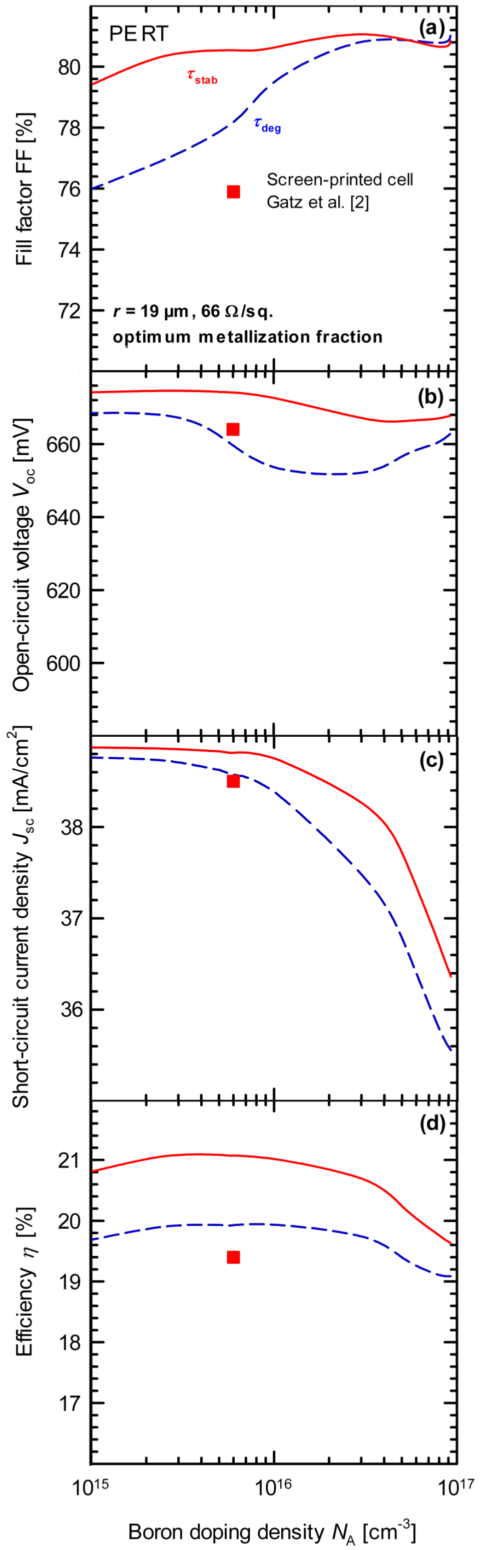

Figure 6.6.: *Simulated solar cell parameters of PERT solar cells as a function of base doping density* N_A *with degraded lifetimes* τ_{deg} *(dashed blue lines) and stabilized lifetimes* τ_{stab} *(solid red lines). The graphs show (a) the fill factor FF, (b) the open-circuit voltage* V_{oc}*, (c) the short-circuit current density* J_{sc}*, and (d) the energy conversion efficiency* η*. The squares represent measured parameters from the screen-printed solar cell from Refs. [31, 34].*

The increase of the V_{oc} in the degraded case for lower doping densities is caused by an increased bulk lifetime whereas the increase for higher doping densities is caused by the direct influence of the doping density on the dark saturation current density.

Similar to PERC cells the degradation of the bulk lifetime is notable regarding the short-circuit current, which decreases with increasing doping density. Regarding the solar cell output an optimum doping density of 4×10^{15} cm^{-3} with an efficiency of 21.1% (stabilized) and 19.9% (degraded) is found. However, the efficiency is not significantly changing for base doping densities from 2×10^{15} to 9×10^{15} cm^{-3} and a PERT solar cell is less sensitive to the base doping than the PERC solar cell structure. Please note that these efficiencies are simulated assuming the current screen-printed front side and that improving the front side would result in higher efficiencies. In the following we want to investigate the influence of the BSF sheet resistance R_{sh} onto the energy conversion efficiency η. In order to estimate cell efficiencies of PERT solar cells that feature back surface fields with higher sheet resistances we extrapolate our measured saturation current densities $J_{0,\mathrm{pas}}$ and $J_{0,\mathrm{cont}}$ (see Fig. 4.10) and contact resistivities ρ_{c} (see Fig. 4.13) and simulate PERT solar cells with BSFs of up to 260 Ω/□. Figure 6.7 shows the simulated energy conversion efficiency of PERT solar cells as a function of BSF sheet resistance R_{sh} with degraded lifetimes τ_{deg} (dashed blue line) and stabilized lifetimes τ_{stab} (solid red line).

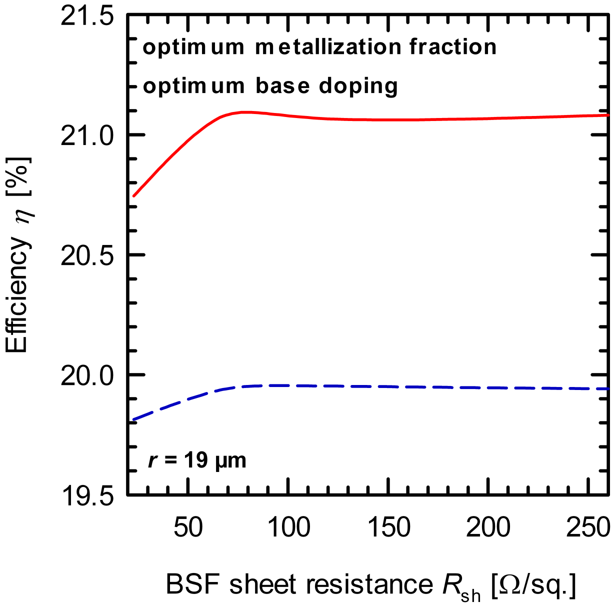

Figure 6.7.: *Simulated solar cell efficiencies of PERT solar cells as a function of sheet resistance R_{sh} with degraded lifetimes τ_{deg} (dashed blue lines) and stabilized lifetimes τ_{stab} (solid red lines). The efficiencies are calculated with the optimum metallization fraction f and optimum base doping density N_A. Both depend on the sheet resistance R_{sh}.*

The efficiencies are calculated for the optimum metallization fraction f_{opt} and base doping density N_{A}. We observe similar cell efficiencies of PERT solar cells with sheet resistances from 60 Ω/□ to 260 Ω/□ with a broad maximum at $R_{\mathrm{sh}} = 70$ Ω/□.

6.4. Loss analysis of PERC and PERT solar cells

In order to identify the efficiency limiting factors we determine the free energy losses of the different transport and recombination paths of the simulated PERC and PERT solar cells [139]. The calculation of the free energy is based on the series resistance and on the recombination current flows, and the quasi-Fermi levels as extracted from the simulation. A detailed description of the analysis is given in Refs. [139, 140]. All losses are determined in power losses per cell area at the maximum power point. Table 6.2 summarizes the power losses of simulated PERC and PERT solar cells with the highest simulated efficiencies.

Table 6.2.
Absolute power losses of the best PERC and PERT cells with stabilized and degraded bulk lifetimes, evaluated at the maximum power point. The losses due to series resistance and due to recombination at the front and rear side and in the bulk are shown.

Cell type	Maximum efficiency [%]	Base doping [cm^{-3}]	Losses at front [%] Ser. res. / Rec.	Losses at rear [%] Ser. res. / Rec.	Losses in bulk [%] Ser. res. / Rec.
PERC (st.)	20.6	4×10^{16}	0.6 / 0.4	0.08 / 0.3	0.2 / 0.4
PERC (dg.)	19.6	3×10^{16}	0.6 / 0.3	0.06 / 0.2	0.1 / 1
PERT (st.)	21.1	4×10^{15}	0.6 / 0.5	0.06 / 0.2	0.08 / 0.1
PERT (dg.)	19.9	4×10^{15}	0.6 / 0.3	0.04 / 0.1	0.07 / 0.8

The power density losses of the simulated PERC and PERT solar cells are in the case of stabilized lifetime dominated by the losses at the front side and in the case of degraded lifetime by losses in the bulk. The contribution of the rear side to the total power losses of the PERC cells is 20.8% when using stabilized bulk material and 13% in the case of degraded p-type Cz-Si. When simulating PERT solar cells, the contribution to the total power losses of the rear side is determined to 29.4% (stabilized) and 10.6% (degraded). Thus, the analysis shows that the energy conversion efficiency of the simulated solar cells is mainly limited by the front side or by the minority charge carrier lifetime in the base and that the evaporated rear contacts only result in minor power losses. In principle, evaporated rear contacts would thus allow higher efficiencies.

6.5. Chapter summary

This Chapter demonstrated the high potential of evaporated rear contacts for PERC and PERT solar cells.

Using the parameterizations derived in Chapter 4, we performed numerical device simulations to determine the optimum base doping density N_A, metallization fraction f, and BSF sheet resistance R_sh for PERC and PERT type solar cells, respectively. We found that a doping density of 4×10^{16} and metallization fraction f of 3% allow for PERC solar cells with energy conversion efficiencies of 20.6%. For PERT solar cells, the optimum base doping density N_A of 4×10^{15}, metallization fraction f of 2%, and BSF sheet resistance R_sh of 66 $\Omega/\square$ lead to 21.1%. In addition, the simulated free energy losses showed that such cells are not limited by the in-line evaporated point contacts on the rear side. Thus evaporated contacts allow even higher efficiencies.

7. Summary

This work presented for the first time a comprehensive study of the in-line high-rate evaporation of aluminum for the contact formation to silicon solar cells.

First, the temperature of silicon wafers during in-line high-rate evaporation of aluminum was investigated. It was shown that the wafer temperature increases with decreasing wafer thickness W, and wafer emissivity ε as well as with increasing aluminum layer thickness d. Depending on the analyzed deposition parameters the wafer temperatures are in a wide range of 497 K to 1050 K. Two-dimensional finite-element simulations reproduce measured peak temperatures with an accuracy of 97%.

This work also studied the wafer bow after in-line high-rate evaporation and showed that the bow depends on the Al layer thickness d, the wafer thickness W and the wafer edge length b. It was found that the elastic theory overestimates the wafer bow of planar Si wafers. By assuming an elastic bending only during the first 79 K in temperature decrease, which is followed by a plastic deformation of the Al layer, the measured bow data could be reproduced with a standard deviation of 0.47 mm. With regard to the assembly of solar cells into a module, we found that the deposition of 2 µm-thick Al layers onto 156 × 156 mm^2 silicon wafers with thickness 150 µm leads to a tolerable wafer bow of (1 ± 0.5) mm. Due to the plastic deformation the bow might be eliminated by cooling down the wafers by 79 K and subsequent heating to room temperature.

In addition, the impact of Al depositions with wafer temperatures of up to 1050 K on the quality of dielectric passivation stacks was analyzed. A passivation stack consisting of 10 nm-thick ALD-Al_2O_3 and 90 nm-thick PECVD-SiN_x still achieved an excellent surface passivation quality, featuring a saturation current densities of $J_{0,\text{pas}}$ below 8 fA/cm^2 on p-type silicon of 1.5 Ω cm resistivity. Parameterizations for the measured saturation currents of contacted p-type Si wafers and of contacted boron-diffused layers were found.

For the first time the formation of aluminum-doped p^+-type silicon regions by the in-line high-rate evaporation of aluminum without any further temperature treatment was presented. Contact saturation current densities of $J_{0,\text{cont}} = (695 \pm 65)$ fA/cm^2 for full-area Al-p^+ regions and of $(1.55 \pm 0.15)\times10^3$ fA/cm^2 for local Al-p^+ regions were determined.

The contact resistivity of 2 µm-thick Al layers to silicon as a function of the surface doping density was parameterized.

The contact formation was found to be a thermally activated process, with an activation energy of $E_\text{A} = (1.06 \pm 0.12)$ eV for B-doped p-type silicon of 0.5 Ω cm resistivity and of

$E_A = (1.24 \pm 0.2)$ eV for silicon of 3.8 Ω cm resistivity.

Finally, the measured electrical properties of the evaporated Al layers were used in numerical simulations and it was shown that the parameters allow for PERC and PERT solar cells with energy conversion efficiencies of 20.6% and 21.1%, respectively. In addition, the simulated free energy losses showed that such cells are not limited by the in-line evaporated point contacts on the rear side.

The use of evaporated rear contacts to high-efficiency silicon solar cells demands for increased process complexity and for alternative bonding technologies, which needs to be further investigated.

However, the results of this work demonstrated the high quality of rear contacts to silicon solar cells that are formed by in-line high-rate evaporation of aluminum and that evaporation is a promising alternative to the screen-printing technology.

A. Analytical verification of two-dimensional temperature simulation

Equation (2.1) has time-varying boundary conditions Eqs. (2.2), (2.3), and (2.18). Such partial differential equations can only be solved analytically in special cases. In the following such special cases are considered and analytical solutions are presented. The temperatures that are calculated with the analytical formula are compared with the temperatures that are calculated using two-dimensional finite-element simulations.

A.1. Temperature increase

First we consider the special case of a linear increase in wafer temperature. In order to simplify Eqs. (2.1), (2.2), (2.3), and (2.18) we assume an in-line deposition process that features a constant static deposition rate $r_\mathrm{s}(x) = r_\mathrm{s}$, i. e. the deposition is independent of the time and of the position in x-direction over the boat (see Fig. 1.5). Besides, the width of the coating area is assumed to be much larger than the wafer edge length. Thus, heat diffusion within the silicon wafer in x-direction does not occur and can be neglected. We further assume that the emissivity of the wafer equals zero and the heat radiation can thus be neglected. As a consequence only the boundary condition according to Eq. (2.2) applies and simplifies to

$$j_\mathrm{dep}(x) = \Delta H_\mathrm{Al}\,\rho_\mathrm{Al}\,r_\mathrm{s}. \tag{A.1}$$

The temperature of the silicon wafer

$$T(t) = \frac{\Delta H_\mathrm{Al}\,\rho_\mathrm{Al}\,r_\mathrm{s}}{C_\mathrm{Si}\,\rho_\mathrm{Si}\,W}\,t + T_0 \tag{A.2}$$

follows by identifying Eq. (A.1) with the left hand term of Eq. (2.1) and by a subsequent integration over time. The heat capacity of the silicon wafer in Eq. (2.1) is assumed to be independent of the temperature. Please note that the wafer thickness W is included in Eq. (A.2), since the analytical solution according to Eq. (A.2) only considers the heat

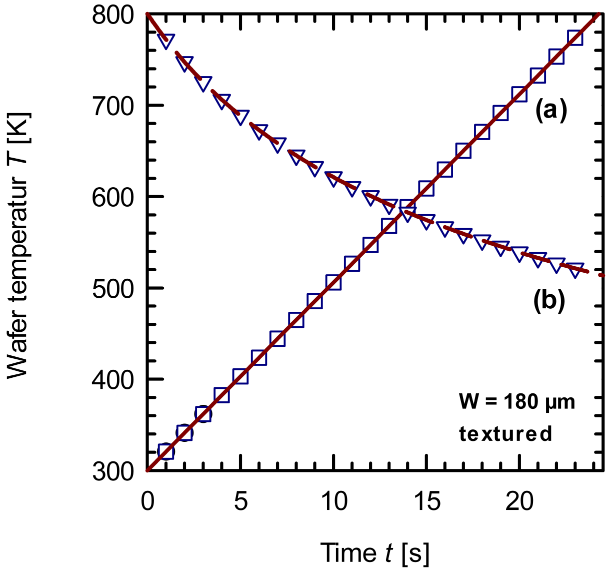

Figure A.1.: *Wafer temperatures calculated by two-dimensional finite-element simulations (symbols) and by the analytical formulas (lines), respectively. (a) The increase in temperature is calculated without any heat radiation from the front side, resulting in a linear increase of the temperature. (b) The temperature decrease of a silicon wafer in vacuum is calculated assuming no heat flows to the wafer.*

capacity of the whole wafer and not of finite-elements, as suggested by Eq. (2.1). T_0 is the temperature of the wafer before deposition. Figure A.1 shows the increase in temperature of a 180 µm-thick silicon wafer calculated with Eq. (A.2) (solid line) and using the two-dimensional finite-element simulation (squares). The agreement of the two is excellent.

A.2. Temperature decrease

In the second case we considered the situation that the wafer of temperature T_0 is cooled down by means of heat radiation. We assume no heat radiation to a wafer (temperature of the chamber equals 0 K) and the reflectivity R of the chamber to be zero. We further assume no aluminum deposition onto the wafer. The temperature dependence of the wafer's emissivity $\varepsilon(T)$ is also neglected. Since heat radiation and heat flow to the wafer are neglected only the boundary condition according to Eq. (2.3) applies and simplifies to

$$j_{\mathrm{rad}}(T) = \varepsilon\, \sigma\, T^4. \tag{A.3}$$

Identifying the left hand term of Eq. (2.1) with Eq. (A.3) gives a differential equation,

$$\dot{T} - a\,T^4 = 0, \tag{A.4}$$

with a = $(\varepsilon\ \sigma)/(C_{\mathrm{Si}}\ \rho_{\mathrm{Si}}\ W)$. Again, W must be taken into account and C_{Si} is assumed to be independent of the temperature T. Solving Eq. (A.4) gives the temperature of the silicon wafer

$$T = \left(3a\left(t + \frac{1}{3aT_0^3}\right)\right)^{-\frac{1}{3}}. \tag{A.5}$$

Figure A.1 shows the temperature of a 180 µm-thick silicon wafer during cooling down calculated with Eq. (A.5) (dashed line) and using the two-dimensional finite-element simulation (triangles). Again, the agreement between the analytical solution and the finite-element simulation is excellent. In conclusion, we have shown that the temperatures which are calculated by two-dimensional finite-element simulations equal the temperatures which are analytically determined.

B. Contacts to n^+-type silicon

B.1. Sample preparation

For the contact resistivity- and lifetime measurements we fabricate asymmetric test structures where the passivated n^+ layer is prepared on the rear side of the wafer while the front side is well passivated with a SiN_x layer. For the sample preparation we use single-crystalline, (1 0 0)-oriented and 300 µm-thick p-type float-zone silicon wafers of 200 Ω cm resistivity. After RCA cleaning we deposit on the wafer front side a diffusion barrier consisting of a 100 nm-thick SiN_x layer with a refraction index of $n = 1.9$. After another RCA cleaning the single-sided phosphorous diffusions are done in an industrial-type diffusion furnace from *LPT Europe* [88]. We perform 2 different diffusion processes with different resulting sheet resistances of 40 Ω/□ and 100 Ω/□, respectively. After the diffusions we remove the SiN_x barrier layer and the phosphorous glass in a 40% solution of hydrofluoric acid. After a following RCA cleaning we deposit on both wafer sides a 10 nm-thick SiN_x layer with a refraction index of 2.4 and a 90 nm-thick SiN_x layer with a refraction

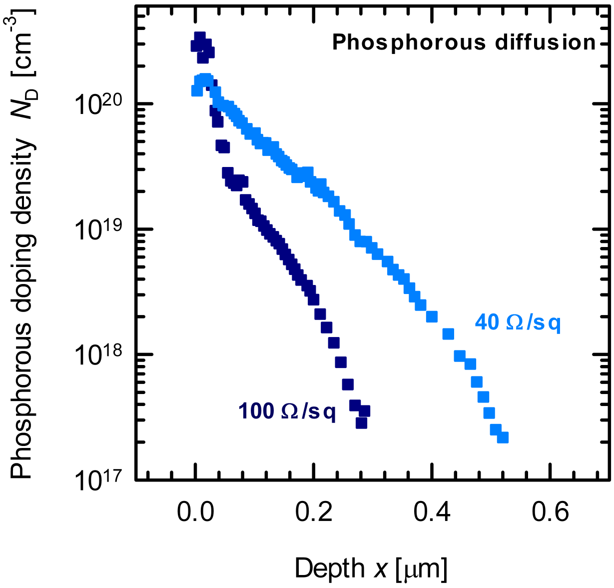

Figure B.1.: *Doping profile of the phosphorous-diffused layers measured using the ECV profiling technique.*

index of $n = 2.05$. Using the ps laser system we apply LCOs to the phosphorous-diffused layers. The contacting scheme consists of non-overlapping point contacts with a metallization fraction of $f = 0.7$. The radius of the point contacts is $r = (20 \pm 1)$ µm. Using the *ATON 500* deposition system we deposit 2 µm-thick Al layers at dynamic deposition rates of 5 µm×m/min onto the locally opened dielectrics. We measure the lifetimes of the metallized samples using the dynILM technique [95,97].

Subsequently, we deposit a 200 nm-thick silicon dioxide SiO_x layer by means of physical vapor deposition at a low temperature of $T < 400$ K on the aluminum layer using a laboratory batch evaporation system (*BAK EVO* from *Unaxis*). Afterwards we ablate a complementary finger structure of the PVD SiO_x layer, again using the ps laser system, and obtain the finger structure by etching in boiling 37% hydrochloric acid. The finger-structure is used for the measurement of the contact resistivity by the transfer length method [25,98,99]. Afterwards we sinter the contacts for 1 minute at 623 K. Each lifetime- and contact resistivity measurement is done on three silicon samples and the standard deviation of the three measurements defines the error bars presented in the following figures.

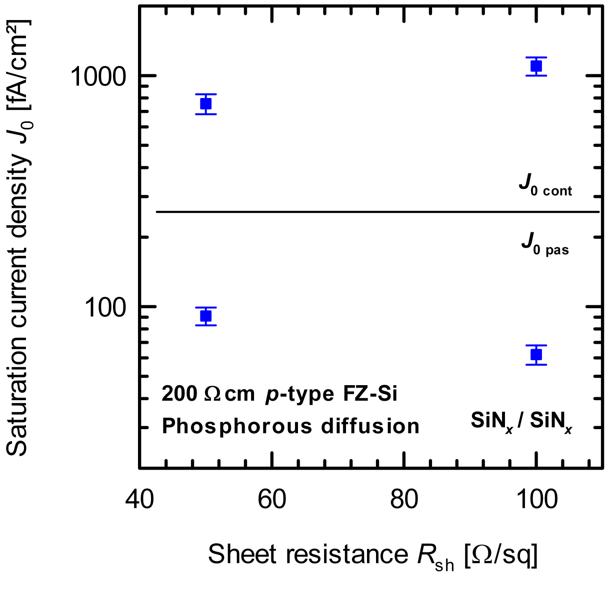

Figure B.2.: *Measured saturation current densities J_0 of passivated and of contacted n^+ layers of sheet resistances R_{sh} of 40 Ω/□ and 100 Ω/□. The J_0 of the contacted phosphorous-doped layers increase with increasing sheet resistance, whereas the saturation current densities of the passivated phosphorous-doped layers decrease with increasing sheet resistance.*

B.2. Results

Figure B.1 shows the doping profiles of the 2 different phosphorous diffusions examined in this work measured using the electrochemical capacitance voltage (ECV) profiling technique (*CVP21* from *WEP*). The diffusions feature surface doping densities N_D of 1.2×10^{20} cm^{-3} (40 Ω/☐) and of 3×10^{20} cm^{-3} (100 Ω/☐), respectively. The depth of the diffused layers are approximately 300 nm (100 Ω/☐) and 500 nm (40 Ω/☐).

Figure B.2 shows the measured J_0 values of the passivated and of the contacted phosphorous-doped layers. The J_0 of the contacted layers increases and the J_0 of the passivated layers decreases with increasing sheet resistance R_{sh}. This is consistent with results obtained on diffused layers presented in the literature [109, 110]. The increase in $J_{0,cont}$ with increasing sheet resistance R_{sh} results from the field effect passivation associated with the gradient of the doping profile [110]. The decrease of the saturation current density $J_{0,pas}$ of passivated phosphorous-diffused layers results from a better surface passivation and thus decreasing recombination for lightly doped diffused layers.

We determine the contact resistivity of Al layers to the two phosphorous-diffused layers using the TLM method. The diffusion with a sheet resistance of 40 Ω/☐ features a surface doping density of 1.3×10^{19} cm^{-3} whereas the diffusion with a sheet resistance of 100 Ω/☐ features a surface doping density of 3×10^{19} cm^{-3}. Similar to Section 4.4.2 we observe a decrease in contact resistivity with increasing doping density from (2.3 ± 0.6) mΩ cm^2 to (1.5 ± 0.4) mΩ cm^2 for the two phosphorous-diffused layers.

References

[1] R. Brendel, N. Harder, J. Schmidt, S. Glunz, R. Preu, S. Reber, and L. Korte, Silicium-Wafersolarzellen: Neue Horizonte, *FVEE - Jahrestagung 2010, Berlin, Germany*, pp. 410–413 (2010).

[2] E. Ralph, Recent advancements in low cost solar cell processing, *Proceedings of the 11th IEEE Photovoltaic Specialists Conference, Scottsdale, AZ, USA*, pp. 315–316 (1975).

[3] M. Godlewski, C. Baraona, and H. Brandhorst, Low-high junction theory applied to solar cells, *Proceedings of the 10th IEEE Photovoltaic Specialists Conference, Palo Alto, CA, USA*, pp. 40–49 (1973).

[4] S. Glunz, New concepts for high-efficiency silicon solar cells, *Sol. Energy Mater. Sol. Cells* **90**, 3276–3284 (2006).

[5] A. Blakers, A. Wang, A. Milne, J. Zhao, and M. Green, 22.8% efficient silicon solar cell, *Appl. Phys. Lett.* **55**, 1363–1365 (1989).

[6] M. Kerr, J. Schmidt, and A. Cuevas, Comparison of the open circuit voltage of simplified PERC cells passivated with PECVD silicon nitride and thermal silicon oxide, *Prog. Photovolt: Res. Appl.* **8**, 529–536 (2000).

[7] J. Schmidt, A. Merkle, R. Brendel, B. Hoex, M. van de Sanden, and W. Kessels, Surface passivation of high-efficiency silicon solar cells by atomic-layer-deposited Al_2O_3, *Prog. Photovolt: Res. Appl.* **16**, 461–466 (2008).

[8] O. Schultz, S. Glunz, and G. Willeke, Multicrystalline silicon solar cells exceeding 20% efficiency, *Prog. Photovolt: Res. Appl.* **12**, 553–558 (2004).

[9] J. Petermann, D. Zielke, J. Schmidt, F. Haase, E. Garralaga, and R. Brendel, 19%-efficient and 43 μm thick crystalline Si solar cell from layer transfer using porous silicon, *Prog. Photovolt: Res. Appl.* **20**, 1–5 (2011).

[10] J. Zhao, A. Wang, M. Green, and F. Ferrazza, 19.8% efficient 'honeycomb' textured multicrystalline and 24.4% monocrystalline silicon solar cells, *Appl. Phys. Lett.* **73**, 1991–1993 (1998).

[11] J. Nekarda, D. Reinwand, A. Grohe, P. Hartmann, R. Preu, R. Trassl, and S. Wiede, Industrial PVD metallization for high efficiency silicon solar cells, *Proceedings of the 34th IEEE Photovoltaic Specialists Conference, Philadelphia, PA, USA*, pp. 892–896 (2009).

[12] C. Mader, J. Müller, S. Gatz, T. Dullweber, and R. Brendel, Rear side point-contacts by in-line thermal evaporation of aluminum, *Proceedings of the 35th IEEE Photovoltaic Specialists Conference, Honolulu, HI, USA*, pp. 1446–1449 (2010).

[13] F. Braun, *Annalen der Physik und Chemie* **153**, 556 (1874).

[14] W. Schottky, Halbleitertheorie der Sperrschicht, *Naturwiss.* **26**, 843 (1938).

[15] F. Mott, *Proc. Cambridge Philos. Soc.* **34** (1938).

[16] E. Rhoderick, *Metal-Semiconductor Contacts*, Clarendon Press (1988).

[17] J. Bardeen, Surface states and rectification at a metal semi-conductor contact, *Phys. Rev.* **71**, 717–727 (1947).

[18] S. Sze, *Physics of Semiconductor Devices*, New York: John Wiley and Sons Inc. (1981).

[19] D. Schroder and D. Meier, Solar cell contact resistance: A review, *IEEE Trans. Electron Devices* **31**, 637–647 (1984).

[20] J. Andrews and M. Lepselter, Reverse current-voltage characteristics of metal-silicide Schottky diodes, *Solid State Electron.* **13**, 1011–1023 (1970).

[21] F. Kröger, G. Diemer, and H. Klasens, Nature of an ohmic metal-semiconductor contact, *Phys. Rev.* **103**, 279–279 (1956).

[22] A. Yu, Electron tunneling and contact resistance metal-silicon contact barriers, *Solid State Electron.* **13**, 239–247 (1970).

[23] F. Padovani and R. Stratton, Field and thermionic-field emission in Schottky barriers, *Solid State Electron.* **9**, 695–707 (1966).

[24] C. Crowell and V. Rideout, Normalized thermionic-field (T-F) emission in metal-semiconductor (Schottky) barriers, *Solid State Electron.* **12**, 89–105 (1969).

[25] D. Schroder, R. Thomas, and J. Swartz, Free carrier absorption in silicon, *IEEE J. Solid-State Circuits* **13**, 180–187 (1978).

[26] J. v. Duppen, *Handbuch für den Siebdruck*, Verlag Der Siebdruck (1986).

[27] P. Hahne, *Innovative Druck- und Metallisierungsverfahren für die Solarzellentechnologie*, PhD thesis, University of Hagen (2000).

[28] P. J. Holmes and R. G. Loasby, *Handbook of Thick Film Technology*, Electrochemical Publications Ltd. (1976).

[29] R. Bock, *Screen-printed aluminum-doped p^+ emitters for the application to n-type silicon solar cells*, PhD thesis, University of Hannover (2011).

[30] J. Murray and A. McAlister, *Bull. Alloy Phase Diagrams* **5**, 74 (1984).

[31] S. Gatz, H. Hannebauer, R. Hesse, F. Werner, A. Schmidt, T. Dullweber, J. Schmidt, K. Bothe, and R. Brendel, 19.4%-efficient large-area fully screen-printed silicon solar cells, *Phys. Status Solidi RRL* **5**, 147–149 (2011).

[32] A. Mohr, P. Engelhart, C. Klenke, S. Wanka, A. Stekolnikov, M. Scherff, R. Seguin, S. Tardon, T. Rudolph, M. Hofmann, F. Stenzel, J. Lee, S. Diez, J. Wendt, W. Brendle, S. Schmidt, J. Müller, P. Wawer, M. Hofmann, P. Saint-Cast, J. Nekarda, D. Erath, J. Rentsch, and R. Preu, 20%-efficient rear side passivated solar cells in pilot series designed for conventional module assembling, *Proceedings of the 26th European Photovoltaic Solar Energy Conference, Hamburg, Germany*, pp. 2150–2153 (2011).

[33] P. Engelhart, D. Manger, B. Klöter, S. Hermann, A Stekolnikov, S. Peters, H. Ploigt, A. Eifler, C. Klenke, A. Mohr, G. Zimmermann, B. Barkenfelt, S. Kuva, J. Wendt, T. Kaden, S. Rupp, D. Rychtarik, M. Fischer, J. Müller, and P. Wawer, Q.antum - q-cells next generation high-power silicon cell & module concept, *Proceedings of the 26th European Photovoltaic Solar Energy Conference, Hamburg, Germany*, pp. 821–826 (2011).

[34] S. Gatz, T. Dullweber, and R. Brendel, Contact resistance of local rear side contacts of screen-printed silicon PERC solar cells with efficiencies up to 19.4%, *Proceedings of the 36th IEEE Photovoltaic Specialists Conference, Seattle, WA, USA*, pp. 3658–3664 (2011).

[35] A. Schneider, *Charakterisierungsverfahren und industriekompatible Herstellungsprozesse für dünne multikristalline Siliziumsolarzellen*, PhD thesis, University of Konstanz (2004).

[36] J. Zhao, A. Wang, and M. Green, 24.5% efficiency PERT silicon solar cells on SEH MCZ substrates and cell performance on other SEH CZ and FZ substrates, *Sol. Energy Mater. Sol. Cells* **66**, 27–36 (2001).

[37] M. Green, K. Emery, Y. Hishikawa, W. Warta, and E. Dunlop, Solar cell efficiency tables (version 38), *Prog. Photovolt: Res. Appl.* **19**, 565–572 (2011).

[38] G. Kienel and K. Röll, *Vakuum- Beschichtung 2*, VDI Verlag (1995).

[39] D. Smith, *Thin-film deposition*, McGraw-Hill, Inc. (1992).

[40] R. Bunshah, *Handbook of deposition technologies for films and coatings*, University of California (1993).

[41] F. Heinemeyer, C. Mader, D. Münster, T. Dullweber, and R. Brendel, Inline high-rate thermal evaporation of aluminum for novel industrial solar cell metallization, *Proceedings of the 5th World Conference on Photovoltaic Energy Conversion, Valencia, Spain*, pp. 2066–2068 (2010).

[42] C. Mader, M. Kessler, U. Eitner, and R. Brendel, Temperature of silicon wafers during in-line high-rate evaporation of aluminum, *Sol. Energy Mater. Sol. Cells* **95**, 3047–3053 (2011).

[43] A. Okhotin, A. Pushkarskii, and V. Gorbachev, *Thermophysical Properties of Semiconductors*, Atom Publ. House (1972).

[44] C. Glassbrenner and G. Slack, Thermal conductivity of silicon and germanium from 3 K to the melting point, *Phys. Rev.* **134**, 1058–1069 (1964).

[45] M. Boccas, T. Vucina, C. Araya, E. Vera, and C. Ahhee, Protected-silver coatings for the 8-m Gemini telescope mirrors, *Thin Solid Films* **502**, 275–280 (2006).

[46] K. Ramanathan and S. Yen, High-temperature emissivities of copper, aluminum, and silver, *J. Opt. Soc. Am.* **67**, 32–38 (1977).

[47] M. Santillan, G. Ares de Parga, and F. Angulo-Brown, Black-body radiation and the maximum entropy production regime, *Eur. J. Phys.* **19**, 361 (1998).

[48] M. Planck, Zur Theorie des Gesetzes der Energieverteilung im Normalspectrum, *Verhandl. Deutsch. phys. Ges.* **11**, 237–245 (1900).

[49] G. Kirchhoff, Ueber das Verhältnis zwischen dem Emissionsvermögen und dem Absorptionsvermögen der Körper für Wärme und Licht, *Annalen der Physik und Chemie* 275–301 (1860).

[50] R. Brendel and D. Scholten, Modeling light trapping and electronic transport of waffle-shaped crystalline thin-film Si solar cells, *Appl. Phys. A* **69**, 201–213 (1999).

[51] R. Brendel, *Sunrays 3.1*, Garching Innovation GmbH (1994).

[52] A. Luque, *Solar Cells and Optics for Photovoltaic Concentration*, Adam Hilger (1989).

[53] R. Smith, *Semiconductors*, Cambridge University Press (1978).

[54] P. Grosse, *Freie Elektronen in Festkörpern*, Springer Verlag (1979).

[55] P. Schumann, W. Keenan, A. Tong, H. Gegenwarth, and C. Schneider, Silicon optical constants in the infrared, *J. Electrochem. Soc.* **118**, 145–148 (1971).

[56] J. Isenberg and W. Warta, Free carrier absorption in heavily doped silicon layers, *Appl. Phys. Lett.* **84**, 2265–2267 (2004).

[57] G. Jellison and H. Burke, The temperature dependence of the refractive index of silicon at elevated temperatures at several laser wavelengths, *J. Appl. Phys.* **60**, 841–843 (1986).

[58] M. Green, Self-consistent optical parameters of intrinsic silicon at 300 K including temperature coefficients, *Sol. Energy Mater. Sol. Cells* **92**, 1305–1310 (2008).

[59] D. Klaassen, A unified mobility model for device simulation-I. Model equations and concentration dependence, *Solid State Electron.* **35**, 953–959 (1992).

[60] D. Klaassen, A unified mobility model for device simulation-II. Temperature dependence of carrier mobility and lifetime, *Solid State Electron.* **35**, 961–967 (1992).

[61] M. Green, Intrinsic concentration, effective densities of states, and effective mass in silicon, *J. Appl. Phys.* **67**, 2944–2954 (1990).

[62] P. Engelhart, N.-P. Harder, R. Grischke, A. Merkle, R. Meyer, and R. Brendel, Laser structuring for back junction silicon solar cells, *Prog. Photovolt: Res. Appl.* **15**, 237–243 (2007).

[63] J. Heinss, C. Mader, A. Merkle, T. Brendemühl, R. Brendel, L. Ehlers, and R. Meyer, Inline high rate deposition of aluminum onto RISE solar cells by electron beam technology, *Proceedings of the 26th European Photovoltaic Solar Energy Conference, Hamburg, Germany*, pp. 2121–2124 (2011).

[64] A. Schneider, C. Gerhards, F. Huster, W. Neu, M. Spiegel, P. Fath, E. Bucher, R. Young, A. Prince, J. Raby, and A. Carroll, Al BSF for thin screenprinted multicrystalline Si solar cells, *Proceedings of the 17th European Photovoltaic Solar Energy Conference, Munich, Germany*, pp.1768–1771 (2001).

[65] A. Schneider, C. Gerhards, P. Fath, E. Bucher, R. Young, J. Raby, and A. Carroll, Bow reducing factors for thin screenprinted mc-Si solar cells with al BSF, *Proceedings of the 29th IEEE Photovoltaic Specialists Conference, New Orleans, LA, USA*, pp. 336–339 (2002).

[66] F. Huster, Aluminium back surface field: bow investigation and elimination, *Proceedings of the 20th European Photovoltaic Solar Energy Conference, Barcelona, Spain*, pp. 635–638 (2005).

[67] M. Hilali, J. Gee, and P. Hacke, Bow in screen-printed back-contact industrial silicon solar cells, *Sol. Energy Mater. Sol. Cells* **91**, 1228–1233 (2007).

[68] M. Köntges, I. Kunze, S. Kajari-Schröder, X. Breitenmoser, and B. Bjoerneklett, The risk of power loss in crystalline silicon based photovoltaic modules due to micro-cracks, *Sol. Energy Mater. Sol. Cells* **95**, 1131–1137 (2011).

[69] U. Eitner, M. Köntges, and R. Brendel, Use of digital image correlation technique to determine thermomechanical deformations in photovoltaic laminates: Measurements and accuracy, *Sol. Energy Mater. Sol. Cells* **94**, 1346–1351 (2010).

[70] J. Orteu, 3-D computer vision in experimental mechanics, *Opt. Lasers Eng.* **47**, 282–291 (2009).

[71] M. Sutton, *Digital image correlation for shape and deformation measurements*, Springer Verlag (2008).

[72] J. Kim, K. Paik, and S. Oh, The multilayer-modified Stoney's formula for laminated polymer composites on a silicon substrate, *J. Appl. Phys.* **86**, 5474 (1999).

[73] C. Hsueh, Modeling of elastic deformation of multilayers due to residual stresses and external bending, *J. Appl. Phys.* **91**, 9652 (2002).

[74] Z. Feng and H. Liu, Generalized formula for curvature radius and layer stresses caused by thermal strain in semiconductor multilayer structures, *J. Appl. Phys.* **54**, 83 (1983).

[75] C. Klein, Comment on 'the multilayer-modified Stoney's formula for laminated polymer composites on a silicon substrate' [J. Appl. Phys. 86, 5474 (1999)], *J. Appl. Phys.* **88**, 5499 (2000).

[76] P. Townsend, D. Barnett, and T. Brunner, Elastic relationships in layered composite media with approximation for the case of thin films on a thick substrate, *J. Appl. Phys.* **62**, 4438 (1987).

[77] Y. Okada and Y. Tokumaru, Precise determination of lattice parameter and thermal expansion coefficient of silicon between 300 and 1500 K, *J. Appl. Phys.* **56**, 314–320 (1984).

[78] R. Roberts, Thermal expansion reference data: silicon 300-850 K, *J. Phys. D: Appl. Phys.* **14**, L163 (1981).

[79] O. Kraft and W. Nix, Measurement of the lattice thermal expansion coefficients of thin metal films on substrates, *J. Appl. Phys.* **83**, 3035–3038 (1998).

[80] J. Greenwood, Silicon in mechanical sensors, *J. Phys. E: Sci. Instrum.* **21**, 1114 (1988).

[81] D. Gerlich and E. Fisher, The high temperature elastic moduli of aluminum, *J. Phys. Chem. Solids* **30**, 1197–1205 (1969).

[82] N. Noda, R. Hetnarski, and Y. Tanigawa, *Thermal stresses*, Taylor & Francis (2002).

[83] D. Kane and R. Swanson, Measurement of the emitter saturation current by a contactless photoconductivity decay method, *Proceedings of the 18th IEEE Photovoltaic Specialists Conference, Las Vegas, NV, USA*, pp. 578–583 (1985).

[84] M. Kerr and A. Cuevas, General parameterization of Auger recombination in crystalline silicon, *J. Appl. Phys.* **91**, 2473–2480 (2002).

[85] B. Fischer, *Loss analysis of crystalline silicon solar cells using photoconductance and quantum efficiency measurements*, PhD thesis, University of Konstanz (2003).

[86] R. Cox and H. Strack, Ohmic contacts for GaAs devices, *Solid State Electron.* **10**, 1213–1218 (1967).

[87] T. Lauinger, J. Schmidt, A. Aberle, and R. Hezel, Record low surface recombination velocities on 1 Ohm cm p-silicon using remote plasma silicon nitride passivation, *Appl. Phys. Lett.* **68**, 1232–1234 (1996).

[88] M. Kessler, T. Ohrdes, B. Wolpensinger, and N.-P. Harder, Charge carrier lifetime degradation in Cz silicon through the formation of a boron-rich layer during BBr_3 diffusion processes, *Semicond. Sci. Technol.* **25**, 055001 (2010).

[89] M. Kessler, D. Münster, T. Neubert, C. Mader, J. Schmidt, and R. Brendel, High-efficiency back-junction silicon solar cell with an in-line evaporated aluminum front grid, *Proceedings of the 37th IEEE Photovoltaic Specialists Conference, Seattle, WA, USA*, pp. 2121–2124 (2011).

[90] M. Bail, J. Kentsch, R. Brendel, and M. Schulz, Lifetime mapping of Si wafers by an infrared camera [for solar cell production], *Proceedings of the 28th IEEE Photovoltaic Specialists Conference, Anchorage, AK, USA*, pp. 99–103 (2000).

[91] K. Ramspeck, *Characterization techniques for silicon solar cells and material using an infrared-camera based approach*, PhD thesis, University of Hannover (2009).

[92] J. Müller, K. Ramspeck, K. Bothe, and R. Brendel, Dynamic infrared lifetime mapping, *Niedersächsisches Photovoltaik Symposium, Hameln, Germany* (2009).

[93] P. Pohl, *Infrared camera-based imaging techniques for solar-grade silicon*, PhD thesis, University of Hannover (2007).

[94] J. Isenberg, *Neue Infrarotmesstechniken für die Photovoltaik*, PhD thesis, University of Konstanz (2003).

[95] K. Ramspeck, S. Reissenweber, J. Schmidt, K. Bothe, and R. Brendel, Dynamic carrier lifetime imaging of silicon wafers using an infrared-camera-based approach, *Appl. Phys. Lett.* **93**, 102104 (2008).

[96] K. Ramspeck, K. Bothe, J. Schmidt, and R. Brendel, Combined dynamic and steady-state infrared camera based carrier lifetime imaging of silicon wafers, *J. Appl. Phys.* **106**, 114506 (2009).

[97] J. Müller, K. Bothe, S. Gatz, F. Haase, C. Mader, and R. Brendel, Recombination at laser-processed local base contacts by dynamic infrared lifetime mapping, *J. Appl. Phys.* **108**, 124513 (2010).

[98] H. Berger, Contact resistance and contact resistivity, *J. Electrochem. Soc.* **119**, 507–514 (1972).

[99] H. Murrmann and D. Widmann, Messung des Uebergangswiderstandes zwischen Metall und Diffusionsschicht in Si-Planarelementen, *Solid State Electron.* **12**, 879–886 (1969).

[100] S. Eidelloth, F. Haase, and R. Brendel, Simulation tool for equivalent circuit modeling of photovoltaic devices, *IEEE J. Photovoltaics,* in press (2012).

[101] S. Eidelloth, C. Mader, and R. Brendel, Simulations for the measurement of specific base contact resistances with the transfer length method, in preparation (2012).

[102] R. Hezel and K. Jäger, Low-temperature surface passivation of silicon for solar cells, *J. Electrochem. Soc.* **136**, 518–523 (1989).

[103] B. Hoex, S. Heil, E. Langereis, M. van de Sanden, and W. Kessels, Ultralow surface recombination of c-Si substrates passivated by plasma-assisted atomic layer deposited Al_2O_3, *Appl. Phys. Lett.* **89**, 042112 (2006).

[104] T. Lauermann, T. Lüder, S. Scholz, B. Raabe, G. Hahn, and B. Terheiden, Enabling dielectric rear side passivation for industrial mass production by developing lean printing-based solar cell processes, *Proceedings of the 35th IEEE Photovoltaic Specialists Conference, Honolulu, HI, USA*, pp. 28–33 (2010).

[105] F. Werner, B. Veith, D. Zielke, L. Kühnemund, C. Tegenkamp, M. Seibt, R. Brendel, and J. Schmidt, Electronic and chemical properties of the c-Si/Al_2O_3 interface, *J. Appl. Phys.* **109**, 113701 (2011).

[106] J. Benick, A. Richter, M. Hermle, and S. Glunz, Thermal stability of the Al_2O_3 passivation on p-type silicon surfaces for solar cell applications, *Phys. Status Solidi RRL* **3**, 233–235 (2009).

[107] M. Schöfthaler, U. Rau, and J. Werner, Direct observation of a scaling effect on effective minority carrier lifetimes, *J. Appl. Phys.* **76**, 4168–4172 (1994).

[108] M. Schöfthaler and R. Brendel, Sensitivity and transient response of microwave reflection measurements, *J. Appl. Phys.* **77**, 3162–3173 (1995).

[109] M. Kerr, J. Schmidt, A. Cuevas, and J. Bultman, Surface recombination velocity of phosphorus-diffused silicon solar cell emitters passivated with plasma enhanced chemical vapor deposited silicon nitride and thermal silicon oxide, *J. Appl. Phys.* **89**, 3821 (2001).

[110] A. Cuevas, P. Basore, G. Giroult-Matlakowski, and C. Dubois, Surface recombination velocity of highly doped n-type silicon, *J. Appl. Phys.* **80**, 3370 (1996).

[111] E. Kirkendall, Diffusion of zinc in alpha brass, *Trans. AIME* **147**, 104–109 (1942).

[112] J. McCaldin and H. Sankur, Diffusivity and solubility of Si in the Al metallization of integrated circuits, *Appl. Phys. Lett.* **19**, 524–527 (1971).

[113] C. Mader, R. Bock, J. Schmidt, and R. Brendel, Formation of highly aluminum-doped p-type silicon regions by in-line high-rate evaporation, *Sol. Energy Mater. Sol. Cells* **95**, 1720–1722 (2011).

[114] C. Mader, J. Müller, R. Bock, J. Schmidt, and R. Brendel, Formation of locally aluminum-doped p-type silicon regions by in-line high-rate evaporation, *Energy Procedia* **8**, 521–526 (2011).

[115] C. Sealy, M. Castell, and P. Wilshaw, Mechanism for secondary electron dopant contrast in the SEM, *J. Electron Microsc.* **49**, 311–321 (2000).

[116] R. Bock, J. Schmidt, and R. Brendel, n-type silicon solar cells with surface-passivated screen-printed aluminium-alloyed rear emitter, *Phys. Status Solidi RRL* **2**, 248–250 (2008).

[117] S. Bowden, D.S. Kim, C. Honsberg, and A. Rohatgi, Rapid thermal processing for front and rear contact passivation, *Proceedings of 29th IEEE Photovoltaic Specialists Conference, New Orleans, LA, USA*, pp. 410–413 (2002).

[118] C. Tool, P. Manshanden, A. Burgers, and A. Weeber, Higher efficiency for thin multi crystalline silicon solar cells by improving the rear surface passivation, *Proceedings of the 29th IEEE Photovoltaic Specialists Conference, New Orleans, LA, USA*, pp. 304–307 (2002).

[119] R. Bock, J. Schmidt, and R. Brendel, Effective passivation of highly aluminum-doped p-type silicon surfaces using amorphous silicon, *Appl. Phys. Lett.* **91**, 112112 (2007).

[120] M. Rauer, C. Schmiga, M. Hermle, and S. Glunz, Passivation of screen-printed aluminum-alloyed emitters for back junction n-type silicon solar cells, *Proceedings of the 24th European Photovoltaic Solar Energy Conference, Hamburg, Germany*, pp. 1059–1062 (2009).

[121] J. Müller, K. Bothe, S. Gatz, H. Plagwitz, G. Schubert, and R. Brendel, Recombination at local aluminum-alloyed silicon solar cell base contacts by dynamic infrared lifetime mapping, *Energy Procedia* **8**, 337–342 (2011).

[122] E. Urrejola, K. Peter, H. Plagwitz, and G. Schubert, Al-Si alloy formation in narrow p-type Si contact areas for rear passivated solar cells, *J. Appl. Phys.* **107**, 124516 (2010).

[123] J. Müller, K. Bothe, S. Gatz, H. Plagwitz, G. Schubert, and R. Brendel, Contact formation and recombination at screen-printed local aluminum-alloyed silicon solar cell base contacts, *IEEE Trans. Electron Devices* **58**, 3239–3245 (2011).

[124] P. Basore, Numerical modeling of textured silicon solar cells using PC-1D, *IEEE Trans. Electron Devices* **37**, 337–343 (1990).

[125] K. McIntosh and P. Altermatt, A freeware 1D emitter model for silicon solar cells, *Proceedings of the 35th IEEE Photovoltaic Specialists Conference, Honolulu, HI, USA*, pp. 2188–2193 (2010).

[126] H. Fischer and W. Pschunder, Investigation of photon and thermal induced changes in solar cells, *Proceedings of the 10th IEEE Photovoltaic Specialists Conference, Las Vegas, NV, USA*, pp. 404–411 (1973).

[127] K. Bothe, R. Sinton, and J. Schmidt, Fundamental boron-oxygen-related carrier lifetime limit in mono- and multicrystalline silicon, *Prog. Photovolt: Res. Appl.* **13**, 287–296 (2005).

[128] A. Herguth, G. Schubert, M. Kaes, and G. Hahn, Avoiding boron-oxygen related degradation in highly boron-doped Cz silicon, *Proceedings of the 21st European Photovoltaic Solar Energy Conference, Dresden, Germany*, pp. 530–537 (2006).

[129] B. Lim, K. Bothe, and J. Schmidt, Deactivation of the boron-oxygen recombination center in silicon by illumination at elevated temperature, *Phys. Status Solidi RRL* **2**, 93–95 (2008).

[130] K. Bothe, *Oxygen-related trapping and recombination centers in boron-doped crystalline silicon*, PhD thesis, University of Hannover (2006).

[131] B. Lim, *Boron-oxygen-related recombination centers in crystalline silicon and the effects of dopant-compensation*, PhD thesis, University of Hannover (2011).

[132] Deepak and H. Krishna, Measurement of small specific contact resistance of metals with resistive semiconductors, *J. Electron. Mater.* **36**, 598–605 (2007).

[133] R. Brooks and H. Mattes, Spreading resistance between constant potential surfaces, *Bell Syst. Tech. J.* **50**, 775–784 (1971).

[134] K. Catchpole and A. Blakers, Modelling the PERC structure for industrial quality silicon, *Sol. Energy Mater. Sol. Cells* **73**, 189–202 (2002).

[135] S. Glunz, E. Schneiderlöchner, D. Kray, A. Grohe, M. Hermle, H. Kampwerth, R. Preu, and G. Willeke, Laser-fired contact silicon solar cells on p- and n-substrates, *Proceedings of the 19th European Photovoltaic Solar Energy Conference, Paris, France*, pp. 408–411 (2004).

[136] S. Yang and J. Plá, Optimization of the back contact in c-Si solar cells, *Solid State Electron.* **53**, 925–930 (2009).

[137] J. Zhao, A. Wang, and M. Green, 24% efficient PERL structure silicon solar cells, *Proceedings of the 21st IEEE Photovoltaic Specialists Conference, Kissimmee, FL, USA*, pp. 333–335 (1990).

[138] J. Zhao, A. Wang, and M. Green, Series resistance caused by the localized rear contact in high efficiency silicon solar cells, *Sol. Energy Mater. Sol. Cells* **32**, 89–94 (1994).

[139] R. Brendel, S. Dreissigacker, N. Harder, and P. Altermatt, Theory of analyzing free energy losses in solar cells, *Appl. Phys. Lett.* **109**, 173503 (2008).

[140] F. Haase, S. Eidelloth, R. Horbelt, K. Bothe, E. Garralaga Rojas, and R. Brendel, Loss analysis of back-contact back-junction thin-film monocrystalline silicon solar cells, *J. Appl. Phys.* **110**, 124510 (2011).

List of Publications

PUBLICATIONS ARISING FROM THE WORK IN THIS THESIS:

Refereed journal papers

1. C. MADER, R. BOCK, J. SCHMIDT, AND R. BRENDEL, Formation of highly aluminum-doped p-type silicon regions by in-line high-rate evaporation, *Sol. Energy Mater. Sol. Cells* **95**, 1720-1722 (2011).

2. C. MADER, M. KESSLER, U. EITNER, AND R. BRENDEL, Temperature of silicon wafers during in-line high-rate evaporation of aluminum, *Sol. Energy Mater. Sol. Cells* **95**, 3047-3053 (2011).

3. C. MADER, R. BOCK, J. MÜLLER, J. SCHMIDT, AND R. BRENDEL, Formation of locally aluminum-doped p-type silicon regions by in-line high-rate evaporation, *Energy Procedia* **8**, 521-526 (2011).

4. C. MADER, J. MÜLLER, S. EIDELLOTH, AND R. BRENDEL, Local rear contacts to silicon solar cells by in-line high-rate evaporation of aluminum, *Sol. Energy Mater. Sol. Cells*, accepted for publication.

5. C. MADER, U. EITNER, S. KAJARI-SCHRÖDER, AND R. BRENDEL, Bow of silicon wafers after in-line high-rate evaporation of aluminum, *IEEE J. Photovoltaics*, submitted.

6. J. MÜLLER, K. BOTHE, S. GATZ, F. HAASE, C. MADER, AND R. BRENDEL, Recombination at laser-processed local base contacts by dynamic infrared lifetime mapping, *J. Appl. Phys.* **108**, 124513 (2010).

Papers presented at international conferences

1. C. Mader, J. Müller, S. Gatz, T. Dullweber, and R. Brendel, Rear side point-contacts by in-line thermal evaporation of aluminum, *Proceedings of the 35th IEEE Photovoltaic Specialists Conference, Honolulu, HI, USA*, pp. 1446-1449, (2010).

2. F. Heinemeyer, C. Mader, D. Münster, T. Dullweber, N. Harder, and R. Brendel, Inline high-rate thermal evaporation of aluminum as a novel industrial solar cell metallization scheme, *Proceedings of the 2nd Workshop on Metallization, Konstanz, Germany*, pp. 48-51, (2010).

3. F. Heinemeyer, C. Mader, D. Münster, T. Dullweber, and R. Brendel, Inline high-rate thermal evaporation of aluminum for novel industrial solar cell metallization, *Proceedings of the 5th World Conference on Photovoltaic Energy Conversion, Valencia, Spain*, pp. 2066-2068, (2010).

4. M. Kessler, D. Münster, T. Neubert, C. Mader, J. Schmidt, and R. Brendel, High-efficiency back-junction silicon solar cell with an in-line evaporated aluminum front grid, *Proceedings of the 37th IEEE Photovoltaic Specialists Conference, Seattle, WA, USA*, pp. 1085-1090, (2011).

5. J. Heinss, C. Mader, A. Merkle, T. Brendemühl, R. Brendel, L. Ehlers, and R. Meyer, Inline high rate deposition of aluminum onto RISE solar cells by electron beam technology, *Proceedings of the 26th European Photovoltaic Solar Energy Conference, Hamburg, Germany*, pp. 2121-2124, (2011).

6. R. Ferre, R. Gogolin, J. Müller, N. Harder, M. Kessler, C. Mader, P. Giesel, T. Neubert, R. Brendel, Laser transfer doping using amorphous silicon, *Proceedings of the 26th European Photovoltaic Solar Energy Conference, Hamburg, Germany*, pp. 879-883, (2011).

Presentations

1. C. Mader, Temperaturentwicklung beim Hochraten Durchlaufaufdampfen, *Workshop Hochratenverdampfen für die Photovoltaik, Emmerthal, Germany*, (2009).
2. C. Mader, In-line Hochraten Durchlaufaufdampfen, *Silicon-FOREST Workshop 2010, Falkau, Germany*, (2010).
3. C. Mader, F. Heinemeyer, T. Dullweber, and R. Brendel, Metallization of silicon solar cells by in-line high-rate evaporation of aluminum, *3rd Workshop on Metallization, Charleroi, Belgium*, (2011).

Patent Applications

1. C. Mader, R. Bock, Verfahren zum Metallisieren eines Halbleitersubstrates, Verfahren zum Herstellen einer Solarzelle sowie Metallisierungsvorrichtung, *DE 10 2009 024 472.9*, 2009.

Danksagung

Hiermit möchte ich mich bei all denjenigen bedanken, die zum Gelingen dieser Dissertation beigetragen haben und die mich sowohl bei der Arbeit als auch privat unterstützt haben.

Als erstes ist mein Betreuer am Institut für Solarenergieforschung (ISFH), Professor Dr.-Ing. Rolf Brendel, zu nennen, bei dem ich mich für die sehr gute wissenschaftliche Betreuung sowie die Anleitung zum wissenschaftlichen Arbeiten und die Hilfe beim Erstellen von Veröffentlichungen bedanken möchte.

Bei Professor Dr.-Ing. Lutz Rissing möchte ich mich für die Übernahme des Korreferates sowie bei Professor Dr. Holger Frahm für die Übernahme des Prüfungsvorsitzes meiner Disputation bedanken.

Des weiteren möchte ich mich bei den (z. T. ehemaligen) Gruppenleitern des ISFH, Professor Dr. Jan Schmidt, Dr. Karsten Bothe, Dr. Rüdiger Meyer, Dr. Thorsten Dullweber und Professor Dr. Nils-Peter Harder für die kompetente, oftmals spontane Unterstützung auf 'kurzem Dienstwege' bedanken.

Ein besonderer Dank gilt auch Dr. Bianca Lim, Dr. Robert Bock, Michael Kessler und Jens Müller für viele hilf- und lehrreiche Diskussionen und die Unterstützung beim Verfassen meiner Veröffentlichungen.

Natürlich möchte ich mich auch bei allen weiteren Kolleginnen und Kollegen vom ISFH bedanken: Vielen Dank an die Mitarbeiter der ATON-Projekte, an die Post-Docs, an alle Mit-Doktoranden, an die CTAs, an das Werkstatt-Team, an die Haustechnik, an die IT, an die Verwaltung,... Vielen Dank für das sehr angenehme, freundliche und persönliche Arbeitsklima!

Zu guter Letzt möchte ich mich ganz herzlich bei meinen Eltern, bei meinen Geschwistern Elisabeth, Johannes und Jacob und bei meiner Großmutter für die liebevolle Unterstützung bedanken! Y por supuesto le quiero dar las gracias a mi querida esposa Yuridia, que siempre me apoya con su amor.

Persönliche Daten

Name	Christoph Paul Mader
Anschrift	Großehofstr. 42, 31785 Hameln
Geburtsdatum	03. November 1980
Nationalität	Dänisch, deutsch
Familienstand	Verheiratet

Schulbildung

1987 - 1991	Grundschule Wulfsdorf, Lübeck
1991 - 2000	Katharineum zu Lübeck (Gymnasium) Abschluss der allgemeinen Hochschulreife im Juni 2000

Zivildienst

September 2000 - Juli 2001	Matthias-Leithoff-Schule, Lübeck

Universitätsausbildung

Oktober 2001 - März 2007	Universität Ulm Studium der Wirtschaftsphysik Diplomprüfung im Februar 2007
Oktober 2003 - September 2004	Université Joseph Fourier, Grenoble, Frankreich Studium der Physik
Oktober 2005 - Dezember 2006	Instituto de Investigaciones Electricas, Cuernavaca, Mexiko Praktikum und Diplomarbeit

Anstellung

März 2007 - April 2012	Institut für Solarenergieforschung (ISFH) Hameln/Emmerthal: Wissenschaftlicher Mitarbeiter im Bereich Produktionsprozesse